Radiofrequency Pulses For Improved Simultaneous Multislice Magnetic Resonance

Imaging

By

Anuj Sharma

Dissertation

Submitted to the Faculty of the

Graduate School of Vanderbilt University

in partial fulfillment of the requirements

for the degree of

DOCTOR OF PHILOSOPHY

in

Biomedical Engineering

August, 2015

Nashville, Tennessee

Approved:

William A. Grissom, Ph.D.

Adam W. Anderson, Ph.D.

Mark D. Does, Ph.D.

Manus J. Donahue, Ph.D.

Edward B. Welch, Ph.D.

ACKNOWLEDGEMENTS

First, I want to thank Dr. Will Grissom for accepting me as his first student four years ago. Working with him has been a wonderful experience, and I have grown both as a researcher and a person under his guidance. Among his many qualities, I admire Dr. Grissom's dedication to his field, his friendly approach, his commitment to his students and his ability to smile and stay composed in otherwise stressful times. I cannot thank this man enough. I was fortunate to have him as my advisor.

I am grateful to all the members of my dissertation committee. I am thankful to Dr. Adam Anderson for being supportive and providing ideas and feedback on my research work. The first MRI course I took was taught by Dr. Mark Does. I learned a lot in that class and I am thankful to him for his insightful thoughts and ideas for my research. Dr. Brian Welch is another professor whose classes I took. I admire his broad knowledge in the field of MRI and I am thankful to him for helping me maintain high scientific rigor in my projects. I am indebted to Dr. Manus Donahue for equipping me with the skills of functional MRI. I have enjoyed working with him and I am grateful to him for generously providing me his time to brainstorm my research projects.

I was blessed to be part of a lab with very nice people. I would like to thank Pooja, Julianna, Megan, Zhipeng, Chris, and Martin. Thanks for being my scan subjects (sometimes multiple times in a week), and for all the fruitful discussions and humor we shared. I wish to thank my other office mates, David, Kurt, John, and Nate for everything you did that made my years in graduate school enjoyable. You guys are all awesome and I wish you good luck in your careers.

My wife, Priyanka has been my pillar of strength for a long time. It was her support and encouragement that helped me come to a foreign country to pursue higher education. I am thankful to her for all the sacrifices she has made for me. Her most beautiful gift to me is our son Agastya. Thanks to him, my last year in graduate school was full of giggles. I love you both.

Finally, I wish to thank my dad Niranjan and mother Geeta for doing more for me than you ever could. I love you.

TABLE OF CONTENTS

LIST OF FIGURES

CHAPTER I

Introduction

Magnetic Resonance Imaging (MRI) is a diagnostic medical imaging technique based on the principle of nuclear magnetic resonance first observed by I. I. Rabi in 1937. The excellent soft tissue contrast, use of non-ionizing radiation and the range of possible contrast mechanisms have made MRI popular in medical imaging, especially for neuroimaging.

An MRI scanner uses a large main magnetic field to polarize the protons inside the human body. Under the effect of an external magnetic field, the protons undergo a precessing motion at a frequency which is dependent on the proton species and the strength of the magnetic field. The precession frequency is called the Larmor frequency, named after the Irish physicist Joseph Larmor. Along with precessing, the protons either align parallel or antiparallel to the main field. The parallel alignment is the more stable, low-energy state and that is how a higher number of protons orient. After the subject is placed in the main magnet, a radiofrequency (RF) pulse oscillating at the Larmor frequency is applied that transfers energy in the form of photons to tip some of the protons from the low-energy (stable) to the high-energy (unstable) state. When the RF pulse is turned off the high-energy protons that were earlier tipped go back to the low-energy state to maintain equilibrium. This change in state releases energy in the form of photons which are picked by RF receive coils. The current thus induced in the RF coils is the MR signal. Spatial localization is achieved by applying gradient magnetic fields in the three spatially orthogonal directions. Due to the gradient field, the precession frequency of the protons become a function of space. A desired imaging slice is excited by applying an RF pulse oscillating at the slice's precession frequency. The slice-thickness is governed by the bandwidth of the RF pulse. The gradients in the other two directions are used to apply frequency and phase encoding in the in-plane dimensions.

The diagnostic quality of an MR image can be improved by increasing it's signal-to-noise ratio (SNR). Signal can be boosted by having more protons in the parallel state which will later be tipped by the RF pulse. As the proportion of protons in the parallel state is inversely proportional to temperature, the MR signal can be increased by decreasing the temperature. Though theoretically possible, the temperature will have to be reduced by a large amount before a significant difference in the signal is observed. A feasible method to increase the signal is to increase the strength of the main magnet (B_0). Presently, scanners with main field strengths of up to 3 Tesla (T) are clinically used for human imaging, whereas magnets of up to 10.5 T have been developed for whole-body MR research.

With increasing field strength new technical challenges have emerged that affect image quality and patient safety. For example, RF wavelength shortening at high field makes transmit RF fields (B_1^+) nonuniform which leads to inhomogeneous image contrast. It is also more difficult to produce high strength magnets with a homogeneous field. The field inhomogeneity leads to image artifacts such as geometric distortion. The magnetic susceptibility artifacts near air-tissue interfaces are amplified at high field and cause signal voids in brain areas near the sinuses and middle ear. The specific absorption rate (an indirect measure of tissue heating that is limited to ensure patient safety) is also increased at high field which limits the performance of the RF pulses that can be played within regulatory limits. Consequently, there are a number of problems to solve before high field scanners will emerge into widespread clinical and research use.

The aim of this research work is to develop RF pulses and pulse sequences that mitigate some of the engineering challenges in high field imaging. Especially, the focus is on development of methods for simultaneous multislice (SMS) imaging also known as multiband imaging, which is a scan acceleration technique where multiple slices are simultaneously excited and received and are separated in reconstruction using the receive coils' field sensitivity maps.

This chapter introduces the fundamentals of MRI and SMS imaging, covering the basis

of small-tip and Shinnar-Le-Roux RF pulse designs. The current methods for mitigation of B_1^+ field inhomogeneity, through-plane signal loss and reduction of peak RF power are also discussed. Chapter II presents our proposed method for designing multiband pulses that compensate for B_1^+ field inmogeneity in SMS imaging. Chapter III introduces novel pulse sequences to reduce through-plane signal loss artifacts in long echo time gradient echo imaging. In Chapter IV we discuss a pulse design method to reduce the peak power of multiband refocusing pulses. We conclude with Chapter V by discussing our contributions and future work that can extend the presented research.

I.1 Nuclear Magnetic Resonance

Atomic nuclei with an odd number of protons exhibit the property of nuclear magnetic resonance (NMR). Such nuclei have both a magnetic moment and an angular momentum. Nuclei that exhibit the NMR property are generally referred to as spins and since water is the most abundant molecule in biological tissues, Hydrogen (^{1}H) proton is the most widely imaged species in MRI. We will use the term 'spins' and 'protons' interchangeably for hydrogen nucleus. When a proton is placed in an external magentic field it undergoes a gyromagnetic motion called precession. The precession frequency denoted by γ which is different for each type of nuclei is called the Larmor frequency. For protons, the Larmor frequency approximately equals 42.58 MHz/T. In a frame that rotates at the Larmor frequency, the behavior of a spin system with magnetic moment $M = (M_x, M_y, M_z)^T$ under the influence of an RF magentic field $b(t) = (b_x, b_y)^T$ and gradient field $G = (G_x, G_y, G_z)^T$ is governed by the Bloch equation which is given by:

$$\frac{\mathrm{d}M}{\mathrm{d}t} = \gamma \begin{pmatrix} -\dfrac{1}{\gamma T_2} & Gx & -b_y \\[2ex] -Gx & -\dfrac{1}{\gamma T_2} & b_x \\[2ex] b_y & -b_x & -\dfrac{1}{\gamma T_1} \end{pmatrix} \begin{pmatrix} M_x \\[1ex] M_y \\[1ex] M_z \end{pmatrix} + \begin{pmatrix} 0 \\[1ex] 0 \\[1ex] \dfrac{M_0}{T_1} \end{pmatrix} \tag{I.1}$$

where, T_1 is the time constant for the recovery of longitudinal magnetization and T_2 is the time constant for decay of transverse magnetization. In a non ideal system, where spins in a given chemical environment precess with different frequencies, T_2 is replaced with T_2^*. In general, the Bloch equation shows that the net magnetization of a spin system precesses around the net magnetic field at the Larmor frequency.

I.2 Functional Magnetic Resonance Imaging

In this section we introduce the blood oxygenation level dependent (BOLD) functional MRI (fMRI) method which is the target application for the through-plane signal loss compensation method discussed in Chapter III.

I.2.1 Physiological Basis of BOLD Contrast

The magnetic properties of hemoglobin molecule found in human blood varies based on whether it is bound to oxygen or not. Oxygenated hemoglobin (Hb) is diamagnetic with zero magnetic moment, whereas, deoxygenated hemoglobin (dHb) is paramagnetic. Being paramagnetic, dHb distorts the neighboring magnetic field which causes a faster decay of transverse magnetization. Therefore, T_2^*-weighted MR pulse sequences produce higher signals in the presence of Hb and lower signal in the presence of dHb. BOLD fMRI utilizes this phenomenon to make functional maps of the brain.

The nerve cell or the neuron is the functional unit of the brain. Neurons process and transmit information between the different regions of the brain in the form of electrical and chemical signals. The main parts of a neuron are the cell body or the soma which contains all the cell organelles, the axon that transmits information to other neurons and the protoplasmic processes called dendrites that integrate signal coming in from other neurons. The point of contact between the axon terminals of one neuron and the dendrites of another neuron is called a synapse. A neuron can have thousands of synaptic connections to other neurons. Information is transmitted at the synapse by way of neurotransmitters which are compounds released by the axon of the upstream neuron, neurotransmitters cause the

opening of specific ion channels in the downstream neuron. When ion channels in multiple synapses are simultaneously opened, an action potential may be generated which travels down the axon and in turn opens the ion channels in the neurons further downstream. The opening and closing of active ion channels requires energy which is provided in the form of a compound called adenosine triphosphate (ATP). In humans, one of the major sources of ATP is the breakdown of glucose. Generally, glucose is stored in the form of glycogen throughout the body but in higher concentrations in liver and muscles. The brain does not have a mechanism to store glucose. Therefore, the glucose in the brain needs to be replenished with the supply of freshly oxygenated blood. As the Hb in the oxygenated blood replaces dHb, T_2^* is elongated which leads to higher MR signal in T_2^*-weighted imaging sequences. This relationship between brain activity and its energy demands forms the basis of BOLD fMRI.

I.2.2 Experiment Setup and Pulse Sequence

As we established in the last section, changes in the brain's activity leads to changes in the MR signal. The change in MR signal due to neuronal activity is called hemodynamic response. In task-based fMRI experiments, MR signal is compared between periods of activity and periods of rest. The task performed by the subject during periods of activity is chosen to elicit response from the brain region that the researcher intends to study. In general, task based fMRI experiments can have block-based or event-based designs depending on the way the task or stimulus is presented. We focus the discussion on block design experiments which we use to validate pulse sequences proposed in Chapter III to mitigate through-plane signal loss in regions of susceptibility difference. In block design experiments the task is performed at a constant level for an elongated period of time, followed by periods of rest. The periods of task and rest together form a block which is repeated several times during the experiment. During the entire experiment, MR images are continuosly acquired to sample the hemodynamic response function. For example, a 64×64

image acquired every 2 s for 10 minutes generates 300 data points per voxel. The main factors to consider in a block design are the experiment conditions and the timing of the blocks. The experiment condition is directly related to the question that the study aims to answer. For example, if the researcher wants to study the visual cortex then an alternating design could be used where periods of visual stimulus presentation are altered with periods of no stimulation. In our functional studies in Chapter III, we use a breathhold block design experiment, where periods of breathhold are altered with periods of normal breathing. If a simple alternating design is insufficient then additional blocks may be added at the expense of longer scan durations. The timing of the blocks is mainly driven by the effect of the block length on the experimental task. If the task is too strenuous then the subject may get fatigued and may not be able to perform consistently through the entire block. In our breathhold experiments, the breathhold period was chosen to be 15 s which formed a good compromise between subject comfort and experiment efficiency. Typically, task blocks ranging from 10 s to 1 minute durations have been reported in earlier research studies.
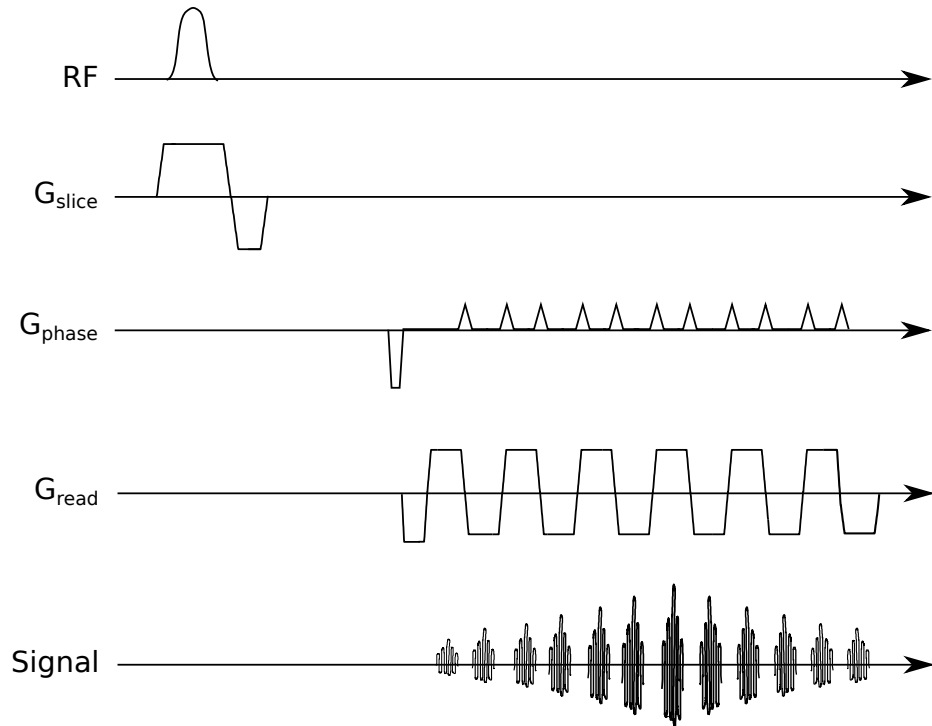
Figure I.1: Illustration of the gradient echo EPI sequence typically used in fMRI scans. After a single RF excitation, the entire k-space signal is acquired using an EPI readout. The peak of the signal occurs when the center of k-space is measured. Here a bipolar trajectory is shown where the signal is acquired on both the positive and negative lobes of the readout gradient. In a flyback trajectory, signal is acquired during either the positive or negative lobe.

The two major requirements for a fMRI pulse sequence are sensitivity to T_2^* and high temporal resolution. T_2-weighted sequences have also been earlier proposed but we limit the discussion to T_2^*-weighted sequences. As shown in Fig. I.1 the gradient recalled echo (GRE) sequence with a long echo time and an echo planar imaging (EPI) signal readout has become the workhorse of most BOLD fMRI experiments. In the GRE sequence, after the excitation pulse is played an echo is generated by a gradient reversal on the frequency encode axis. A prephasing gradient dephases the spins which are rephased by the readout gradient lobe. The peak of the echo signal is formed at the time point where the area of the prephasing and the readout gradients cancel. The time from the peak of the RF pulse to the peak of the echo signal is called the echo time (TE). During the echo time, the transverse

magnetization created by the excitation pulse decays at a rate defined by the T_2^* of the spin isochromat. At long TEs, transverse magnetization from spins with shorter T_2^* decay more than spins with longer T_2^*. Therefore, the use of long TE produces a T_2^*-weighted image. To meet the high temporal resolution requirement of fMRI scans, a single-shot EPI readout is used which fills the entire 2D Fourier space necessary to reconstruct an image. The scan time reduction achieved with EPI comes at the cost of artifacts such as ghosting and chemical shifts. These artifacts can be reduced by the use of scan acceleration methods such as parallel imaging and partial k-space acquisitions. These scan time reduction methods are discussed in section I.3.

I.2.3   Data Processing and Analysis

The two major steps in analysing fMRI data are preprocessing, and statistical analysis. As described in the previous section, the output of an fMRI experiment are images of the brain acquired at different time points. The goal of the preprocessing step is to remove undesirable variability in this data and prepare it for statistical analysis. One of the major sources of error in fMRI data is head motion. If the subject moves his/her head between the image acquisitions, then time series data from one voxel can contain information from multiple voxels. This spurious data can lead to detection of false activations. In general, head motion is either prevented by the use of head restraint systems or more commonly, head motion is retrospectively corrected by co-registering the images at different time points to one reference image in the time series. Physiological motion and scanner drift are two other sources of unwanted data variability. While designing a task-based experiment, it is important to choose the task frequency which is different from the frequency of physiological events such as breathing and beating of the heart. Then the unwanted variability in the time-series data can be removed by the use of temporal filters. Another common preprocessing step is the application of spatial smoothing filters on the images. Typically, a Gaussian filter of 3-5 mm full-width-at-half-max (FWHM) is convolved with the images to reduce the

high-frequency spatial components.
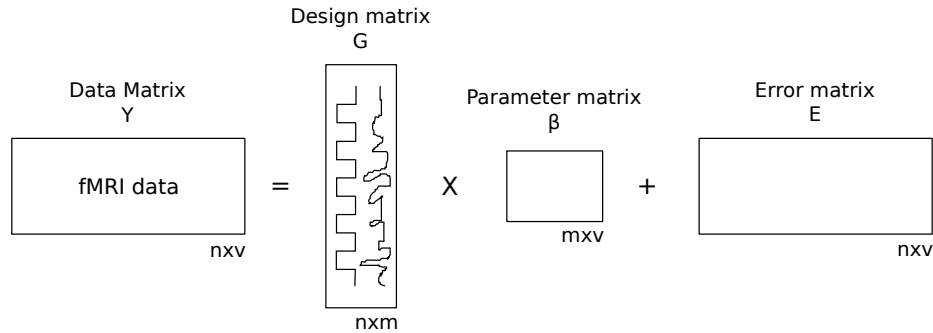
Figure I.2: Illustration of the General Linear Model setup. The fMRI data matrix Y is modeled as a linear combination of regressors represented by the design matrix G, with the weights defined by the parameter matrix β, summed with an error matrix E

Once the data is preprocessed, statistical tests are run to form the fMRI activation maps. From a simplistic view, the goal of statistical analysis is to run tests on time-series data from each voxel and infer which voxels correlate with the stimulus. The voxels that pass the test are marked as 'active'. There are many different approaches to statistical analysis of fMRI data. We will discuss the more common General Linear Model (GLM) approach [2] which we use to analyze our fMRI dataset in Chapter III. Figure I.2 shows the GLM setup. The fMRI data obtained from specific spatial locations at different time points are organized into a 2D data matrix Y with n rows (time points) and v columns (voxels). The data is assumed to be produced by a linear combination of regressors which model the experimental condition. The regressors are organized in a design matrix G with n rows and m columns, one for each regressor. From the block design, a regressor is built with two discrete levels, one for each of the two experiment conditions. To accurately model the physiological response, the regressor is convolved with the canonical hemodynamic response function. The weights of the regressors are represented by a parameter matrix β with m rows and v columns. And the error matrix E with n rows and v columns represents the residual error for each voxel. In the GLM, the data and design matrices are known, and the regressor weights and residual errors are calculated during the analysis. One of the benefits of using GLM is that it provides a framework in which many statistical tests such

9

as the student's *t* test and ANOVA (analysis of variance) can be casted. In an experiment where the regressor has two discrete levels, the *t* test can be performed to compare the two conditions. Voxels with a *t* statistic value below the chosen significance level α, are marked as active. An activation map is formed for the entire brain by thresholding all the voxels. Finally, the activation map is overlaid on an anatomical image to show which brain regions were activated by the performed task.

I.3 Methods to Reduce Scan Time

In recent years, new research initiatives have pushed MR imaging to its technical limits and have thus opened new avenues. One such program, The Human Connectome Project, aims to form a detailed map of the structural and functional neural networks in the human brain. Given that the human brain contains about 10 billion neurons and each neuron is connected to other neurons by about 10,000 synapses which communicate with each other at roughly 100 Hz, mapping all the networks is a daunting task. Any imaging method employed to map the detailed structure and function of the brain needs to have a high spatial and temporal resolution. In the Connectome project, the main technique employed to map the human brain is diffusion imaging. But diffusion imaging based methods suffer from long scan durations. To accelerate diffusion-weighted scans, simultaneous multislice imaging [3] has been previously employed [4]. However, the multiband RF pulses used in simultaneous multislice imaging are limited by the available peak RF power and SAR limits. In this section, we give an overview of some of the existing methods to reduce scan time and in Chapter IV we introduce low peak power spin echo RF pulses that can be used to accelerate diffusion-weighted imaging.

Conventionally, in Fourier imaging the imaged object is repeatedly excited using an RF pulse and data is sequentially acquired to fill the Fourier(k)-space. Thus multiple RF shots are applied to acquire one image. The time interval between the application of two consecutive RF pulses is called the repetition time (TR) and the duration from the application of

the RF pulse to the acquisition of the MR siganl is called the echo time (TE). The total scan duration is given by TR×N, where N is the number of RF repetitions which is dependent on the desired image resolution and field-of-view (FOV). From Nyquist sampling theorem, for a given FOV the minimum k-space resolution $\triangle k$ required to form an image without any aliasing artifacts is given by:

$$\triangle k = \frac{1}{FOV} \tag{I.2}$$

and to achieve a desired image resolution $\triangle x$, the extent of k-space data required is given by:

$$K = \frac{1}{\triangle x} \tag{I.3}$$

Therefore, N can be calculated as:

$$N = \left\lceil \frac{K}{\triangle k} \right\rceil = \left\lceil \frac{FOV}{\triangle x} \right\rceil \tag{I.4}$$

For a typical 2D brain scan at 3 T the parameters are: $FOV = 26$cm, $\triangle x = 3$mm and $TR = 2$s, which give a minimum scan time of approximately 3 minutes to acquire one 2D brain slice. This sampling rate is inadequate for probing the workings of the neural networks.

The existing methods to increase the temporal resolution of MR images can be broadly classified into two categories: methods that fully sample k-space at a faster rate and methods that undersample k-space. We will next discuss both of these approaches.

I.3.0.1 Single-Shot Imaging

The core idea of the first set of approaches is to reduce the number of repetitions or RF shots (N) required to synthesize an image. In the extreme case of single-shot imaging $N = 1$, which will reduce the scan time in our earlier example from 3 minutes to 2 s. To sample the entire k-space in one shot, 2D trajectories are employed. Echo-planar imaging (EPI) and spiral are two of the most common trajectories used. Figure I.3 compares the

11

gradient waveforms and k-space trajectories of spiral and EPI acqusition methods.
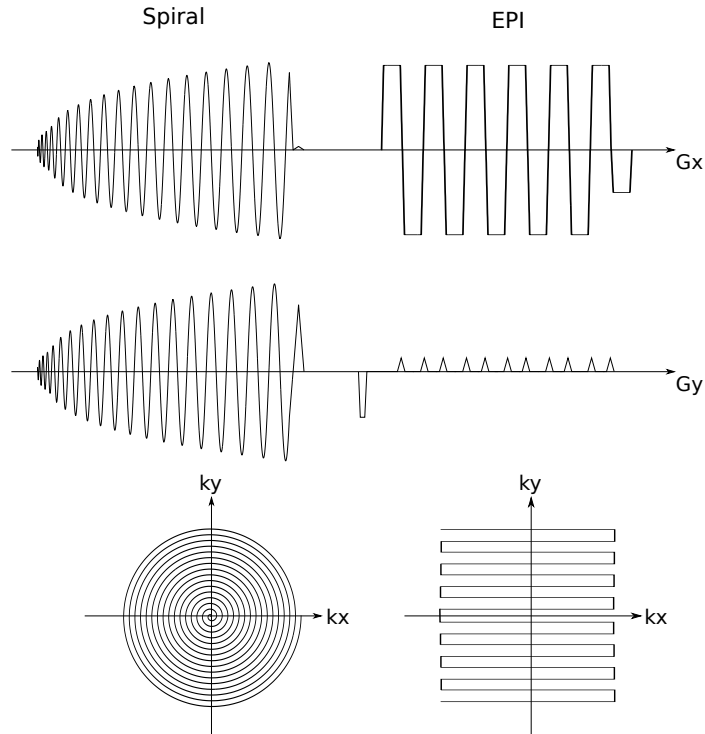
Figure I.3: Illustration of single-shot spiral and EPI gradient waveforms and k-space trajectories which fully sample the k-space in one TR.

Both of these methods are widely used in fast imaging schemes, especially EPI has become the workhorse of fMRI. However, the reduced scan time achieved with single-shot imaging comes at the cost of various image artifacts. For example, EPI suffers from T_2^*-induced image blurring, chemical shift artifacts in the phase-encode direction and geometric distortion and ghosting artifacts in the presence of inhomogeneous magnetic fields. Similarly, spiral acquisitions suffer from problems such as image blurring due to off-resonance effects and waveform distortion due to high gradient slew-rate demands. In practice, single-shot imaging requires pro- and retrospective corrections to mitigate the various image artifacts.

I.3.0.2 Scan Acceleration Methods

The second category of methods to increase the temporal resolution of MR images comprises approaches that acquire partial data at sub-Nyquist rate and aim to synthesize images without any aliasing artifacts. SMS imaging falls in this category. These methods either utilize the conjugate symmetry property of Fourier data or use receive coil sensitivities to fill-in for the missing gradient encoding.

One of the straightforward approaches is the partial Fourier method. MR data is acquired in one half of k-space and the other half is filled by exploiting the Hermitian conjugate symmetry of Fourier domain. Typically, additional lines of k-space are sampled to compute a low resolution correction phase map. Figure I.5 shows an illustration of the partial Fourier data sampling scheme.
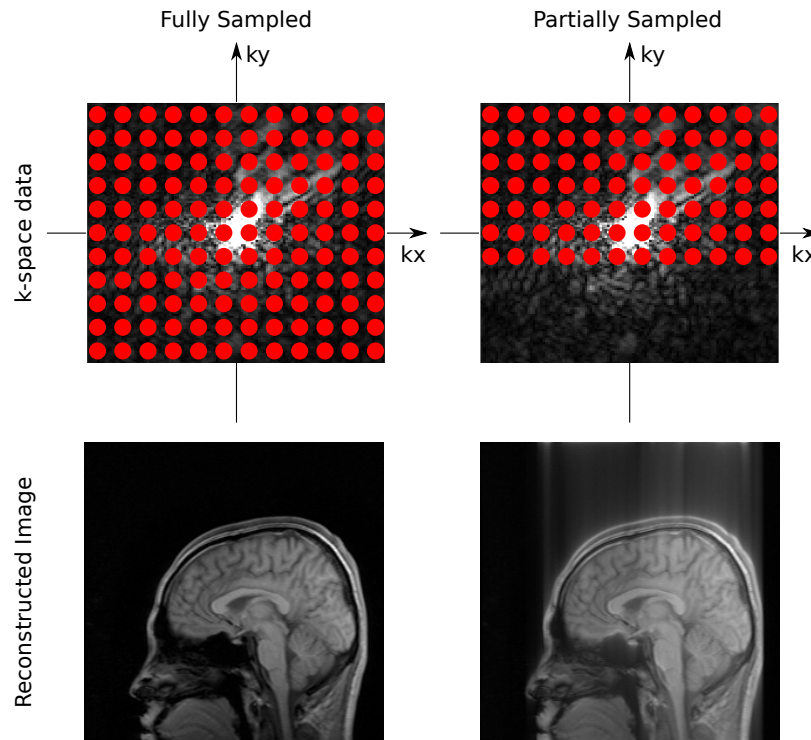
Figure I.4: Illustration of partial Fourier data acqusition. Red dots indicate the sampled k-space date. Images reconstructed using the complete and partial k-space data, respectively, are shown.

The scan acceleration achievable with partial Fourier methods is limited. Usually, 60-

75% of the data has to be acquired to faithfully reconstruct the image. Also, the conjugate symmetry property holds for Fourier transform of real images. Since MR images are complex the *k*-space symmetry is an approximation.

A scan acceleration technique that has gained wide popularity is parallel imaging. Multiple localized receive coils with intentionally non-uniform fields are employed to acquire undersampled MR data. Two of the popular methods to reconstruct images without un-aliasing artifacts are SENSE [5] and GRAPPA [6]. While SENSE unfolds the aliases in the image domain using the receive coil sensitivity maps, GRAPPA works in the Fourier domain to synthesize the missing data using a kernel calibrated from fully-sampled low resolution images. Both of these parallel imaging methods are now routinely employed in fMRI scans.
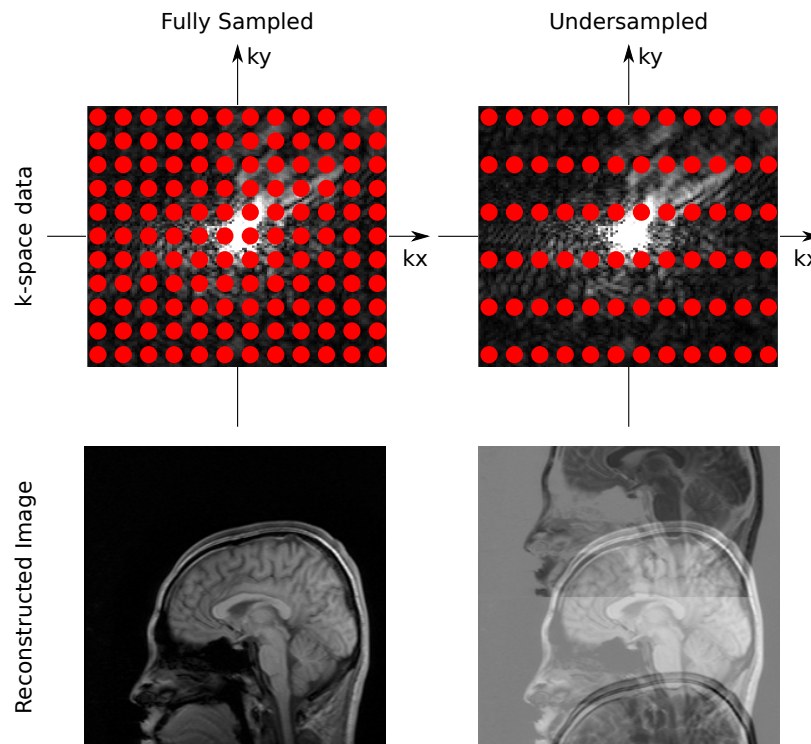
Figure I.5: An image reconstructed using undersampled data shows aliasing artifacts in the direction of undersampling. In parallel imaging, undersampled data is acquired and the spatial encoding provided by the multiple receive coils is used to unfold the images.

In the next section we discuss a scan acceleration method called simultaneous multislice

imaging which allows for acquiring multiple slice images in parallel.

I.3.0.2.1 Simultaneous Multislice Imaging

Analogous to parallel imaging, simultaneous multislice (SMS) imaging undersamples data in the slice direction and the slice images are unfolded using the receive coil's senstivity maps. Figure I.6 illustrates the SMS imaging method. In conventional single-slice imaging, slice-selection is performed by applying a linear gradient in the slice direction with an RF pulse modulated to the frequency of the spins at the desired location. For a given gradient amplitude, the thickness of the excited slice is defined by the bandwidth of the RF pulse. In conventional SMS imaging, a multiband pulse is generated by taking a complex-sum of the slice-selective pulses. In the presence of a gradient the multiband pulse simultaneously excites the desired slices and a 2D readout causes the slices to collapse (alias) on top of each other.
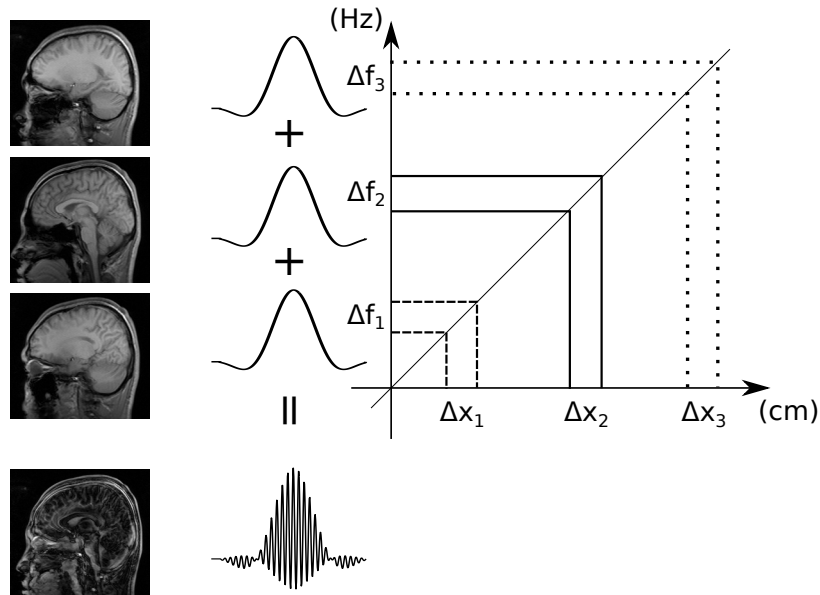
Figure I.6: Illustration of simultaneous multislice imaging method. A conventional multi-band pulse is generated by summing slice-select pulses designed to excite slices with desired thickness and location. Scan acceleration is achieved by using 2D data sampling which causes the slice images to collapse on top of each other.

Larkman et al. [3] first demonstrated SMS imaging and proposed to use the SENSE

(Sensitivity Encoding) [5] method from parallel imaging to reconstruct the slice images. The complex collapsed signal C_j acquired by coil j is given by:

$$C_j = S_{j1}x_1 + S_{j2}x_2 + \ldots + S_{jk}x_k \tag{I.5}$$

where S_{jk} is the complex sensitivity of coil j at spatial location x_k. For N_c coils, the complex signal from each slice can be estimated as $x = (S^*\Psi^{-1}S)^{-1}S^*\Psi^{-1}C$, where Ψ is $N_c \times N_c$ receiver noise matrix. For the matrix $(S^*\Psi^{-1}S)$ to be invertible, the number of aliased pixels should not exceed the number of coils. Therefore, the achievable acceleration factor is limited by the number of receive coils.

Where SENSE aims to unfold the aliased slices in the image domain, an alternate method to synthesize missing data in the Fourier domain is slice-GRAPPA [1] which is inspired by the parallel imaging reconstruction method called GRAPPA (Generalized Autocalibrating Partially Parallel Acquistions) [6]. But unlike conventional GRAPPA which synthesizes missing k-space data, slice-GRAPPA creates entirely new data for the separated slices. The idea is that the k-space data of each coil and slice can be created by a weighted-sum of collapsed data from all the coils. The synthesized k-space data $C_{j,z}$ for coil j and slice z is given by:

$$C_{j,z}(k_x,k_y) = \sum_{l=1}^{N_c} \sum_{b_x=-Bx/2}^{B_x/2} \sum_{b_y=-B_y/2}^{B_y/2} n_{j,z,l}^{b_x,b_y} C_{l,collapse}(k_x - b_x \triangle k_x, k_y - b_y \triangle k_y) \tag{I.6}$$

where, $n_{j,z,l}$ is the weight at location (b_x, b_y) of the GRAPPA kernel of size $B_x \times B_y$ for coil l applied to the collapsed data $S_{l,collapse}$. The weights are calculated by fitting a kernel on single-slice training dataset acquired in the pre-scan stage.

I.4 Radiofrequency Pulse Design

In this section we describe two RF pulse design methods that are used to construct the pulses proposed in Chapter II and IV to mitigate transmit field inhomogeneity and peak RF

power, respectively, in simultaneous multislice imaging.

I.4.1 Small-tip-angle Pulse Design

This section is based on Ref. [7, 8].

The small-tip approach proposed by Pauly et al. [7] provides a straightforward method for RF pulse design by utilizing a Fourier relationship between the RF pulse and the excited magnetization pattern. When the pulse excites a small flip angle, it can be assumed that the longitudinal magnetization M_z is equal to the equilibrium magnetization M_0. And for short duration pulses, T_1 and T_2 can be assumed to be infinity, and the bloch equation I.1 can be rewritten as

$$\frac{\mathrm{d}M}{\mathrm{d}t} = \gamma \begin{pmatrix} 0 & Gx & -b_y \\ -Gx & 0 & b_x \\ b_y & -b_x & 0 \end{pmatrix} \begin{pmatrix} M_x \\ M_y \\ M_z \end{pmatrix} \tag{I.7}$$

Using the small-tip approximation and multiplying out Eq. I.7 gives:

$$\frac{\mathrm{d}M_x}{\mathrm{d}t} = \gamma(M_y Gx - M_0 b_y)$$

$$\frac{\mathrm{d}M_y}{\mathrm{d}t} = \gamma(-M_x Gx + M_0 b_x) \tag{I.8}$$

By defining the transverse magnetization as $M_{xy} = M_x + \iota M_y$ and the applied RF pulse as $b = b_x + \iota b_y$, and combining the above two equations we get:

$$\frac{\mathrm{d}M_{xy}}{\mathrm{d}t} = \iota\gamma(-GxM_{xy} + M_0 b) \tag{I.9}$$

where $\iota = \sqrt{-1}$. The solution to this first-order differential equation at the end of the pulse duration T is given by:

$$M_{xy}(x) = \iota\gamma M_0 \int_0^T b(t)e^{-\iota\gamma x \int_t^T G(s)ds} dt \tag{I.10}$$

If we define a spatial frequency term $k(t) = -\gamma \int_t^T G(s) ds$ then M_{xy} can be rewritten as:

$$M_{xy}(x) = \iota \gamma M_0 \int_0^T b(t) e^{\iota x k(t)} dt \qquad (\text{I.11})$$

Equation I.11 shows that in the small-tip regime the magnetization pattern is the Fourier transform of the RF pulse evaluated on the excitation k-space trajectory $k(t)$. Thus given an excitation k-space trajectory, a RF pulse can be designed to excite a desired magnetization pattern [7, 9].

A recent significant development has been the use of multiple RF transmitters in parallel [10, 11] in applications such as patient-tailored field inhomogeneity mitigation and reduced field-of-view imaging. In parallel transmit, multiple coils are used each with a localized sensitivity to excite the spins in the imaged object. Therefore, the magnetization pattern is a superposition of the magnetization caused by the RF pulse played on each channel weighted by the coil's localized sensitivity. Therefore, for parallel transmit, M_{xy} can be rewritten as:

$$M_{xy}(x) = \iota \gamma M_0 \sum_{c=1}^{C} s_c(x) \int_0^T b_c(t) e^{\iota x k(t)} dt \qquad (\text{I.12})$$

where $s_c(x)$ and RF pulse b_c are the sensitivity pattern and RF pulse for each of the C transmit coils.

To design a RF pulse on a computer Eq. I.12 can be discretized and rewritten in the matrix-vector form as:

$$m = \sum_{c=1}^{C} S_c A b_c \qquad (\text{I.13})$$

where, m is a length N_s vector of magnetization pattern at all spatial locations, $S_c = diag\{s_c(x)\}$, b_c is a length N_t vector of RF pulse samples for channel c, and A is a size $N_s \times N_t$ system matrix whose element at location (i, j) is given by:

$$a_{ij} = \iota \gamma M_0 \triangle t e^{\iota x_i k(t_j)} \qquad (\text{I.14})$$

The summation in Eq. I.13 can be replaced with matrix multiplication by concatenating the system matrices and RF pulse vectors along the coil dimension such that:

$$m = [S_1A \ldots S_cA] \begin{bmatrix} b_1 \\ \vdots \\ b_c \end{bmatrix} = A_{full}b_{full} \qquad (I.15)$$

An RF pulse b_{full} that excites a magnetization pattern m can be designed by solving the following minimization problem.

$$\min_{b_{full}} ||A_{full}b_{full} - m||_W^2 + R(b_{full}) \qquad (I.16)$$

where, W is a $N_s \times N_s$ diagonal matrix containing the spatial weightings that can be used to mask locations outside the region of interest. For example, in brain imaging W will contain 1's for pixels inside the brain and 0's for those outside. $R(b_{full})$ is a regularization term that can be used to control certain properties of the RF pulse. For example, $R(b_{full})$ can be set to $\lambda b'_{full}b_{full}$ to control the integrated power of the designed RF pulse, where λ is a scalar factor that balances the regularization with the excitation error. Equation I.16 is a convex optimization problem which can be efficiently solved using iterative descent methods such as steepest descent or the conjugate gradient (CG) method.

In this section we have discussed the spatial domain method to design small-tip RF pulses [12] that produce a desired excitation pattern. In Chapter II we will extend this formalism to design multiband spokes pulses. The next section presents another pulse design method that can be used to design single-channel slice-selective RF pulses.

I.4.2   Shinnar Le-Roux Pulse Design Method

This section is based on Refs. [13, 14, 15].

Shinnar et al. and Le Roux [13, 14] independently proposed a method for RF pulse design based on approximations to the spin domain representation of the Bloch equation.

Later, Pauly et al. [15] derived analytic expressions relating RF pulse and slice profile characteristics that made the Shinnar and Le Roux's algorithm more useful. This method, popularly known as SLR, is the basis of our proposed low peak power multiband pulses discussed in Chapter IV. In this section we summarize the SLR algorithm.

In the spin domain, the Bloch equation is given by:

$$
\begin{pmatrix} d\beta/dt \\ d\alpha^*/dt \end{pmatrix} = \frac{\iota\gamma}{2} \begin{pmatrix} Gx & b^* \\ b & -Gx \end{pmatrix} \begin{pmatrix} \beta \\ \alpha^* \end{pmatrix}
\tag{I.17}
$$

where * represents the mathematical conjugate operation and α and β are called the Cayley-Klein parameters which are given by,

$$
\begin{aligned}
\alpha &= \cos\phi/2 - \iota n_z \sin\phi/2 \\
\beta &= -\iota(n_x + \iota n_y)\sin\phi/2
\end{aligned}
\tag{I.18}
$$

where ϕ is the rotation angle, and $\hat{n} = \{n_x, n_y, n_z\}$ represent the unit vector. α and β satisfy the condition $\alpha\alpha^* + \beta\beta^* = 1$ so that Q is a unitary (length-preserving) rotation matrix. The solution to the Bloch equation I.17 is a rotation and the effect of an RF pulse on a spin system can be modeled by a 2×2 unitary matrix of the form:

$$
Q = \begin{pmatrix} \alpha & -\beta^* \\ \beta & \alpha^* \end{pmatrix}
\tag{I.19}
$$

If the RF pulse is assumed to be piecewise constant then the net effect of the pulse on a spin system can be modeled by a series of rotations. The rotation parameters for the jth RF sample of duration $\triangle$t is given by

$$
\begin{aligned}
\phi_j &= -\gamma\triangle t \sqrt{|b_j|^2 + (Gx)^2} \\
n_j &= \frac{\gamma\triangle t}{|\phi_j|}(b_{x,j}, b_{y,j}, Gx)
\end{aligned}
\tag{I.20}
$$

and the Cayley-Klein parameters for the jth interval are

$$
\begin{aligned}
a_j &= \cos\phi_j/2 - \iota n_{z,j}\sin\phi_j/2 \\
b_j &= -\iota(n_{x,j} + n_{y,j})\sin\phi_j/2
\end{aligned}
\tag{I.21}
$$

The rotation matrix Q_j for the jth sample and the total rotation Q produced by the entire pulse are given by

$$
Q_j = \begin{pmatrix} a_j & -b_j^* \\ b_j & a_j^* \end{pmatrix}
\tag{I.22}
$$

$$
Q = Q_n Q_{n-1}\cdots Q_1
$$

From the spin domain notation an expression to compute the magnetization can be derived. Given the initial state of the transverse and longitudinal magnetization M_{xy}^- and M_z^-, magnetization M_{xy}^+ and M_z^+ at the end of the pulse can be calculated by solving:

$$
\begin{pmatrix} M_{xy}^+ \\ M_{xy}^{+*} \\ M_z^+ \end{pmatrix} =
\begin{pmatrix}
(\alpha^*)^2 & -\beta^2 & 2\alpha^*\beta \\
-(\beta^*)^2 & \alpha^2 & 2\alpha\beta^* \\
-\alpha^*\beta^* & -\alpha\beta & \alpha\alpha^* - \beta\beta^*
\end{pmatrix}
\begin{pmatrix} M_{xy}^- \\ M_{xy}^{-*} \\ M_z^- \end{pmatrix}
\tag{I.23}
$$

Table I.4.2 shows the analytic expressions for the slice profile of some of the common imaging pulses calculated using Eq. I.23.

Excitation	$M_{xy}^+ = 2\alpha^*\beta M_0$
Inversion	$M_z^+ = (\alpha\alpha^* - \beta\beta^*)M_0$
Spin echo	$M_{xy}^+ = (\alpha^*)^2 M_{xy}^- - \beta^2 M_{xy}^{-*}$
Crushed spin echo	$M_{xy}^+ = -\beta^2 M_{xy}^{-*}$

In Chapter IV we use these results to derive the ripple relationships for the proposed root-flipped refocusing pulses.

A second simplification made in the SLR algorithm is the hard-pulse approximation. Under this, if the RF and gradient rotations are small in a given time step, then their ro-

tation matrices can be split into two sequential rotations, free precession under the effect of the local gradient field and a rotation about the applied RF vector. Using the hard pulse approximation, Pauly et. al. showed that the Cayley-Klein parameters at the nth time step can be written as

$$A_n(z) = \sum_{j=0}^{n-1} a_j z^{-j}$$

(I.24)

$$B_n(z) = \sum_{j=0}^{n-1} b_j z^{-j}$$

where $z^{-j} = e^{-\iota \gamma G x \Delta t}$. With this representation the effect of an RF pulse is reduced from a product of n 2×2 rotations to a product of two $(n-1)$-order polynomials. The recursion that maps an RF pulse to two complex polynomials $A_n(z)$ and $B_n(z)$ is called the forward SLR transform. As a corollary, given two related polynomials $A_n(z)$ and $B_n(z)$, the inverse SLR transform calculates the RF pulse that produces these polynomials. Thus RF pulse design is reduced to a polynomial design problem.

In practice, polynomials $A_n(z)$ and $B_n(z)$ can be determined by first approximating $B_n(z)$ with a polynomial and then factoring it to find $A_n(z)$. Since $B_n(z)$ is directly proportional to the *sine* of half the flip angle, $B_n(z)$ polynomial is designed to match the desired slice profile. The magnitude of $A_n(z)$ can then be found as $|A_n(z)| = \sqrt{1 - B_n(z)B_n^*(z)}$. The phase of $A_n(z)$ can be determined from the fact that the log-magnitude of a minimum-phase $A_n(z)$ and its phase form a Hilbert transform pair. Once $A_n(z)$ and $B_n(z)$ are determined, the RF pulse can be computed by the inverse SLR transform. In Chapter IV we use the SLR formalism to design multiband root-flip pulses by first designing a multiband $B_n(z)$ polynomial and then flipping the roots of the polynomial to compute a pulse with minimum peak power.

I.5   Technical Challenges in High Field Simultaneous Multislice Imaging

Till now, this chapter has focused on the imaging methodologies and RF pulse design methods that are utilized in the presented research work. Now, we describe the engineering

problems in high field imaging, that the proposed research aims to mitigate.

I.5.1 Transmit Radiofrequency Field Inhomogeneity

The Larmor frequency of spins increases with the main field strength. Because RF pulses need to oscillate at the Larmor frequency for excitation, with increasing field strength the RF wavelength gets shorter. At high field strengths (≥ 3 T), the RF wavelength becomes comparable to the size of the human anatomical structures. This leads to field-focusing effects that produce spatially varying image contrast. For example, at 7 T the proton Larmor frequency is 300 MHz with a wavelength of approximately 11 cm in water [16, 17]. As this is smaller than the dimensions of an average human head, the phase distribution of the RF field from a given source varies considerably across the field of view. Therefore RF waves

Figure I.7: $|B_1^+|$ maps and images in 3 slices at 7 T. Non-uniform $|B_1^+|$ field leads to center-brightening artifact in the images.

from various sources such as coil elements and tissue boundaries with different dielectric constants destructively interfere to cause field cancellations. Figure I.7 shows the typical center-brightening image artifact caused by non-uniform $|B_1^+|$ field in three slices imaged at 7 T using a birdcage coil.

I.5.2 Through-plane Signal Loss Due to High Susceptibility Gradient

Another significant setback at high fields is the signal loss seen in long echo time gradient echo scans near the air-tissue interfaces due to magnetic susceptibility differences. The susceptibility difference between air and tissue creates a background gradient field that applies an approximate linear phase shift to the excited spins in the slice direction. At signal read-
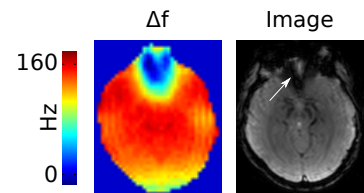
Figure I.8: Off-resonance (Δf) map and image acquired at 3 T in a human head using a GRE sequence with TE = 35 ms. Arrow points to signal loss region.

23

out the spins' signals cancel causing a signal null in the brain images in regions near the sinuses in the frontal lobe and near the middle ear in the temporal lobes. These effects limit the successful use of SMS imaging in high field, long echo-time gradient echo scans such as BOLD fMRI. Figure I.8 shows a representative off-resonance (Δf) map with in-plane field variation and the corresponding long echo-time (TE) gradient echo image with signal loss in the frontal lobe.

I.5.3 Peak Power Demand of Multiband RF Pulses

Since a conventional multiband RF pulse is constructed by taking a complex sum of the slice-selective pulses the peak RF amplitude increases linearly with the number of excited slices. Since RF power is proportional to the square of RF amplitude, the peak power increases quadratically with the number of slices. As the number of excited slices increases, the peak RF demand quickly reaches the maximum power limit of the RF amplifier. This limits the maximum scan acceleration that can be achieved with SMS imaging. Especially large-tip pulses such as refocusing pulses for spin echo acquisitions are limited by the peak power demand. In section IV we propose a new method to design low peak power multiband refocusing pulses based on the SLR algorithm.

In this section we described the technical challenges in high field imaging, in the next section we explore the existing methods that address these problems.

I.6 Current Methods for Transmit Field Inhomogeneity Compensation in Simultaneous Multislice Imaging

In the past there have been significant developments to prospectively mitigate the effects of field inhomogeneity in single-slice and conventional multi-slice imaging. But few methods have been developed to address the high field effects in SMS imaging. To correct the $|B_1^+|$ artifacts in the human head at 7 T, Yang et. al. [18] have proposed the use of dielectric water pads around the head to redistribute the RF field. Since water has a high permittivity it alters the displacement current distribution and thus the RF field distribution. Dielectric

pads have been shown to produce homogeneous excitation but it is difficult to tailor the current distribution to correct localized field inhomogeneity. The more successful and popular methods to mitigate $|B_1^+|$ effects are based on patient-tailored RF pulses in conjunction with parallel transmission. Saekho et. al. [19] have demonstrated the use of spokes pulses to mitigate artifacts in single-slice images. Among the few patient-tailored multiband pulse design approaches, Wu et. al. [20] have proposed a method for RF shimming of multiband pulses. Though their method reduces the $|B_1^+|$ artifacts, it doesn't fully utilize all the degrees of freedom that can be achieved with a multi-dimensional pulse such as the spokes pulse. The tailored multi-dimensional multiband pulses we propose can achieve higher levels of excitation uniformity, and are effective even with a single transmit channel.

I.7 Current Methods for Signal Loss Mitigation in Gradient Echo Imaging

As early as 1988, Young et. al. [21] independently proposed the straightforward approach of thin-slice averaging to recover signal near the air-tissue interfaces. In this method multiple thin slices are acquired and averaged to cover the desired imaging slice thickness. Though simple and effective in reducing the signal loss, it leads to increase in scan time and reduced SNR, both of which are detrimental to fMRI scans which require high temporal resolution and high SNR. New hardware approaches have also been proposed to effectively shim the regions of through-plane susceptibility gradient. Wilson et al. [22] demonstrated that placing materials with high diamagnetic susceptibility in the roof of the mouth can passively shim the regions of signal loss in the brain. This approach can only achieve localized shimming near the region where the passive shim is placed. Since the shim material is palced in a body cavity, this method is affected by safety concerns such as RF heating and eddy currents induced in the shim material. A general shortcoming of hardware-based methods is that they require more hardware to be placed near the subject, which conflicts with the need to place RF coils and stimulation equipment, and maintain subject comfort. Therefore, many researchers have looked into pulse sequence based methods which can be

broadly classified into two categories: z-shim and tailored RF pulses based methods. The method proposed by us in Chapter III falls under this category.

I.7.1   Z-shim Based Methods

Constable et al. [23] proposed the so called 'z-shim' gradient compensation method wherein a compensatory gradient waveform (z-shim) is played in the slice direction to cancel phase accrued due to off-resonance at TE. Multiple images are acquired with different z-shim strengths to refocus different regions and the images are combined to form one image with no signal loss. However, a significant drawback to the method is that the shimmed images must be acquired in separate TRs to maintain full signal, since the entire slice is excited for each shim measurement. This is not suitable for fMRI which demands a high temporal resolution.

Many variants of the z-shim based method have been proposed that combine z-shim with other pulse sequences to mitigate the scan time penalty of the conventional z-shim approach. Song [24] proposed to reduce the scan time by performing two partial k-space single-shot EPI readouts in one TR separated by a z-shim blip. The two EPI images are combined in reconstruction to form one image with nominally no signal loss. For more than two signal-loss bands the readout time of this method can become prohibitively long causing T_2^* mismatch between the bands and significant T_2^* decay in the bands that are acquired later. In another similar approach, Guo et al. [25] embedded a z-shim gradient between a spiral-in and a spiral-out readout in the same TR, thus creating two images with and without signal-loss correction respectively. They also showed that combining the images using a sum-of-squares operation produces the most uniform image compared to direct sum, weighted-sum and maximum intensity projection. This method has similar disadvantages as the dual-EPI approach. To address the problem of T_2^* mismatch between the different bands Heberlein et al. [26] proposed to acquire a z-shimmed gradient echo EPI image and a z-shimmed asymmetric spin echo EPI image in the same TR. They tuned

the sequence timing so that the two acquired bands have the same T_2^*-weighting. The major drawback of this method is the reduction in signal intensity in the asymmetric spin echo image due to T_2 decay.

I.7.2   Tailored Radiofrequency Pulses

Another software-based approach that has gained popularity is the use of RF pulses that are tailored to the field patterns in each subject. In Yip et al.'s method [27], 3D tailored spokes (also known as echo-volumar and fast-k_z) pulses are iteratively designed to excite a magnetization with the negative of the phase pattern caused by the susceptibility gradient. The pulse design is cast as a minimization problem and is solved iteratively using the conjugate gradient algorithm. In another approach, Yip et al. [28] proposed the use of tailored spectral-spatial pulses that exploit the approximately linear relationship between in-plane off-resonance and through-plane susceptibility difference, to selectively excite and apply precompensatory phase in the regions of signal loss. These methods are effective in mitigating signal loss in 2D imaging, but come at the expense of long pulse computation times, complicated pulse design method and/or limited control over slice profile characteristics. In another tailored RF approach, Yang et al. [29] used four-dimensional spectral-spatial pulses to simultaneously mitigate in-plane $|B_1^+|$ inhomogeneity and through-plane signal loss artifacts in T_2^*-weighted sequences. 2D spectral-spatial pulses were designed to induce compensatory phase in the desired off-resonance regions. To mitigate the $|B_1^+|$ inhomogeneity the SPSP pulses were played along a spokes trajectory, thus forming a 3D pulse. Multiple off-resonance regions were targeted by concatenating the 3D SPSP pulses, thus forming a 4D pulse. The 4D SPSP pulses were demonstrated for dual band problems where it was assumed that one off-resonance band did not need any compensation. The authors noted that the dual band design is not sufficient to compensate the signal-loss in all the brain regions. The major drawback of this method is the prohibitively long pulse durations for problems that require more than two bands.

The method proposed by us in Chapter III utilizes both patient-tailored pulses and z-shim compensatory gradients to recover signal in brain regions with through-plane suscep-tibility gradients.

I.8 Current Methods for Peak Power Reduction of Multiband Pulses

Few methods have been proposed earlier to control the peak power of multiband pulses. In this section we describe three of the popular approaches. We first describe the PINS pulses which simultaneously excite an infinite number of slices without a peak power penalty. We then give an overview of phase-optimization and time-shifting techniques that are applied on conventional multiband pulses to reduce their peak power.

I.8.1 Power Independent of Number of Slices

Norris et al. [30] have proposed the so-called PINS pulses (Power Independent of Number of Slices) that can simultaneously excite a large number of slices with the same peak RF power as a single-slice pulse. PINS pulses are theoretically obtained by multiplying a single-slice pulse with a comb function. Since the Fourier Transform of a comb function is another comb function, the slice profile of the single-slice pulse is replicated at the comb function's frequency to excite multiple slices simultaneously. From the excitation k-space perspective, PINS pulses are designed for a reduced excitation FOV which causes aliasing of the excitation pattern, consequently exciting multiple slices. From sampling theory, if the excitation trajectory is discretely sampled at $\triangle k$ resolution then the magnetization pattern will repeat infinitely with periodicity $1/\triangle k$. Therefore, to achieve a slice-gap of $\triangle z$ cm, the linear excitation k-space trajectory of a single-slice pulse should be sampled every $1/\triangle z$ cm^{-1}. This is achieved by playing a train of rectangular subpulses separated by gradient blips of area A_z given by:

$$A_z = \frac{2\pi}{\gamma} \frac{1}{\triangle z} \tag{I.25}$$

The train of hard pulses is modulated by the slice-select RF envelope to achieve the desired slice profile and flip angle. Figure I.9 illustrates a time-bandwidth product 2 PINS pulse designed to excite 3 slices of thickness 5 mm and at 3 cm slice gap.
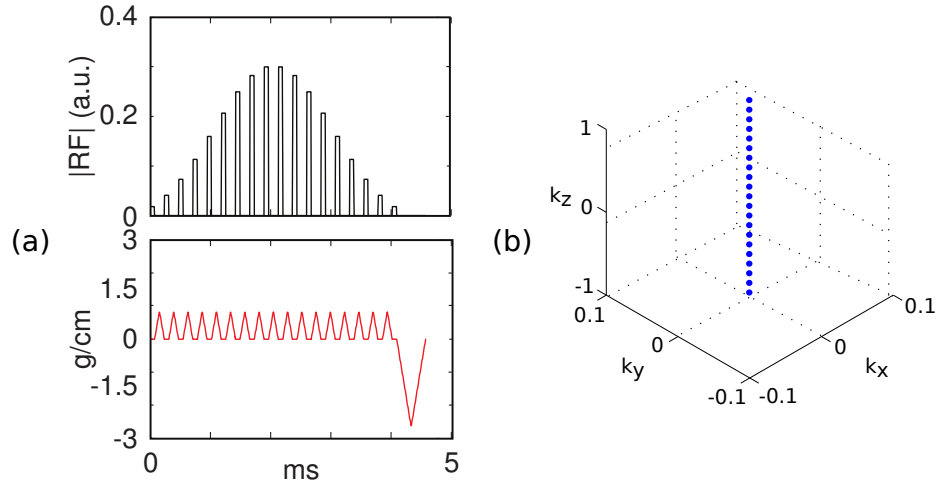
Figure I.9: Illustration of (a) PINS pulse and gradient waveform designed to excite three slices of thickness 5 mm and slice gap 3 cm and (b) the excitation k-space trajectory traversed.

The major drawbacks of PINS pulses is that they excite infinite number of slices and can have unacceptably long pulse durations due to gradient slew-rate limitations, especially for a small number of bands. The large number of excited slices are difficult to separate in reconstruction using the finite spatial encoding provided by the receive coil sensitivity. Even with large number of receive coils, use of PINS pulses is limited to saggital and coronal directions in brain imaging to keep the number of slices within reasonable limits. Nevertheless, they are often used for refocusing when a large multiband factor is desired, in combination with a conventional multiband excitation pulse. This way, signals from unwanted refocused slices are never excited and are crushed away.

I.8.2 Radiofrequency Pulse Phase Optimization

Goelman [31] and Wong [32] have independently shown that the peak power of a multi-band pulse can be reduced by introducing optimized excitation phases to each band. For certain phase combination, the pulses destructively interfere leading to a reduced peak RF

amplitude. The optimized phases α for the N_{sl} number of pulses can be obtained by solving the following minimization problem:

$$\min_{\alpha} \max_{i} \left| \sum_{m=1}^{N_{sl}} p_i^m e^{\imath \alpha_m} \right|, \tag{I.26}$$

where, p_i^m is the complex RF waveform sample for slice m at time index i. Figure I.10 shows the conventional and phase-optimized RF pulses designed to excite 5 slices at 2 cm slice gap. The slice profile shows that both the pulses excite the desired slices. The plot of increase in peak RF amplitude shows that the peak RF of conventional pulses increases linearly with the number of slices whereas peak amplitude of phase-optimized pulses increases as square root of the number of slices, hence, the peak power increases linearly.
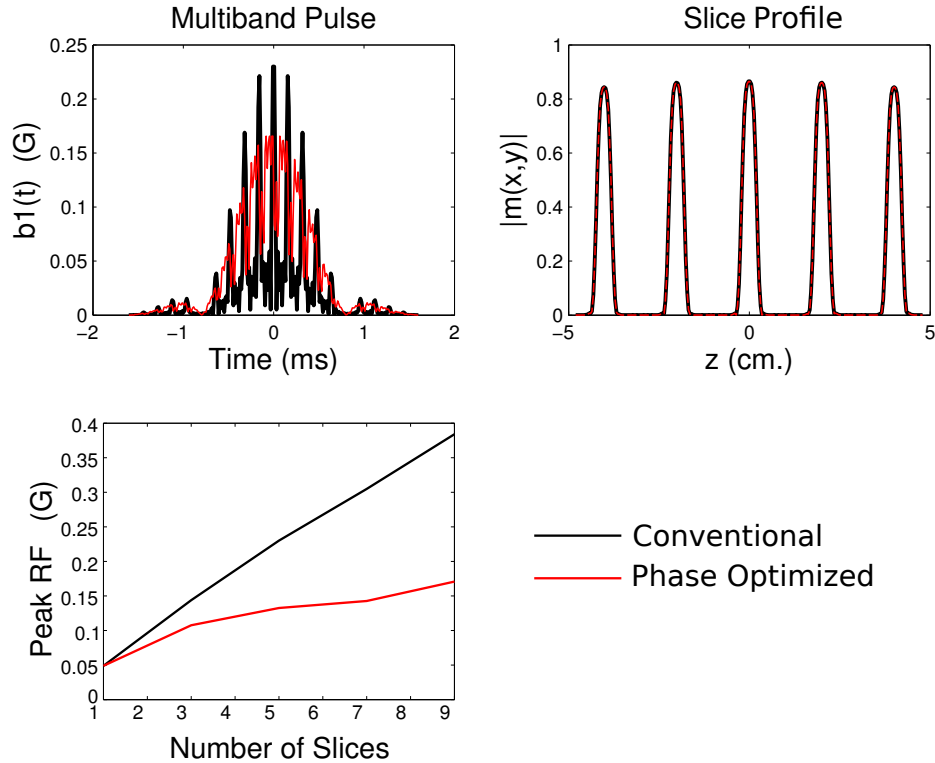
Figure I.10: Conventional and phase-optimized multiband pulses designed to excite 5 slices at 2 cm gap. The slice profile shows that both the pulses excite the desired slices. The plot of peak RF amplitude vs. number of slices demonstrates that peak amplitude of phase-optimized pulses rises more gradually than conventional pulses.

In Chapter II we propose an extension of the phase-optimization method to reduce the peak

power of multiband spokes pulses.

I.8.3 Time-shifted Radiofrequency Pulses

To reduce the peak power of multiband pulses, Auerbach et al. [33] introduced time shifts between the single-slice pulses before summing them to form the multiband pulse. For optimized time-shifts the main lobe of the pulses do not overlap in time, thus reducing the maximum amplitude of the multiband pulse. Time-shifted pulses were shown to have significantly lower peak RF amplitude compared to phase-optimization. Since the pulses are shifted in time, an asymmetric slice-select gradient moment is experienced by each pulse. Therefore, time-shifted pulses require additional pulse sequence design consideration to balance the excitation and refocusing gradient moments. For sequences such as twice-refocused spin echo and bipolar diffusion-weighted EPI the dephasing from the asymmetry of the slice-select gradient around the first refocusing pulse is cancelled by the gradient moment of the second pulse. Thus no extra consideration is required while designing multi-band pulses. But sequences such as monopolar diffusion-weighted EPI require tuning of the time-shift duration and gradient amplitude to balance the effects of the asymmetric gradient moments on each band. For $\triangle_{exc}$ and $\triangle_{ref}$ time shifts between the excitation and refocusing bands respectively, the moment of the excitation and refocusing gradients G_{exc} and G_{ref} can be balanced by satisfying the condition:

$$G_{exc}\triangle_{exc} = 2 \times G_{ref}\triangle_{ref} \qquad (I.27)$$

To balance the gradient moments in monopolar spin echo sequences, Auerbach et al. proposed two approaches that satisfy Eq. I.27. In the first approach called the "aligned echo" method, the same gradient amplitude was used for both excitation and refocusing, i.e. $G_{exc} = G_{ref}$. To satisfy Eq. I.27 the time shift between the excitation bands should be twice that between the refocusing bands so $\triangle_{exc} = 2 \times \triangle_{ref}$. Therefore, the effective TE of the bands differ by $2 \times \triangle_{ref}$ even though the spins refocus at the same time. In the

second approach called "aligned-TE", the excitation gradient amplitude is set to twice the refocusing gradient, i.e. $G_{exc} = 2 \times G_{ref}$. To satisfy Eq. I.27 the same time shift has to be applied between the excitation and refocusing bands, respectively. Therefore, all the bands have the same TE but unlike the "aligned-echo" scheme the spins refocus at different times.

Though phase-optimization and time-shift methods reduce the peak power of multiband pulses, they do not achieve feasible pulse durations for large number of slices and are thus restricted to lower SMS slice-acceleration factors. In section IV we show that for a given peak RF power, the method proposed by us can produce even shorter (roughly half the duration) multiband pulses.

CHAPTER II

Multiband spokes pulses for transmit field inhomogeneity compensation

II.1 Introduction

In this chapter we discuss the proposed multiband spokes pulses used to mitigate B_1^+ inhomogeneity in multiple simultaneously excited slices.

Previously, Wu et al [20] have described a method for RF shimming of MB pulses in both single and parallel transmit settings. They introduced two approaches to design the RF amplitude and phase weights (collectively called shim weights) called 'MB B1 Shim' and 'Full pTx MB'. In the simpler 'MB B1 Shim' approach, channel-specific RF shim weights are jointly calculated for all the excited slices. In the 'Full pTx MB' approach, the shim weights are independently calculated for each transmit channel and each excited slice. It was shown that independently designing the shim weights provides a more homogeneous flip angle pattern compared to the joint design. They also demonstrated a two-spoke extension of this concept, with fixed target phase and excitation k-space trajectory and a hard peak-power constraint built into the pulse design problem [34]. Here, we report an analogous approach to design multidimensional multiband pulses by extending the single-slice spokes [35] pulse. The proposed pulse is henceforth denoted as 'MB spokes'. In addition to the shim weights, we optimize the spokes excitation $k-$space trajectory and the target in-plane phase pattern for each slice. To design MB spokes pulses, the 'interleaved greedy and local' optimization method [8] for small-tip-angle spokes pulse design was extended to the multiband case. This method was chosen because it is computationally efficient and allows the incorporation of off-resonance effects due to main field inhomogeneity, which are amplified at high fields. It also jointly optimizes the RF pulses, the target excitation phase patterns, and the excitation k-space locations visited by the spokes trajectory. For the computation of shim weights the 'Full pTx MB' approach proposed by Wu et al [20]

was adapted for MB spokes. Wu et al also demonstrated the use of a regularization term in the pulse design cost function to control the integrated power of the shimmed MB pulse. However, this technique does not regulate peak RF power. It has been shown that peak RF power can be reduced by optimizing the relative phases of the slices excited by a multiband pulse prior to summing the pulses [32, 31]. We generalize this method to the MB spokes pulses. For a given slice, the spokes subpulses have phase relationships that are optimized to achieve a uniform excitation pattern. Therefore, directly changing the phase of the slice-select sub-pulses will destroy these inter-spoke phase relationships leading to non-uniform excitation. To address this problem we propose a straightforward extension of the optimal excitation phase method to achieve reduced peak RF power of MB spokes pulses.

In the following section, we formulate the multiband spokes pulse design as an optimization problem and layout the strategy to reduce the peak power of these pulses. We then show in 7 T in vivo experiments and single-channel and two-channel parallel transmit simulations that MB spokes pulses improve flip angle homogeneity in multiple simultaneously excited slices compared to conventional multiband excitations. It is demonstrated that spokes pulses designed using a 'Slice-Independent' design approach analogous to Wu's 'Full pTx MB' approach gives a more uniform excitation pattern than a 'Slice-Joint' design approach analogous to Wu's 'MB B1 Shim'. Simulation results show that the maximum power of peak power-minimized pulses increases more gradually with the number of excited slices than unregularized and integrated power-regularized pulses.

II.2 Theory

A spokes pulse comprises of a train of N_s slice-selective RF subpulses that are played concurrently with slice-select gradient trapezoids, and are separated in time by small transverse-plane gradient blips that move the excitation k-space trajectory to different locations in the in-slice spatial frequency dimensions. Such a pulse can be extended to simultaneously excite multiple slices by replacing the single-slice-selective subpulses with multiband wave-

forms. Here we present an extension of a single-slice spokes pulse design method [8] to multiband pulses. Though Ref. [8] describes a pulse design method for multiple off-resonance frequencies, for simplicity we will discuss the MB spokes pulse design for a single isochromat at each spatial location.

II.2.1 Slice-Independent Design of MB Spokes Pulses
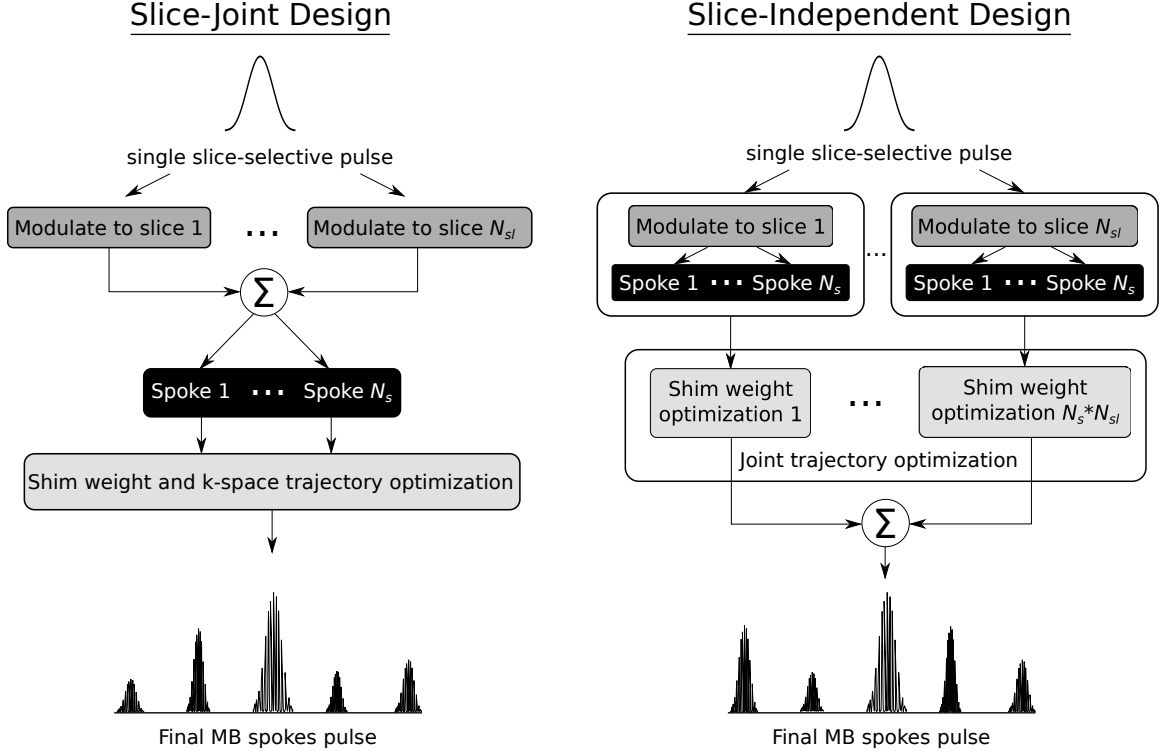
Figure II.1: Illustration of 'Slice-Joint' and 'Slice-Independent' design approaches to multiband spokes pulse design. The 'Slice-Independent' approach designs separate RF amplitude and phase weights for each single-slice subpulse, whereas in the 'Slice-Joint' approach a single amplitude and phase are determined for all slices simultaneously. Both independent and joint designs start with a single slice-selective pulse which is modulated to produce pulses for the N_{sl} number of desired slices. In the 'Slice-Joint' design approach the single-slice pulses are summed to obtain a multiband subpulse which is copied for the desired N_s number of spokes. The optimization routine optimizes the shim weight and excitation k-space trajectory of each multiband spoke to produce the final MB spokes pulse. In the 'Slice-Independent' approach the slice-select pulses are copied over to N_s spokes to produce $N_s N_{sl}$ number of subpulses. The design algorithm independently optimizes the shim weights for each of the $N_s N_{sl}$ subpulses and jointly optimizes the k-space trajectory. The final MB spokes pulse is obtained by summing the optimized slice-select spokes subpulses.

Here we introduce the 'independent shimming' approach to MB spokes pulse design that optimizes RF weights for each slice independent of the others, allowing each slice's excitation pattern to be tailored to its local B_1^+ and B_0 fields. Figure II.1 illustrates this approach in comparison to a 'joint shimming' approach wherein the spokes subpulse weights are solved for jointly across slices. We develop the pulse design problem in analogy to the conventional spokes pulse design algorithm of Ref. [8].

For N_s subpulses that simultaneously excite N_{sl} slices using N_c transmit channels, with B_1^+ fields $\{s_c^m(x,y)\}_{m=1}^{N_{sl}}$ where m is the slice index, the goal of 'independent shimming' multiband spokes pulse design is to determine $N_s N_c N_{sl}$ subpulse weights and N_s transverse-plane (k^x-k^y) excitation k-space locations to be visited by the trajectory, which together produce a uniform flip angle pattern in each slice. Adapting the notation from Ref. [8], the flip angle pattern excited in the center of slice m by a small-tip-angle single-slice spokes pulse is:

$$\theta_m(x,y) = \iota\gamma\Delta_t \sum_{n=1}^{N_s} \left(\sum_{c=1}^{N_c} b_{c,n,m} s_c^m(x,y) e^{\iota(x k_n^x + y k_n^y)} \right) \left(\sum_{i=1}^{N_t} p_i^m e^{\iota 2\pi \Delta_f^m(x,y)(i\Delta_t - (N_s - n + 1)T)} \right),$$
(II.1)

where $b_{c,n,m}$ are the complex RF shim values, p^m is a single-slice-selective small-tip-angle RF pulse for slice m, $\Delta_f^m(x,y)$ is the spatial frequency offset due to B_0 inhomogenity (Hz) in slice m, T is the duration of the subpulses, and Δ_t is the RF sampling period. In most cases, the p^m pulses will be derived by modulating the same single-slice-selective waveform p to the position z_m of each slice on the slice-select axis, as:

$$p_i^m = p_i e^{\iota\gamma G z_m t_i},$$
(II.2)

where γ is the gyromagnetic ratio, G is the gradient strength corresponding to the prescribed slice thickness, the time points t_i are referenced to the middle of the pulse, and $\iota = \sqrt{-1}$.

Discretizing each slice's pattern to N_x^m x-y locations $\{(x_j^m, y_j^m)\}_{j=1}^{N_x^m}$, Eq. II.1 can be

written in matrix-vector form as:

$$\boldsymbol{\theta}_m = \sum_{c=1}^{N_c} \boldsymbol{S}_{c,m} \boldsymbol{A}_m(\mathbb{K}) \boldsymbol{b}_{c,m}, \qquad (\text{II}.3)$$

where $\boldsymbol{S}_{c,m} = \text{diag}\{s_c(x_j^m, y_j^m)\}$, $\mathbb{K}$ is the set of excitation k-space locations visited by the pulse, $\boldsymbol{b}_c$ is a length-N_s column vector of RF weights for each channel and $\boldsymbol{A}_m(\mathbb{K})$ is an $N_x^m \times N_s$ single-slice spokes system matrix with elements:

$$\{\boldsymbol{A}_m(\mathbb{K})\}_{j,n} = \iota \gamma \Delta_t e^{\iota(x_j^m k_n^x + y_j^m k_n^y)} \sum_{i=1}^{N_t} p_i^m e^{\iota 2\pi (\Delta_f(x_j^m, y_j^m)(i\Delta_t - (N_s - n + 1)T))}. \qquad (\text{II}.4)$$

We note that N_x^m counts the number of voxels containing tissue in slice m, and can be different for each slice. For N_c transmit channels a combined system matrix for slice m, denoted $\tilde{\boldsymbol{A}}_m(\mathbb{K})$, is constructed as:

$$\tilde{\boldsymbol{A}}_m(\mathbb{K}) = \begin{bmatrix} \boldsymbol{S}_{1,m} \boldsymbol{A}_m(\mathbb{K}) & \cdots & \boldsymbol{S}_{N_c,m} \boldsymbol{A}_m(\mathbb{K}) \end{bmatrix}, \qquad (\text{II}.5)$$

and a single length-$N_s N_c$ column vector of RF weights for slice m is similarly constructed by concatenating the $\boldsymbol{b}_c$ vectors:

$$\tilde{\boldsymbol{b}}_m = \begin{bmatrix} \boldsymbol{b}_{1,m}^T & \cdots & \boldsymbol{b}_{N_c,m}^T \end{bmatrix}^T. \qquad (\text{II}.6)$$

With these definitions $\boldsymbol{\theta}_m$ can be equivalently written as:

$$\boldsymbol{\theta}_m = \tilde{\boldsymbol{A}}_m(\mathbb{K}) \tilde{\boldsymbol{b}}_m. \qquad (\text{II}.7)$$

With the discretized system model defined, the MB spokes pulse design problem is cast as a penalized least squares problem:

$$\min_{\boldsymbol{k}, \tilde{\boldsymbol{b}}, \boldsymbol{\phi}} \sum_{m=1}^{N_{sl}} \left[\frac{1}{2} ||\tilde{\boldsymbol{A}}_m(\mathbb{K}) \tilde{\boldsymbol{b}}_m - \boldsymbol{d}_m(\phi_m)||^2 + \frac{\lambda}{2} ||\tilde{\boldsymbol{b}}_m||^2 \right] \qquad (\text{II}.8)$$

where $\boldsymbol{d}_m$ is the length-N_x^m desired flip angle pattern vector for each slice, with target phase ϕ_m. For B_1^+ inhomogeneity-compensating pulse design the $\boldsymbol{d}_m$ patterns have uniform magnitude inside the brain masks of all the slices, and ϕ_m is optimized independently for each slice. The second term in the objective function is a Tikhonov regularizer that penalizes the ℓ_2 norm of each slice's RF weights, where λ is a tunable factor that determines the relative weighting given to the regularization term. In the Appendix, we show that $\sum_{m=1}^{N_{sl}} \|\tilde{\boldsymbol{b}}_m\|^2$ is proportional to the integrated power of the combined time-domain pulses, summed across coils.

The design problem in Eq. II.8 is solved using the interleaved greedy and local optimization method for single-slice spokes design [8]. In each iteration the RF weights $\tilde{\boldsymbol{b}}_m$ are calculated slice-by-slice by calculating the pseudo-inverse of each slice's contribution to the objective function. The target phase profiles ϕ_m are updated slice-by-slice using Eq. 6 from Ref. [8]. The excitation k-space locations $\mathbb{K}$ of the spokes are updated using Eq. 9 from Ref. [8], where all the slices contribute to the derivative calculations. Once the algorithm converges to the optimal shim values $\{\tilde{\boldsymbol{b}}_m\}_{m=1}^{N_{sl}}$, the MB spokes pulses for each transmit channel are computed by summing the individual spokes pulses across slices.

II.2.2 Peak Power Minimization

The peak power of a conventional multiband pulse can be minimized by applying optimized excitation phases to each band [31, 32]. This strategy can be extended to MB spokes by optimizing the relative phases of the individual slices' spokes pulses. After the 'interleaved greedy and local optimization' method has converged to obtain the shim weights $\{\tilde{\boldsymbol{b}}_m\}_{m=1}^{N_{sl}}$, excitation phases that reduce the peak power can be obtained by solving the optimization problem:

$$\min_{\boldsymbol{\alpha}} \max_{n,c,i} \left| \sum_{m=1}^{N_{sl}} p_i^m b_{c,n,m} e^{\iota\alpha_m} \right|, \tag{II.9}$$

where p_i^m is sample i of the slice-select pulse for slice m and the 'max' operation returns the maximum RF amplitude across spokes (n), coils (c), and time points (i), after summing the

individual N_{sl} slice-selective spokes pulses. This problem can be solved to obtain the N_{sl} optimal excitation phases $\{\alpha_m\}_{m=1}^{N_{sl}}$ using the MATLAB (MathWorks Inc., Natick, MA, USA) `fminsearch` function (Nelder-Mead simplex [36]). A feature of this method is that it does not require hand-tuning of regularization.

II.2.3 Overall Algorithm

The overall pulse design approach described here has two steps. In the first, the extended interleaved greedy and local spokes pulse design method is used to solve for $\mathbb{K}$, $\{\tilde{\boldsymbol{b}}_m\}_{m=1}^{N_{sl}}$, and $\{\phi_m\}_{m=1}^{N_{sl}}$. The output of this step is a set of spokes pulses for each slice that have been regularized for low integrated RF power. These spokes pulses are input to the second step which solves for the optimal phases $\{\alpha_m\}_{m=1}^{N_{sl}}$ using the method described above to reduce the peak power of the slice-combined pulses.

II.3 Methods

II.3.1 Pulse Design Parameters

The following simulations and experiments were carried out with conventional MB and MB spokes pulses designed in MATLAB running on a MacBook Air computer (Apple Inc., Cupertino, CA, USA) with a 1.7 GHz Intel Core i7 processor and 8 GB RAM. All slice-selective subpulses were designed using the Shinnar-Le Roux [15] algorithm and had a time-bandwidth product of 2. Flyback spokes trajectories were used, and RF and gradient waveforms were sampled with a dwell time of 6.4 μs. All gradient trapezoids were designed subject to a maximum amplitude of 15 mT/m and maximum slew rate of 120 T/m/s. For 'Slice-Independent' MB spokes designs, peak power minimization was implemented by initializing the α_m to zero, and applying MATLAB's `fminsearch` to optimize them using 30 restarts, each with its own uniformly-distributed random initialization. Unless otherwise noted, MB spokes pulses comprised five spokes subpulses of duration 1.8 ms each, and had a total duration of 8.8 ms. Figures II.3(c,d) show that the knees of the flip angle standard deviation and power versus number of spokes curves occur around five spokes,

indicating that this number of spokes gives a good balance between flip angle uniformity, power, and pulse duration.

II.3.2   Simulations

II.3.2.1   Peak Power Minimization

The peak power minimization strategy was tested in simulations of single-channel transmit and two-channel parallel transmit by measuring the increase in peak RF power of MB spokes pulses with the number of excited slices. Pulses were designed with the 'Slice-Independent' approach to excite a flip angle of 30 degrees in three to nine axial brain slices of 3 mm thickness. The B_1^+ maps for pulse design were measured in a healthy volunteer in 9 axial brain slices with a slice gap of 10 mm and slice thickness of 2 mm on a 7 T Philips Achieva scanner (Philips Healthcare, Cleveland, OH, USA) with a 32 receive channel head coil and a two-channel birdcage transmit coil (Nova Medical Inc., Wilmington, MA, USA), with the approval of the Institutional Review Board at Vanderbilt University. The 'STE first' DREAM B_1^+ mapping sequence [37] was used to map each transmit channel independently, where the nominal flip angle of the stimulated echo preparation pulse was 40 degrees and the flip angle of the imaging pulse was 15 degrees. The maps were acquired over a 20×20 cm in-plane field-of-view (FOV) and a 64×64 matrix size. The increase in peak RF amplitude versus number of excited slices was compared among pulses designed with no power regularization, integrated power regularization only, and integrated power regularization plus peak power minimization. The pulses with no regularization were computed by setting $\lambda = 0$ in Eq. II.8. The integrated power-regularized-only pulses were computed by skipping the peak power minimization step.

II.3.2.2   'Slice-Joint' versus 'Slice-Independent' Design

To investigate the advantages of the 'Slice-Independent' design approach, pulses designed by that method were compared with pulses designed using the 'Slice-Joint' approach. Pulses with 1 to 50 spokes subpulses were designed to excite three slices at 20 mm slice

gap, and the predicted flip angle standard deviation and integrated and peak RF powers were recorded for the comparison.

II.3.3   In Vivo Experiments

In vivo experiments were performed in 2 subjects at 7 T, using the same two-channel Nova birdcage coil driven in its single-channel circularly-polarized mode. Experiments were performed in axial and coronal orientations. B_1^+ and off-resonance maps were measured for 3 slices spaced 2 cm apart in the axial orientation and 3 cm apart in the coronal orientation with 64×64 matrix size. The in-plane FOV's were 20×20 cm for axial slices and 21×21 cm for coronal slices. The Bloch-Siegert [38] method with optimized encoding pulses [39] was used for B_1^+ mapping, and off-resonance maps were measured using the double echo-time (TE) method [40] with a TE difference of 1 ms. A tissue mask was formed for pulse design for the transverse slices by manually choosing a threshold level. Since brain masks are more difficult to form manually in coronal slices, the Otsu's image segmentation algorithm [41] was used to automatically calculate thresholds. Conventional MB pulses and MB spokes pulses with the 'Slice-Independent' approach were designed to excite a flip angle of 75 degrees in the three slices with thickness 3 mm each.

Images were collected using the pulses for excitation, followed by a 3D gradient echo readout with 144×144 matrix size and TR/TE of 150/6.8 ms. The flip angle excited by the pulses was measured using a 3D gradient echo Actual Flip Angle (AFI) [42] mapping sequence with $6 \times 6 \times 3$ mm resolution, 114×114 matrix size and TE/TR$_1$/TR$_2$ of 7.3/100/400 ms. Due to slice profile effects [43] the measured AFI maps were biased down, so the maps were normalized by their median value for comparison to the predicted patterns. Aliased slice images were also acquired by exciting with multiband pulses followed by a 2D Cartesian readout. The aliases were separated using the slice-GRAPPA reconstruction algorithm [1]. Calibration data for the GRAPPA kernel were calculated from 3D images acquired using the conventional multiband and MB spokes pulse, respec-

tively. The separated images were normalized by the coil receive sensitivity maps which were estimated by dividing out the B_1^+ maps from low-resolution small-tip single-spoke images.

II.4 Results

II.4.1 Simulations

II.4.1.1 Peak Power Minimization
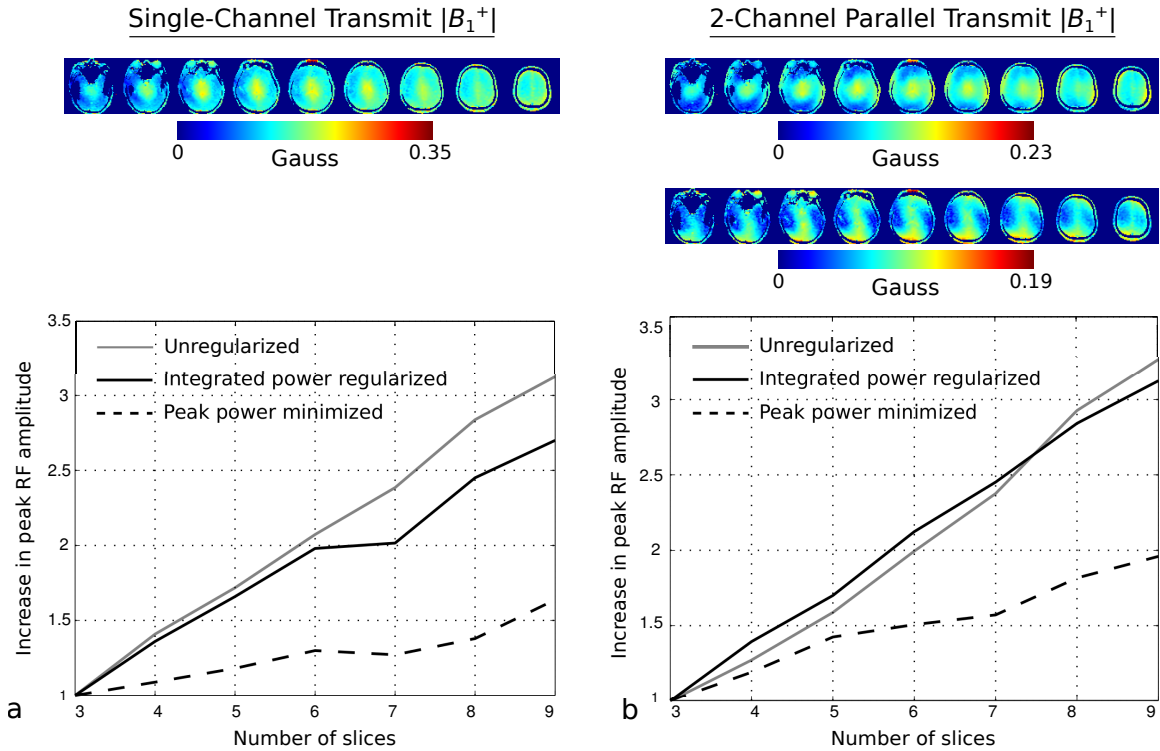
Figure II.2: Increase in peak RF amplitude of 5 MB spokes pulses using 'Slice-Independent' design versus number of excited slices. Peak RF power of the unregularized, integrated power-regularized and peak power-minimized MB spokes pulses are compared. Single channel and parallel transmit B_1^+ maps and simulation results are shown for a target mean flip angle of 30 degrees. (a) Single transmit channel results: The peak power-minimized pulses show a drastic reduction of peak power compared to the unregularized and integrated power regularized pulses. (b) 2-channel parallel transmit results: Again, the peak power-minimized parallel transmit MB spokes pulses have the lowest peak RF amplitude.

Figure II.2(a) shows a plot of the increase in peak RF amplitude versus number of excited slices for the unregularized, the integrated power-regularized and the peak power-minimized single-channel MB spokes pulses. The peak amplitudes of the unregularized and integrated power-regularized pulses rise almost linearly with the number of slices. In comparison, the peak power-minimized pulses show a more gradual increase, and a 9-slice pulse had only $1.64\times$ higher peak amplitude than a 3-slice pulse. As expected, the peak power minimization did not increase the integrated power of the MB spokes pulse.

Figure II.2(b) shows the same plot for the two-channel parallel transmit MB spokes pulses. The peak power-minimized pulses showed the most gradual increase in peak power with the number of slices, and a 9-slice pulse had only $1.96\times$ higher peak amplitude than a 3-slice pulse. As expected, the peak power minimization did not increase the integrated power of the parallel transmit MB spokes pulse.

II.4.1.2 'Slice-Joint' versus 'Slice-Independent' Design

Figure II.3(b) shows that among conventional multiband, 'Slice-Joint' and 'Slice-Independent' MB spokes pulses, the 'Slice-Independent' MB spokes pulses produced qualitatively the most homogeneous excitation patterns.
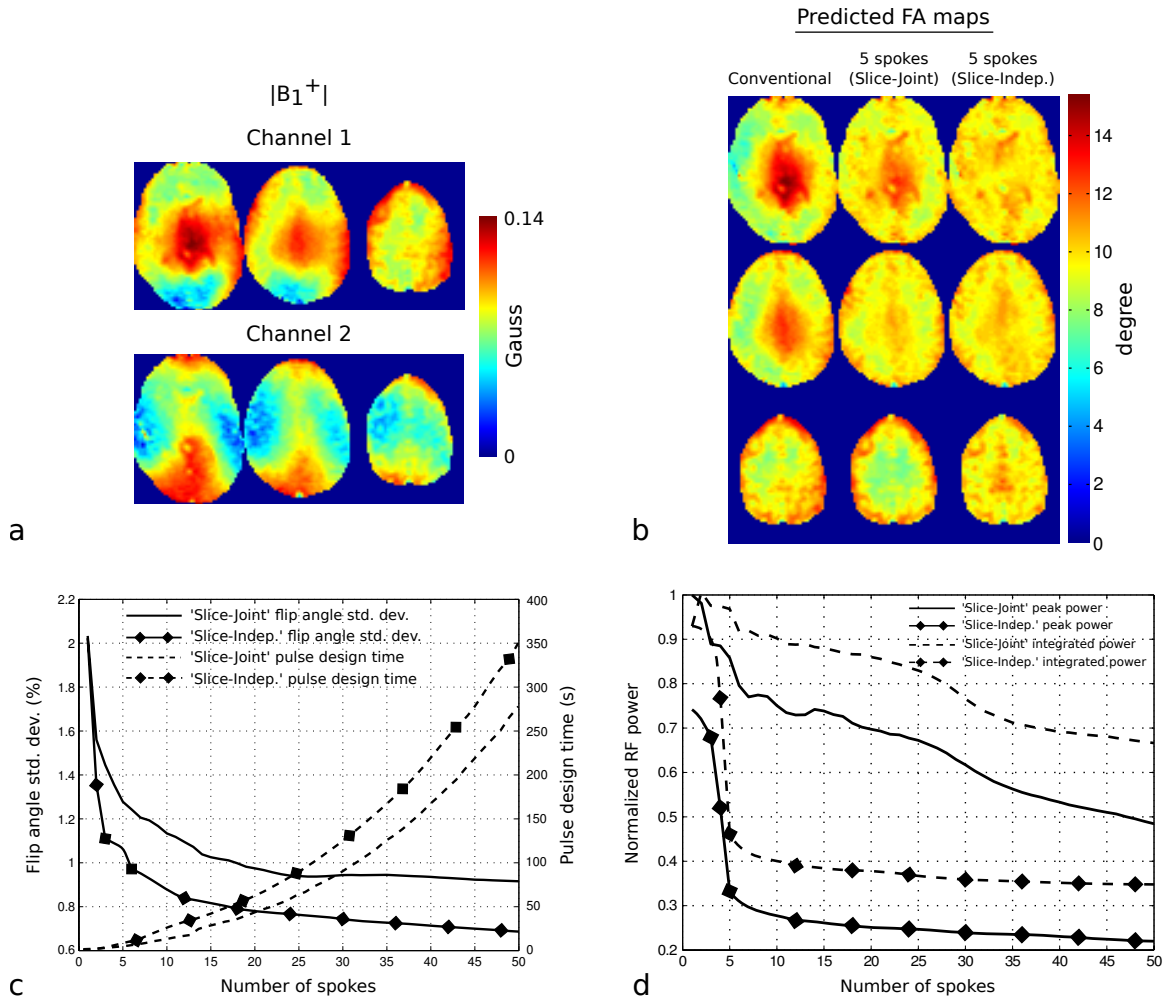
Figure II.3: Parallel transmit simulations using measured B_1^+ maps of a 2-channel head volume coil, shown in (a). (b) The 5 spokes 'Slice-Independent' approach yields more uniform patterns compared to 'Slice-Joint' design. (c) Plot of predicted flip angle standard deviation versus number of spokes for 2-channel 'Slice-Joint'- and 'Slice-Independent'-designed pulses. For any given number of spokes, the 'Slice-Independent' approach has the lowest flip angle standard deviation. Pulse design times are also shown. The design times for the 5-subpulse MB spokes pulse with 'Slice-Joint' and 'Slice-Independent' design were 3.4 s and 6.2 s, respectively. (d) Plot of normalized integrated and peak RF powers versus number of spokes for the 'Slice-Joint'- and 'Slice-Independent'-designed pulses. For any given number of spokes, the 'Slice-Independent' method produces pulses with lower integrated and peak power than the 'Slice-Joint' approach.

The plot of flip angle standard deviation versus number of spokes in Fig. II.3(c) shows that for any given number of spokes the 'Slice-Independent'-designed two-channel MB spokes pulse produced a more uniform excitation compared to the 'Slice-Joint'-designed

pulse. As more spokes are added the flip angle standard deviation is reduced for both the methods. The pulse design times are also shown. The design times for the 5-spoke MB spokes pulses with 'Slice-Joint' and 'Slice-Independent' design were 3.4 s and 6.2 s, respectively. The mean compute time for peak-power optimization was 0.17 s. Figure II.3(d) shows that for any given number of spokes the 'Slice-Independent'-designed pulses have lower integrated and lower peak power than the 'Slice-Joint'-designed pulses.

II.4.2 Experiments

Figures II.4 and II.5 show results from axial and coronal head scans conducted in two human subjects.
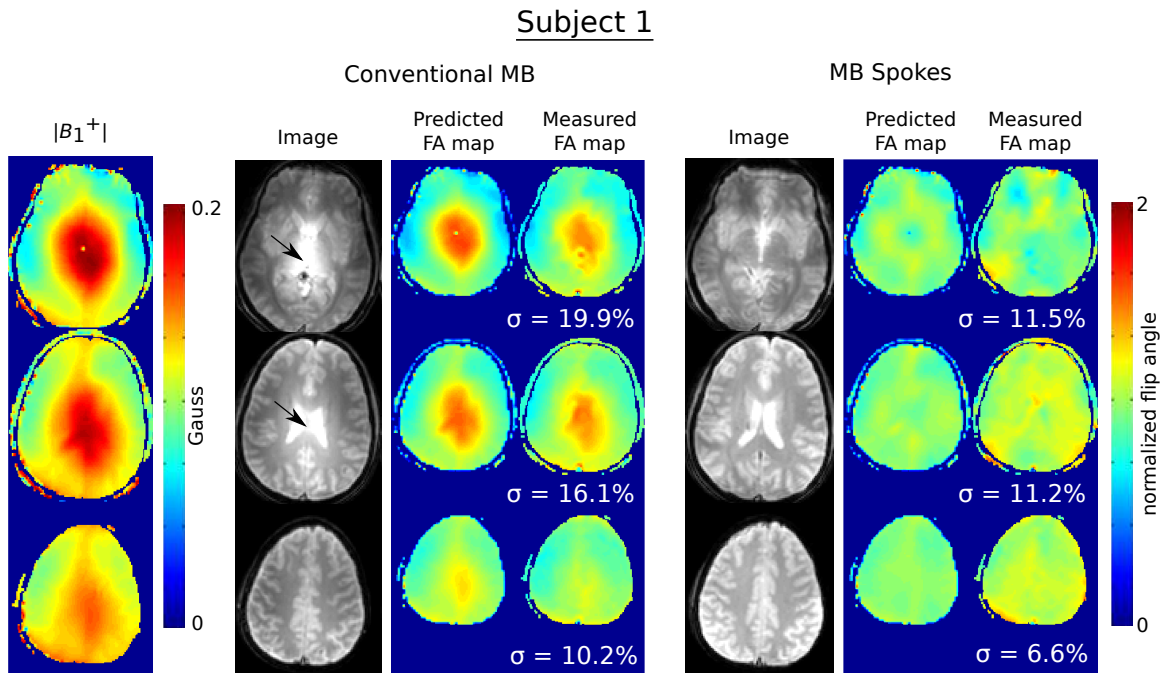
Figure II.4: B_1^+ maps, images and predicted and measured flip angle maps from in vivo axial slices. Excitations using conventional MB and MB spokes pulses with 5 subpulses and 'Slice-Independent' design are compared. Arrows point to regions with center brightening artifact in conventional MB images which are reduced when the MB spokes pulse is used for excitation. The measured AFI maps match well with the predictions and MB spokes show a more uniform excitation pattern than conventional MB pulse. The flip angle standard deviation was lower for all the slices acquired using MB spokes pulse compared to conventional MB.

In both subjects the MB spokes images show a significant reduction in the center brightening artifact which obscures the anatomical information near the center of the brain when conventional MB pulses are used. Both axial and coronal MB spokes patterns show a significant improvement over the conventional MB patterns which are marred by the center-brightening artifact caused by the non-uniform B_1^+ field. The flip angle standard deviation is smaller in all the slices with MB spokes pulses. Compared to conventional pulses, in the MB spokes patterns the flip angle standard deviation was reduced by 31.2% averaged across all the slices in both the subjects. Also, the measured patterns match well with the predictions.
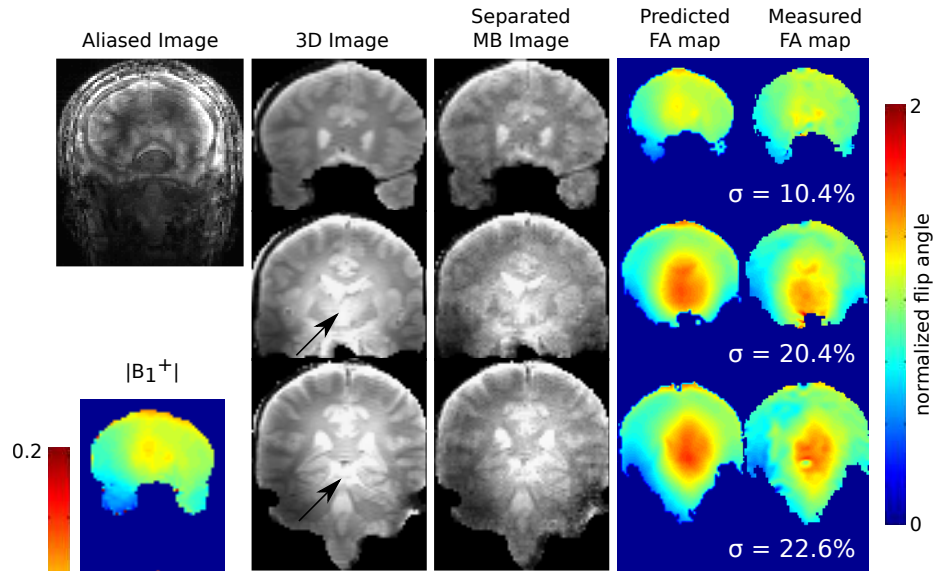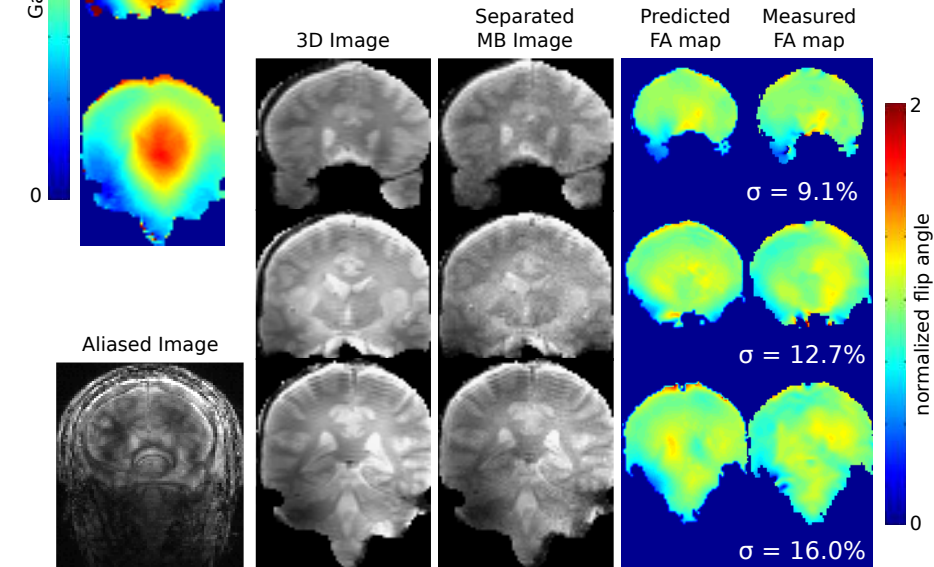
Figure II.5: B_1^+ maps, images and predicted and measured flip angle maps from in vivo coronal slices. Excitations using conventional MB and MB spokes pulses with 5 subpulses and 'Slice-Independent' design are compared. Acquired aliased images, 3D images and slice images separated using slice-GRAPPA [1] reconstruction are shown. Arrows point to center brightening in conventional multiband images that are reduced when the MB spokes pulse is used for excitation. The separated images match well with the acquired 3D images. The measured AFI maps match well with the predictions and MB spokes show a more uniform excitation than conventional MB pulses. The flip angle standard deviation was lower for all the slices acquired using MB spokes pulse compared to conventional MB.

Figure II.5 also shows the slice images separated in reconstruction along with the acquired 3D and aliased images. The reconstructed slice images show good correspondence with the 3D images and in both cases the MB spokes pulse gives a reduced center brightening artifact compared to images excited with the conventional pulse.

II.5 Discussion

We have introduced an approach to design multi-dimensional multiband excitation pulses that mitigate flip angle variations due to inhomogeneous B_1^+ fields in multiple simultaneously-excited slices. MB spokes have all the advantages of the pulses proposed by Wu et al in Ref. [20] when designing small-tip pulses and also inherit the benefits of the interleaved and greedy method from Grissom et al [8]. The pulses can also be implemented with a single transmit channel.

Though bipolar gradients enable shorter pulse durations, flyback gradients were used in the presented results since it was found that the excitation patterns produced by pulses with bipolar gradients were degraded in comparison. We believe those errors were primarily due to zeroth- and first-order eddy current effects, which could be compensated using gradient trajectory measurement [44] or predistortion [45, 46]. The proposed algorithm is fully compatible with bipolar gradient trajectories.

The results from our single-channel experiments show that 'Slice-Independent'-designed MB spokes pulses yield reduced center brightening compared to conventional MB pulses. The pulses can be implemented with a single transmit channel. In the slice-GRAPPA [1] reconstructions of $3\times$ slice-accelerated acquisitions using MB spokes excitations, the separated slices show a reduction in the center-brightening compared to conventional multiband pulse excitations.

The integrated RF power was minimized using a regularization scheme and we proposed a straightforward method to minimize the peak power of the pulses. This approach was taken because it is simple to implement and worked consistently in all simulations and

experiments. An alternative approach would be to extend the pulse design problem (Eq. II.8) to incorporate a peak-power regularization term in the cost function directly, which may enable still lower peak power via simultaneous adjustment of k-space locations, target excitation phase, and subpulse weights, at the cost of increased algorithm complexity [34]. The additional regularization term would be:

$$\frac{\beta}{2} \max_{n,c,i} \left| \sum_{m=1}^{N_{sl}} p_i^m b_{c,n,m} \right|.$$ (II.10)

A problem formulation with a hard peak power constraint could also be used. Another approach to reducing the peak power of multiband RF pulses is to shift the pulses in time with respect to each other, so that their main lobes do not overlap [47]. This approach could be incorporated into the proposed MB spokes design algorithm by replacing the slice-selective subpulses for each slice with time-shifted pulses. We note that constraining the peak power of the multiband pulse does not directly limit the local and global SAR values, which can be explicitly controlled by incorporating SAR matrices in the pulse design problem [48].

II.6 Conclusions

We have presented a fast method to design low peak power patient-tailored multiband spokes pulses to mitigate B_1^+ inhomogeneity at high field. In vivo experiments showed that the MB spokes pulses improve the flip angle homogeneity in all excited slices. Compared to conventional pulses, with a 5-subpulse MB spokes pulse the flip angle standard deviation was reduced by 31.2% averaged across all the slices in all the subjects. Simulations with in vivo field maps demonstrated that the algorithm was able to mitigate increased peak RF power as the number of excited slices increased. For a peak-power minimized two-channel pulse that excites 9 slices, the peak amplitude increased by $1.96\times$ of the peak amplitude of a 3-slice pulse, compared to $3.27\times$ for an unregularized MB spokes pulses. The use of multiple transmit channels further improved the performance of MB spokes pulses. Simulation results show that a MB spokes pulse with 5 subpulses gave a flip angle standard

deviation of 1.1%. MB spokes pulses are expected to be most useful for applications such as high field BOLD fMRI and diffusion weighted imaging (DWI) where multiple slices need to be imaged within a short acquisition time window.

II.7   Appendix

When designing an MB spokes pulse it is desirable to regularize the integrated power or ℓ_2 norm of the combined time-domain MB waveform. In the proposed algorithm, we regularize the ℓ_2 norm of the shim weights, and it is not immediately apparent that the two norms are proportional to each other due to complex interference between the individual slices' waveforms. In Ref. [20], Wu et al state that the two norms are proportional to each other due to Parseval's relation. Here we provide a mathematical proof of this fact.

The total integrated power of an N_c-channel/N_s-spoke combined time-domain MB spokes pulse is:

$$\sum_{c=1}^{N_c} \sum_{n=1}^{N_s} \left\| \sum_{m=1}^{N_{sl}} \boldsymbol{p}^m b_{c,n,m} \right\|^2, \tag{II.11}$$

where $\boldsymbol{p}^m$ is a single-slice-selective pulse vector for slice m. In the small-tip-angle regime, the slice profile of an MB pulse is its Fourier transform, whose calculation we can represent here by multiplication with a discrete Fourier transform matrix $\boldsymbol{Q}$. Because $\boldsymbol{Q}'\boldsymbol{Q} = \boldsymbol{I}$, we can insert the $\boldsymbol{Q}$ matrix into each term in Eq. II.11 and use Parseval's theorem to get:

$$\left\| \sum_{m=1}^{N_{sl}} \boldsymbol{p}^m b_{c,n,m} \right\|^2 = \left\| \boldsymbol{Q} \sum_{m=1}^{N_{sl}} \boldsymbol{p}^m b_{c,n,m} \right\|^2 \tag{II.12}$$

$$= \left\| \sum_{m=1}^{N_{sl}} \boldsymbol{Q} \boldsymbol{p}^m b_{c,n,m} \right\|^2 \tag{II.13}$$

$$\approx \sum_{m=1}^{N_{sl}} \left\| \boldsymbol{Q} \boldsymbol{p}^m b_{c,n,m} \right\|^2, \tag{II.14}$$

where the last approximation assumes that non-zero regions of the slice profiles do not overlap. This approximation applies to pulses exciting well-separated slice profiles whose stopband ripples decay rapidly away from the edges of the passbands. In this paper, pulses

were designed using the SLR algorithm with a least-squares filter design [15], which produces approximately quadratic stopband ripple decay. Each term in Eq. II.14 can be expanded as:

$$\sum_{m=1}^{N_{sl}} \|Q p^m b_{c,n,m}\|^2 = \sum_{m=1}^{N_{sl}} b_{c,n,m}^* (p^m)' Q' Q p^m b_{c,n,m} \qquad \text{(II.15)}$$

$$= \sum_{m=1}^{N_{sl}} b_{c,n,m}^* (p^m)' p^m b_{c,n,m} \qquad \text{(II.16)}$$

$$= \sum_{m=1}^{N_{sl}} |b_{c,n,m}|^2 \|p^m\|^2 \qquad \text{(II.17)}$$

$$\propto \sum_{m=1}^{N_{sl}} |b_{c,n,m}|^2 , \qquad \text{(II.18)}$$

where the last proportionality follows from the assumption that the individual slice's pulses differ only in their phase modulation, so their ℓ_2 norms are the same. Based on this result we conclude that the ℓ_2 norm of all the $N_c N_s N_{sl}$ weights $\sum_{m=1}^{N_{sl}} \|\tilde{b}_m\|^2$ is proportional to the ℓ_2 norm of the full time-domain MB subpulses, summed across transmit channels, so appending this regularizer to the objective function for pulse design is equivalent to regularizing the total integrated power of the time-domain MB pulses.

Two remarks can be made regarding generalizability of this result. First, in going from Eq. II.17 to Eq. II.18 we assumed that the ℓ_2 norms of the p^m waveforms are the same. It would be straightforward to accommodate different pulse shapes for each slice (which could have different ℓ_2 norms) by implementing Eq. II.17 as the regularizer, which corresponds to a diagonally-weighted norm with different weights for each slice. Those weights could be absorbed into slice-specific Tikhonov regularization parameters $\lambda_m \triangleq \|p^m\|^2 \lambda$. With this modification Eq.[4] could still be solved slice-by-slice for the optimal shim weights as was done in the present work. The second remark is that although we assumed small-tip-angles when we inserted the DFT matrix into the norm in Eq. II.12, in most design scenarios the separation of the slice profiles calculated by DFT would approximately hold also for large-tip-angle pulses, since the stopbands of large-tip-angle slice-selective

pulses stay in the small-tip-angle regime [15]. Therefore, this same regularizer may also be useful to mitigate integrated RF power in the design of large-tip-angle MB spokes pulses.

CHAPTER III

Multispectral z-shimming to mitigate through-plane signal loss in functional MRI

III.1   Introduction

In this chapter we present a novel approach to mitigate through-plane signal loss in the brain at the air-tissue interfaces due to susceptibility differences.

Several methods have been previously proposed to recover the lost signals. The most common solution is simply to reduce the TE at the cost of sensitivity to magnetic susceptibility differences. Additionally, as early as 1988 and 1999, Young et al. [21] and Jesmanowicz et al. [49] respectively proposed the simple approach of thin-slice averaging. In this approach, multiple thin slices are acquired and averaged to cover the desired imaging slice thickness. Though simple and effective in reducing the signal void, this method leads to increase in scan time and reduced SNR, both of which are detrimental to fMRI scans which require high temporal resolution and high SNR. Another straightforward solution, proposed by Constable is the so called 'z-shim' [23] gradient compensation wherein a gradient waveform in played along the slice dimension to cancel the phase accumulated due to the susceptibility difference at TE. Multiple images are acquired with different z-shim moments and are combined in reconstruction to form one image with nominally no signal loss artifact. However, a significant drawback of the method is that the z-shimmed images must be acquired in separate repetition times (TR) to maintain full signal. This is not suitable for the high temporal resolution requirement of fMRI scans. Some variants of z-shim such as z-shimmed single-shot EPI [24] and spiral image acquistion method [25], and Z-SAGA [26] have also been proposed. These methods suffer from long readout times and different T_2^* weighting of the shimmed regions. The latter effect is undesirable, and will lead to spatially-varying intravascular and extravascular weighting of BOLD contrast [50, 51]. Other pulse sequence based approaches include the use of tailored RF pulses such

as quadratic phase pulses [52], spokes pulses [27], optimized spectral-spatial pulses [28] and parallel transmit pulses optimized for both B_1^+-inhomogeneity and signal loss compensation [53]. These methods though effective in mitigating signal loss artifacts, come at the expense of long pulse computation times, complicated pulse design methods and limited control over slice profile characteristics.

In this work, we propose the use of spectral-spatial pulses [54] along with z-shimming to selectively excite and rewind the spin isochromats in the different regions of signal loss in a slice. The approximately linear relationship between the through-plane susceptibility difference induced gradient and in-plane off-resonance frequency is exploited to design spectral-spatial pulses that target the different regions, based on the range of off-resonance frequencies in each region. The z-shim gradient is optimized by evaluating a range of gradient moments in simulation and choosing the solution that recovers the most signal in the target region. Since the spectral-spatial pulse and z-shim combinations excite and refocus spatially disjoint regions, they are treated as different slices of a multislice stack, like the fat and water multispectral imaging method proposed by Meyer et al. [54]. Hence the method is named multispectral z-shim or MS z-shim in short.

Here, we outline the theory of this improved approach. Subsequently, structural imaging experiments performed in 15 subjects at 3 T are used to confirm the predicted signal improvements, and demonstrate that the MS z-shim method recovers signal in the regions of loss while maintaining signal elsewhere in the slice. In comparison, the conventional z-shim method loses signal in the regions with no susceptibility difference when the scan time is matched between the two methods. This is one of the major advantages of the MS z-shim method. We also demonstrate that MS z-shim can incorporate three frequency bands or signal loss regions within the same TR as a two band sequence. The use of three bands allowed signal recovery over a larger area of the slice without requiring tripling of scan time as would be required to maintain the same signal levels using conventional z-shim. GRE images acquired in multiple brain slices in one of the subjects show that MS z-shim

recovers signal and gives higher signal levels than conventional z-shimming. Finally, globally vasoactive breath-hold BOLD fMRI experiments were performed to demostrate that similar to conventional z-shimming, MS z-shim recovers temporal SNR (tSNR) and neuronal activation in the regions of signal loss but unlike conventional z-shim, MS z-shim maintains tSNR and activation in the rest of the slice.

III.2 Theory

III.2.1 Susceptibility Difference Induced Signal Loss

When two materials with different magnetic susceptibilities χ are placed in a magnetic field of strength B_0, a magnetic field gradient $G_z = \frac{d\chi}{dz}B_0$ is created at their interface. In the human head, large magnetic susceptibility differences occur at the air-tissue interface in the sinuses and the middle ear canal. If the susceptibility-difference at these air-tissue interfaces is approximated to be linear across the voxel, then the through-plane phase ϕ_{z_i} accumulated at slice location z_i and the transverse magnetization M_{T_E} at the end of echo time are given by:

$$
\begin{aligned}
\phi_{z_i}(x,y,z) &= \gamma G_z(x,y,z_i)z_i T_E \\
M_{T_E}(x,y,z) &= M(x,y,z)e^{-\iota\phi_{z_i}(x,y,z)}
\end{aligned}
\tag{III.1}
$$

where γ is the gyromagnetic ratio, $G_z(x,y,z_i)$ is the through-plane gradient at axial location z_i and $M(x,y,z)$ is the transverse magnetization immediately after excitation. The size of the through-plane gradient G_z increases with field strength B_0, leading to large gradients at high field strengths (≥ 3 T). This, combined with the long echo times of 25-50 ms in fMRI acquisitions, leads to through-plane intravoxel dephasing between excitation and readout and complete signal cancellation near air-tissue interfaces.

III.2.2 Conventional Z-shimming

In the conventional z-shim method [23], a precompensatory gradient with a moment of $-G_z T_E$ is played after the excitation pulse to cancel out the through-plane phase accumulated due to the susceptibility difference. The z-shim gradient rewinds the spins in the

regions of signal loss but causes spin dephasing in the rest of the slice. Multiple images with different z-shim gradient moments are acquired and combined in reconstruction to form one image with nominally no signal loss artifact. Since the entire slice is excited to collect an image for each gradient moment, it is necessary to wait a full TR between the z-shim acquisitions to maintain full SNR. Thus scan duration is increased by a factor of the number of z-shims required to recover signal in the entire slice. The long scan durations in the conventional z-shim approach is unacceptable for fMRI which demands a high temporal resolution to adequately sample the neuronal hemodynamic response function.

III.2.3 Multispectral Z-shimming

Analogous to multislice imaging, Meyer et al. [54] proposed a multispectral acquisition scheme wherein water- and fat-selective spectral-spatial pulses were used to acquire images containing only water or only fat. Since spectral-spatial pulses are selective in both space and frequency, the acquisition yields both water-only and fat-only images from a desired slice within the same TR without a SNR penalty. In the proposed method, instead of collecting images of water and fat, a multispectral acquisition is used to selectively acquire signal from individual signal loss regions, and a z-shim gradient is applied in each acquisition that is optimized for the region being imaged. This is possible because the through-plane susceptibility difference-induced gradient through a voxel is correlated with its off-resonance frequency, which was previously demonstrated by Yip et al [28]. Therefore, the measured field offset map $\triangle f_z$ can be used to predict the through-plane gradient in each voxel in a slice. The through-plane phase ϕ_{z_i} at TE can be rewritten as

$$\phi_{z_i}(x,y,z) = \gamma\alpha \triangle f_z(x,y,z_i)z_i T_E, \qquad (\text{III.2})$$

where α is the proportionality constant that relates G_z and $\triangle f_z$. Figure III.1 shows the proposed MS z-shim sequence where the $\triangle f_z$ map is segmented into N_b distinct frequency bands, each of which is selectively excited using a spectral-spatial pulse followed by a

56
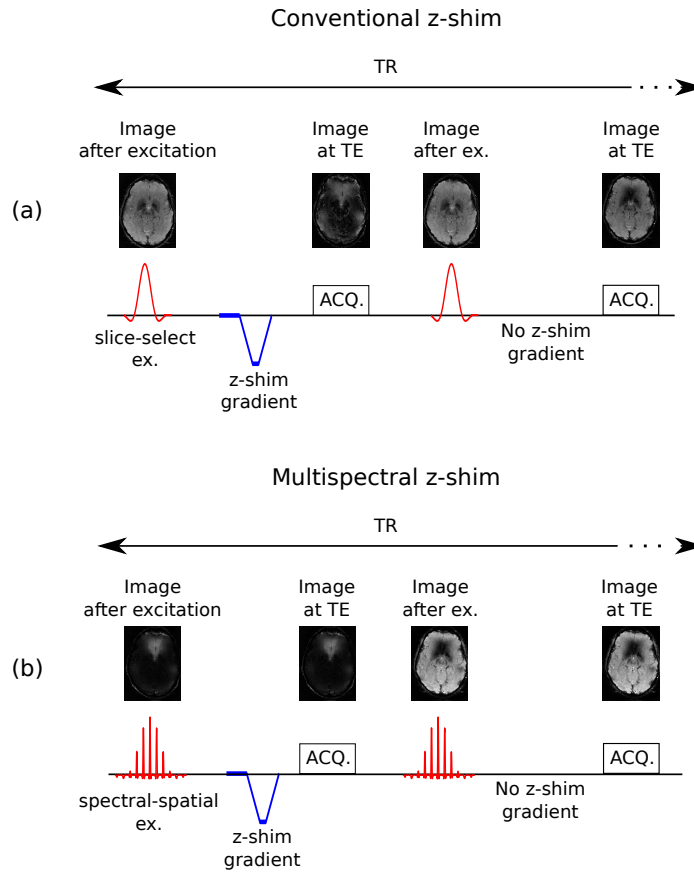
Figure III.1: Illustration of two-band conventional z-shim (a) and MS z-shim (b) pulse sequences where the different signal loss regions are treated as two slices in a multislice stack. In conventional z-shim, a slice-select pulse is played to excite the entire slice followed by a precompensatory gradient to rewind the spin isochromats in regions of susceptibility difference. Typically, multiple images are acquired with different z-shim gradient moments. Since the entire slice is excited in each repetition, regions with no signal loss experience a decrease in longitudinal magnetization which leads to loss of signal. In MS z-shim, spectral-spatial pulses are used to selectively excite different regions of susceptibility-difference. Since the spins in regions with no loss are not excited, they do not lose longitudinal magnetization, thus preserving the signal.

precompensatory z-shim gradient tailored to that band. Since the N_b bands correspond to disjoint groups of voxels in the image slice, the MS approach allows all bands to be imaged in a single TR, without a SNR penalty. The composite image is formed in reconstruction by performing a sum-of-squares combination of all the band images. In comparison, since conventional z-shim uses excitation pulses that excite all the spins in a slice each time a band is imaged, collecting all images in a single TR period will result in SNR loss due to

incomplete relaxation of the longitudinal magnetization in the spins outside the rephased regions.

III.3 Methods

III.3.1 Pulse design

In the MS z-shim method, spectral-spatial pulse parameters and z-shim gradient moments were computed based on multi-slice off-resonance ($\triangle f$) maps measured over the desired slice thickness using the double echo-time method [55]. From the $\triangle f$ maps, masks covering the different frequency bands were manually defined. For example, a slice exhibiting off-resonance in the frontal cortex had two masks for the frontal region and the rest of the slice, respectively. The $\triangle f$ map histograms with 64 frequency bins were calculated for each band mask. The center frequency (f_0) of each band was set to the frequency bin containing the maximum number of pixels. The histogram based approach helped to avoid any noisy pixel with unusually high or low $\triangle f$ value. For each band, a spectral-spatial pulse was designed using the iterative method described in Ref. [56] to excite a slice with the desired thickness and slice location. The center frequency of the pulse was set to that computed from the $\triangle f$ histogram. For the width of the spectral-spatial pulse's passband a value between 160 and 200 Hz was manually chosen. This range of bandwidth sufficiently covered the frequency bands and provided adequate overlap between the bands to avoid signal attenuation in the transition region between the bands for brain imaging experiments at 3 T. The spectral FOV of the pulses was 440 Hz. To compute the precompensatory z-shim gradient the knowledge of α proportionality constant is required. For typical susceptibility differences in the human head at 3 T, α values between 1-2 mT/m/Hz (Eq. III.2) have been previously reported [28, 53]. The value of α can be negative in some brain regions. Here, the spectral spatial pulses were simulated over the multi-slice $\triangle f$ maps to obtain the magnetization patterns for each band over all the sub-slices. Z-shim gradient moments were calculated over a range of α values from -2 to 2 mT/m/Hz in increments

of 0.13 mT/m/Hz for the band's center frequency f_0. For each α, the final magnetization pattern was computed as the complex sum of the simulated patterns over all the sub-slices. For each band, the z-shim gradient waveform was computed from the α value that gave the maximum sum of the absolute signal in the final magnetization pattern inside the band mask. Code to design the pulses is available at https://bitbucket.org/wgrissom/z-shimming.

III.3.2   Experiments

In vivo brain imaging experiments were performed in 15 subjects (age = 27.5 +/-4.5 years; sex = 8 male, 7 female) on a 3 T Philips Achieva scanner (Philips Healthcare, Best, Netherlands) with a body transmit coil and a 32-channel head receive coil, with the approval of the Institutional Review Board at Vanderbilt University. The images were acquired using a modified gradient recalled echo pulse sequence. $\triangle f$ maps were measured using the double echo time method [55] in 20 slices with 0.5 mm slice-thickness covering a z-FOV of 1 cm. Flyback spectral-spatial pulses were designed to excite a 5 mm thick slice. The pulses were designed with spatial time-bandwidth product 4 and spectral time-bandwidth product 3. The flip angle was set to 80 degrees which corresponds to the Ernst angle for the human head cortex with $T_1 = 1200$ ms for a TR of 2000 ms. The center-frequency and passband width of the pulse was calculated using the method described in the previous section. The gradient waveforms were designed subject to a maximum strength of 3 G/cm and maximum slew rate of 12 G/cm/ms. Both the gradient and RF waveforms were defined with the scanner's dwell time of 6.4 μs . These settings produced pulses between 17 and 23 ms long.

III.3.2.1   Structural Experiments

Gradient recalled echo (GRE) images with TR/TE of 2000/35 ms, and slice thickness 5 mm were acquired over FOV of 260×260 mm and matrix size 96×96 in the 15 subjects using coventional GRE with no compensation, conventional z-shim and MS z-shim methods. The performance of the three methods was compared by computing image ratio maps between

the methods. Z-shim/GRE, MS z-shim/GRE and MS z-shim/z-shim image ratios were computed. The hypotheses was that compared to conventional GRE, MS z-shim would give higher signal in more voxels than conventional z-shim. To test this hypothesis paired t-tests were performed to compare the percentage of voxels in the slice that have a ratio greater than 1 in MS z-shim/GRE versus z-shim/GRE maps. In one of the subjects an additional lower slice was imaged to illustrate that, when dictated by a larger range of through-plane gradients, three or more distinct frequency bands and z-shim gradient moments can be used for more complete signal recovery. The three bands were imaged within the same TR of 2000 ms. To verify that multispectral z-shim can recover signal at multiple slice locations in the brain, the method was used to acquire 5 axial slices near the frontal sinus and the middle ear canal of one of the subjects. The upper four slices were 3 mm apart and the lowermost slice was chosen to be 12 mm away to demonstrate signal recovery in the temporal lobe near the middle ear canal. The TR for these multislice structural scans was 250 ms.

III.3.2.2 Functional Experiments

To compare the performance of MS z-shim with GRE and conventional z-shim methods in functional imaging, block design breath-hold BOLD fMRI experiments were performed in the 15 subjects. Since breath-holding leads to a global increase in cerebral blood flow and volume in healthy parenchyma, it is a suitable fMRI task to compare the performance of the methods in the different brain regions. Each 1 minute block comprised 40 s of normal breathing, 3 s of breathing in, 2 s of breathing out, followed by a 15 s breathhold. In each fMRI run, the task block was repeated 5 times and single-shot echo-planar images with a $2\times$ SENSE acceleration factor were acquired with spatial resolution of $3.5 \times 3.5 \times 5$ mm and TR/TE of 2000/35 ms. The same TR/TE settings were used in the GRE, conventional z-shim and MS z-shim experiments. STIR [57] fat-suppresion was used to suppress fat chemical-shift artifacts in the images. The fMRI activation maps were computed using

the FSL FEAT package [58, 59, 60] (FMRIB, Oxford, UK). Voxel-wise z-statistics were calculated using the general linear model where the box-car regressor was convolved with a double gamma canonical hemodynamic response function. FILM pre-whitening [61] was enabled and the images were smoothed with a Gaussian kernel with full-width at half-max of 5 mm and high pass filtered to remove undesired low frequency content such as scanner drift. The computed z-stat maps were thresholded at a z-stat value of 1.8 and cluster p threshold of 0.05.

The temporal SNR (tSNR) of the MS z-shim method was compared to coventional GRE and z-shim acquisitions, with matched TRs. tSNR maps were computed by dividing the mean signal in each voxel over time by the signal standard deviation over time. It has been earlier shown that tSNR is a good indicator of BOLD sensitivity [62, 63]. For statistical validation, single-tailed paired t-tests were performed between MS z-shim and GRE tSNR maps and between MS z-shim and z-shim tSNR maps in the regions of signal loss (frontal and temporal lobes) and the entire slice respectively to test the unidirectional hypothesis that MS z-shim provides higher tSNR compared to conventional GRE and z-shim methods. For each method, the region of signal loss was defined by the voxels with image intensity value less than 15% of the maximum signal in that slice.

The fMRI z-stat maps were used to compare the activation coverage of the conventional GRE, z-shim and MS z-shim methods. Activation coverage in a region was defined as the percentage of voxels in the region that were activated (z-stat > 1.8). The activation coverage in the signal loss region (frontal and temporal lobes) and the rest of the slice respectively were compared.

The signal loss region was defined in the same way as for the tSNR maps. Paired t-tests were performed to compare the activation coverage of GRE versus conventional z-shim, and MS z-shim versus conventional z-shim, respectively.

III.4 Results

III.4.1 Structural Experiments
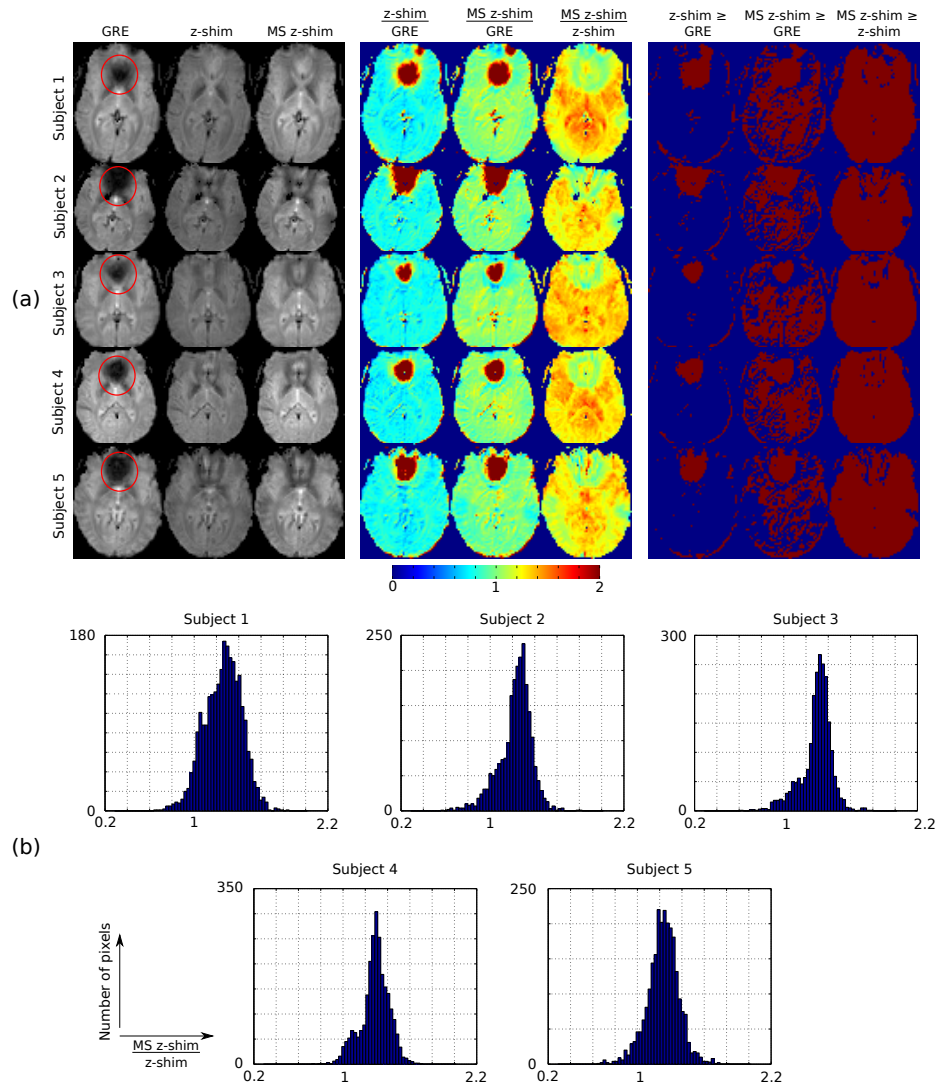
Figure III.2: Representative gradient echo images and image ratios from 5 subjects. Red circles on the GRE images show signal loss in the frontal lobe. The image ratio maps show that both conventional z-shim and MS z-shim recover signal in the frontal lobe. But, conventional z-shim loses signal in the rest of the slice. The histogram of the MS z-shim/z-shim maps shows that most of the voxels has a value greater than 1, indicating that MS z-shim gave higher signal than z-shim in majority of the voxels.

Figure III.2 shows representative images and image ratios from 5 subjects. Red circles on the GRE images show the regions of signal loss in the frontal cortex. In all the subjects, both conventional z-shim and MS z-shim methods brought back signal in the frontal region.

62

Z-shim/GRE maps demonstrate that compared to GRE, z-shim recovers signal in the frontal lobe but loses signal in the rest of the slice. MS z-shim/GRE maps show that MS z-shim recovers signal in the frontal region and maintains signal in the rest of the slice. MS z-shim/z-shim maps show that MS z-shim and z-shim recover signal to similar levels in the frontal lobe, but in the rest of the slice MS z-shim gives higher signal levels. In the frontal region of the MS z-shim/z-shim maps, MS z-shim produces higher signal than z-shim in the center, where the off-resonance was well within the spectral-spatial pulse's passband and the z-shim gradient caused more complete recovery. MS and conventional z-shim signal levels were more similar in the regions of overlap between the spectral bands. The histograms of the MS z-shim/z-shim maps further illustrate that majority of the voxels in the maps have values greater than 1 indicating that MS z-shim gives higher signal than conventional z-shim in most of the slice. Averaged across all the 15 subjects, MS z-shim gave higher signal than GRE in 37% more voxels than conventional z-shim with a standard deviation of 12% and p-value < 0.001. The conventional z-shim signal may have been boosted slightly by using the Ernst angle for a 1000 ms TR; the Ernst angle for gray matter ($T_1 = 1200$ ms) and white matter ($T_1 = 800$ ms) are 64 degrees and 74 degrees, respectively, for TR = 1000 ms. In simulation it was seen that the use of these flip angles would have led to a signal boost of 4% and 0.7% in the gray and white matter, respectively, for conventional z-shim. However, even with this signal boost, MS z-shim would have produced 18% higher signal.

Figure III.3 shows the conventional z-shim and MS z-shim images and MS z-shim/z-shim image ratio maps for a slice acquired using two and three frequency bands, respectively. The green contour on the MS z-shim $\geq$ z-shim map shows inadequate signal recovery in the transition region between the two bands. With the addition of a third band, signal was recovered in the transition region and MS z-shim signal was higher than conventional z-shim in 91% of the voxels compared to 83% when two bands were used.

Figure III.4 shows the conventional GRE, z-shim and MS z-shim images acquired in
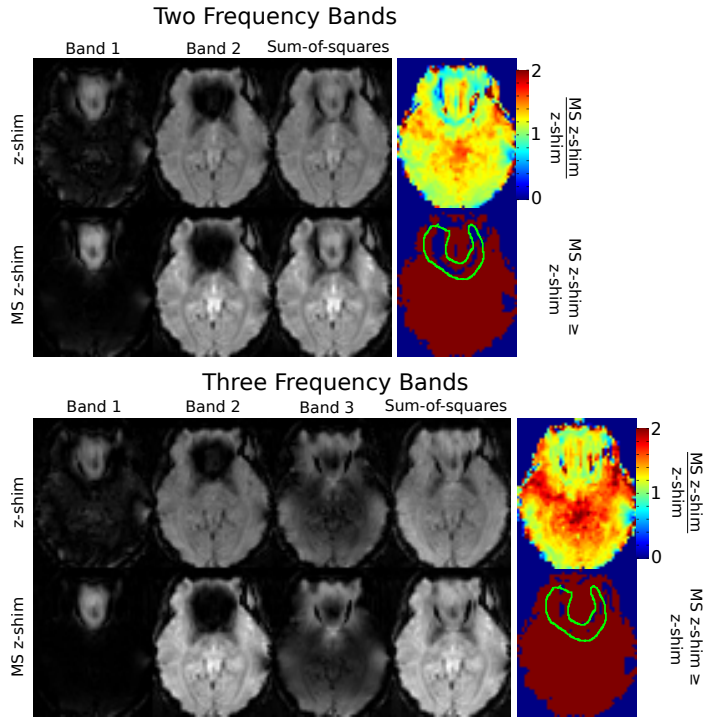
Figure III.3: Comparison of gradient echo images acquired using MS z-shim with 2 and 3 frequency bands, respectively. The green contour line in the MS z-shim $\geq$ z-shim map shows that when 2 frequency bands are used, signal cannot be fully recovered at the transition region between the bands. With the addition of a third band, signal is recovered in most of the voxels in the transition region.

five slices in one of the subjects. Red circles show the region of signal loss in the frontal lobe of the top 4 slices, and in the temporal lobe of the last slice.

Images in each row have the same grayscale window level and width. Both MS z-shim and conventional z-shim recovered signal in the frontal and temporal regions. But MS zshim gave higher signal than conventional z-shim.

III.4.2 Functional Experiments

Figure III.5 shows representative fMRI activation maps in one of the subjects from the conventional GRE, z-shim and MS z-shim scans. Qualitatively, conventional GRE shows signal loss in the frontal region which leads to loss of activation. Both conventional z-shim and MS z-shim recovered activation in the frontal lobe but z-shim loses activation in the rest of the slice which is maintained by MS z-shim. The bar plots show the MS
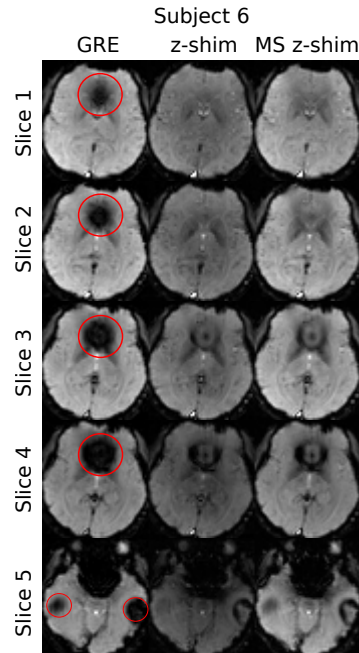
Figure III.4: Images acquired using conventional GRE, conventional z-shim and MS z-shim in 5 brain slices of one of the subjects. In all the slices both z-shim and MS z-shim recovered signal in the regions of loss and MS z-shim gave higher signal. In slice 5, signal was recovered in the temporal lobe near the middle ear canal.

z-shim/GRE and MS z-shim/z-shim tSNR maps primarily in bi-frontal lobes and the entire slice averaged across the 15 subjects. P-values from the paired t-tests are also shown. At a significance level of 5%, the p-values indicate that MS z-shim gives significantly higher tSNR than GRE in the frontal lobe and the entire slice. At a p-value < 0.02, MS z-shim had higher t-SNR than conventional z-shim in the entire slice. And at p-value < 0.7, it cannot be concluded that MS z-shim tSNR was higher than conventional z-shim in the frontal lobe. This was expected, from Fig. III.2 it can be seen that in the frontal lobe both conventional and MS z-shim methods recover signal to similar levels, therefore they were expected to produce similar tSNR values.

Table 1 shows the difference in activation coverage between conventional z-shim and GRE, and MS z-shim and GRE, respectively. The mean difference in activation coverage is also shown along with the p-value from the paired t-tests. At a significance level of 5% it can be concluded that conventional z-shim recovers activation in the signal loss regions

	Subject															Mean
	1	**2**	**3**	**4**	**5**	**6**	**7**	**8**	**9**	**10**	**11**	**12**	**13**	**14**	**15**	
(z-shim−GRE) in signal loss regions	69	10	45	41	33	11	31	15	65	-21	20	-2	2	29	-26	**22 % ($p < 0.005$)**
(GRE−z-shim) in rest of the slice	8	5	-10	11	14	12	10	-12	-18	39	-3	-4	7	2	6	**5% ($p < 0.02$)**
(MS z-shim−GRE) in signal loss regions	5	42	31	3	-17	-8	58	-2	62	-34	-2	60	5	29	-2	**15% ($p < 0.04$)**
(GRE−MS z-shim) in rest of the slice	5	-5	-5	31	5	16	0	13	-18	5	-4	-19	-8	-12	28	**-1% ($p < 0.7$)**

Table III.1: Difference in BOLD fMRI activation coverage in the 15 subjects between z-shim and GRE and GRE and MS z-shim and GRE, respectively, in the signal loss regions and the rest of the slice, respectively. The mean difference in activation coverage across all the subjects and the p value from the paired t-tests are also shown. At $p < 0.005$, z-shim had higher coverage in signal loss regions than GRE. At $p < 0.02$, GRE coverage was higher than z-shim in the rest of the slice. At $p < 0.04$ MS z-shim had higher activation coverage than GRE in the signal loss regions. Whereas, in the rest of the slice, at $p < 0.7$ it cannot be concluded that GRE signal was higher than MS z-shim in the rest of the slice. It was expected that GRE and MS z-shim will have similar activation coverage in regions of no loss.
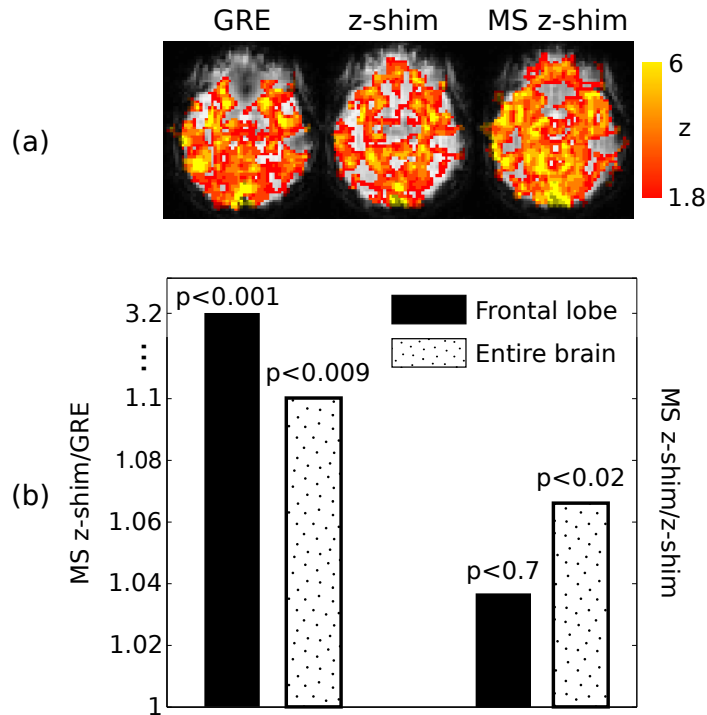
Figure III.5: Representative BOLD fMRI activation maps from one of the subjects measured using conventional GRE, conventional z-shim and MS z-shim methods. Both z-shim and MS z-shim recovered activation in the frontal lobe but z-shim lost activation in the rest of the slice while MS z-shim preserved activation. The bar plot shows the mean MS z-shim/GRE and MS z-shim/z-shim tSNR ratios in the signal loss region and the entire slice averaged across all the 15 subjects. At $p < 0.001$ and $p < 0.009$ MS z-shim gave higher tSNR in signal loss regions and the entire slice, respectively. With $p < 0.02$, MS z-shim tSNR was higher than z-shim when considering the entire slice. In the signal loss regions, even though MS z-shim gave 4% higher tSNR than z-shim, at $p < 0.7$ it is not statistically significant.

compared to GRE but loses activation in the rest of the slice. MS z-shim recovers activation in the signal loss regions compared to GRE. In the rest of the slice, it cannot be concluded that activation from MS z-shim is different from that from GRE. This was expected since MS z-shim has been shown to maintain the same signal level as GRE in regions of no signal loss.

III.5 Discussion

Structural imaging experiments demonstrated that in multiple subjects and in multiple slices in one of the subjects, compared to conventional GRE, the MS z-shim method re-

covers signal in the regions of loss while maintaining signal elsewhere in the slice. In comparison, the conventional z-shim loses signal in the regions with no signal loss. The fMRI experiments showed that the MS z-shim method recovers activation in the signal loss regions while maintaining activation in the rest of the slice. The conventional z-shim method led to loss of activation in regions without signal loss. The average pulse design time in our experiments, including manual segmentation of the bands, was about 1 minute and reconstruction of the composite image using sum-of-squares operation is straightforward with compute time in milliseconds. And given that $\triangle f$ maps are usually available from the prescan stage of main field shimming in high field imaging studies, MS z-shim method can be readily utilized in routine research protocols without noticeable time penalty.

III.5.1 Comparison to existing methods for mitigating through-plane signal loss in fMRI

The proposed MS z-shim method has several advantages over earlier approaches for signal loss mitigation. The major drawback of earlier methods such as conventional z-shim [23], and pulse design based methods for simultaneous multislice imaging [64, 53], is reduced fMRI sensitivity in regions with no signal loss. Using MS z-shim we have demonstrated that fMRI signal can be recovered in regions with susceptibility difference while maintaining signal elsewhere. Earlier z-shim schemes that use single-shot EPI [24] and spiral readout [25] suffer from long readout times and different T_2^* weighting for the different signal loss regions. Moreover, these methods are limited to the use of two z-shim values as additional z-shimmed regions will have significant T_2^* decay. MS z-shim does not suffer from these drawbacks as each frequency band is acquired in a separate readout window. And since each band is treated as a separate slice in a multislice imaging stack, multiple bands can be corrected without significant increase in scan time.

III.5.2 Limitations and Future Directions

The proposed setup of the MS z-shim method involves some manual steps which could be automated to reduce the sequence design time. For example, the masks for the different bands may be determined using an optimized image thresholding method. Presently, all the band pulses have the same passband width which is manually set. In our pulse sequence implementation, we were constrained to use the same gradient duration across all the bands. But it is possible that each frequency band has an optimal width which can be determined using the acquired $\triangle f$ maps.

We have presented results from 2D single-slice experiments but the proposed MS z-shim method can be extended to simultaneous multislice imaging [3, 65]. This could be implemented in a gradient moment-driven manner, by jointly determining a set of gradient moments across the simultaneously-excited slices and summing the corresponding spectral-spatial pulses [64]. Because α may vary somewhat between slices, the spectral-spatial pulses may excite different frequency bands in each slice for the same gradient moment. The new multislice multispectral imaging paradigm will allow correction of signal loss artifacts in multiple slices with a higher signal level than what would be possible with a conventional simultaneous multislice z-shim sequence with the same TR.

III.6 Conclusions

A straightforward method to recover lost signal in brain regions with susceptibility difference-induced through-plane gradients was proposed. Compared to conventional GRE, the proposed MS z-shim recovered structural and functional signal in regions with loss and also maintains signal in the rest of the slice. In comparison, for the same TR the conventional z-shim method loses signal in regions with minimal through-plane gradients where the conventional GRE acquisition does not suffer signal loss. The MS z-shim method will be useful in long echo time T_2^* weighted imaging methods such as fMRI and susceptibility weighted imaging.

CHAPTER IV

Root-flipped multiband refocusing pulses

IV.1 Introduction

This chapter introduces a method to design low peak-power multiband refocusing pulses for spin echo SMS imaging.

Several methods have been proposed to design multiband pulses with reduced peak power compared to direct summation. One approach is to apply phase shifts to the pulses prior to the summation that can be optimized to achieve a minimal increase in peak RF amplitude over a single-slice pulse [31, 66]. The peak power of multiband pulses constructed this way has been shown to increase with the square root of the number of excited slices, rather than linearly. Another approach is to introduce time shifts between the single-slice pulse waveforms, so that their main lobes do not overlap in time [33]. That approach requires consideration of the different refocusing times of the different slices, but it was shown to achieve significantly lower peak RF amplitudes compared to phase-optimized pulses. Whereas the phase-optimized and time-shifted pulse design methods use the same constant trapezoid gradient waveforms that would be used by a single-slice pulse, the Power Independent of Number of Slices (PINS) pulse design technique constructs multiband pulses by breaking up a single-slice pulse into a train of hard pulses and placing uniform gradient blips between those pulses, whose area is dictated by the desired slice gap [30]. While PINS pulses are robust and simple to construct, in practice their durations can be unacceptably long and are primarily dictated by the gradient system slew rate. Furthermore, the number of excited slices cannot be controlled. To mitigate these drawbacks, a hybrid of PINS and conventional multiband pulses has been proposed, which have shorter pulse durations than PINS pulses and lower peak amplitudes than conventional multiband pulses [67].

Root-flipping is a method that has been extensively applied to other RF pulse design problems to minimize the peak amplitude of a pulse subject to a fixed pulse duration, or equivalently to reduce its duration subject to a fixed peak amplitude [68, 69, 70, 71, 72]. It has typically been applied when a high time-bandwidth product is used to obtain very sharp slice or slab profiles for inversion, saturation or refocusing. The procedure requires first the design of a selective RF pulse using the Shinnar-Le Roux (SLR) algorithm [15], followed by the replacement of selected passband roots of its α and/or β polynomials with the inverses of their complex conjugates. The best pattern of flipped roots will lead to a uniform distribution of RF energy in time, imitating a quadratic phase pulse. Root flipping changes the phase responses of the α and β polynomials but does not change their magnitude responses, so the magnitude of the excited magnetization remains unchanged compared to the original pulse. The best pattern of flipped roots can be determined by exhaustive search when the number of roots is small, or using optimization methods such as genetic or Monte-Carlo algorithms [72, 71] when it is large.

In this work we propose a multiband pulse design method based on root-flipping. Like phase-optimized and time-shifted pulses, the algorithm produces pulses to be played simultaneously with a constant gradient. However, we show that it achieves substantially lower peak RF amplitudes for a given duration, or equivalently, shorter pulse durations for a given peak RF amplitude. The method is based on an extension of the SLR algorithm to directly design multiband pulses based on multiband digital filter designs, and the duration of the pulses is minimized subject to a desired peak RF amplitude by redistributing RF energy in time using multiband root-flipping. Because the designed refocusing pulses will produce non-linear phase profiles across the refocused slices, phase-matched excitation pulses are also designed to obtain linear-phase echoes. Alternatively, the pulses can be used directly in twice-refocused spin echo sequences with conventional linear-phase multiband excitations, since the nonlinear refocusing phase will cancel out [73]. The pulse design method is explained in detail in the Theory section. That section is followed by a comparison of

the performance of the root-flipped multiband pulses to phase-optimized [31, 66] and time-shifted [33] pulses in simulations. Finally, phantom and in vivo human experiments were performed at 7 T to validate the root-flipped pulses' function and to compare their signal profiles to that of time-shifted pulses.

IV.2 Theory
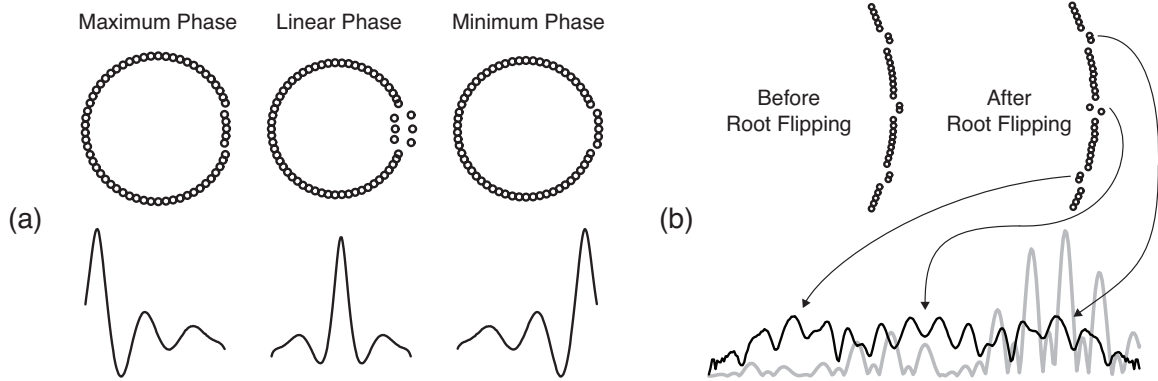
Figure IV.1: Illustration of how root flipping can reduce the peak RF amplitude of multi-band pulses. (a) The positions of the complex passband roots with respect to the unit circle determines the position of the main lobe within a single-band pulse. To minimize the peak amplitude of a multiband pulse, the passband roots of each band can be configured so that its main lobe does not coincide with the other bands' main lobes. (b) A 3-band pulse designed by the proposed algorithm. The algorithm first designs a minimum-phase multi-band pulse (left zoomed-in roots, gray RF amplitude waveform). The peak amplitude of that pulse is minimized using Monte Carlo optimization to determine the best configuration of flipped passband roots. In this 3-band case, the optimization converged on minimum-, linear- and maximum-phase root configurations for the bands, producing three humps in the pulse's amplitude waveform corresponding to the bands' main lobes.

The basic idea of the proposed method is illustrated in Fig. IV.1. Figure IV.1a shows how the timing of a pulse's main lobe depends on the position of its β filter's passband roots relative to the unit circle. This suggests that the passband roots of a multiband pulse can be configured so that the bands' main lobes do not coincide in time, and the peak amplitude of the pulse can be reduced compared to direct summation of identical pulses. Figure IV.1b il-lustrates the outputs of the two stages of the proposed method. In the first stage a multiband minimum-phase β filter is designed for the refocusing pulse. Minimum-phase filters are

chosen because they have sharper transition bands than the linear-phase filters on which most slice-selective refocusing pulses are based [15]. In the second stage an optimized root flipping pattern is determined using a Monte-Carlo algorithm to minimize the maximum magnitude of the resulting pulse. The best pattern of flipped roots will distribute the pulse's energy evenly over its duration. Once the root-flipped refocusing pulse is designed, a phase-matched excitation pulse can be designed to cancel non-linear phase variation in the refocusing profile, or the pulse can directly be used in place of both refocusing pulses in a twice-refocused pulse sequence.

IV.2.1   Multiband minimum-phase β polynomial design

In Ref. [15], Pauly et al provide an algorithm to design single-band minimum-phase RF pulses using SLR. Here we extend that approach to design multiband minimum-phase pulses using numerical optimization to obtain the required multiband β filter. We also incorporate smoothly decaying ripple constraints in the stopbands of the target β filter response to minimize spikes at the ends of the final waveforms [74], which appear in conventional minimum-phase SLR pulses derived from uniform ripple-constrained β filter designs.

To design a length-N multiband minimum-phase β filter, a length $2N - 1$ linear-phase filter is first designed whose magnitude response will equal the square of the minimum-phase filter's magnitude response. After its design it will be factored to produce the minimum-phase filter. Since the linear-phase filter will be symmetric, there are only N unique coefficients to design and only half the frequency axis needs to be considered in the optimization. The length-N half-filter $\boldsymbol{b}_{\frac{1}{2}}$ is designed by solving the following convex optimization problem:

$$
\begin{aligned}
\text{minimize} \quad & \delta \\
\text{subject to} \quad & -\delta \leq \{\boldsymbol{A}\boldsymbol{b}_{\frac{1}{2}}\}_i - 1 \leq \delta, \quad i \text{ in passbands} \\
& 0 \leq \{\boldsymbol{A}\boldsymbol{b}_{\frac{1}{2}}\}_i \leq \delta \frac{d_2^2}{2d_1} w_i, \quad i \text{ in stopbands.}
\end{aligned}
\tag{IV.1}
$$

In this problem, δ is the maximum passband ripple of the linear-phase filter, which will equal twice the minimum-phase filter's passband ripple d_1, and the maximum stopband ripple of the linear-phase filter is the square of the minimum-phase filter's stopband ripple d_2. The linear-phase filter's maximum stopband ripple should therefore equal $\delta \frac{d_2^2}{2d_1}$, which is the upper stopband constraint used in this filter design. The frequency grid is indexed by i, and the stopband ripple weights w_i decay as $1/i^2$ away from each stopband edge. They are generated for each stopband edge, are normalized to a maximum value of 1 at that edge, and are combined across edges by taking the maximum w_i across edges at each index i. Finally, the system matrix A has elements:

$$
a_{ij} = \begin{cases} 2\cos\left(2\pi i j/N_f\right), & i = 0,\ldots,N_f/2 \\ & j = 1,\ldots,N \\ 1, & i = 0,\ldots,N_f/2 \\ & j = 0. \end{cases} \tag{IV.2}
$$

The frequency grid in the design should be oversampled; an oversampling factor of 10 was used in the designs presented here so that $N_f = 10N$. Note that in this formulation the frequency response is strictly positive, so it need not be biased up prior to taking its square root to obtain the corresponding minimum-phase filter's response.

The set of indices i corresponding to passbands and stopbands in the β filter design are determined by the desired time-bandwidth product TB, the passband and stopband ripples δ_1 and δ_2, and the distance between the centers of the slices Δ, which has units of slice widths. The time-bandwidth product and ripples determine the fractional transition width W as [15]:

$$
W = (2TB)^{-1}d_\infty(2\delta_1, \delta_2^2/2). \tag{IV.3}
$$

where $d_\infty(\delta_1, \delta_2)$ is a polynomial defined in Ref. [15]. In the normalized frequency range $(0, N_f/2)$ spanned by i, the passband edges will then be $(1-W)TBN_f/(4N)$ away from the

center of each passband, and the stopband edges will be $(1 + W)TBN_f/(4N)$ away. The centers of the bands will be $TB\Delta N_f/(2N)$ apart from each other.

Once $\boldsymbol{b}_{\frac{1}{2}}$ is designed by solving the optimization problem in Eq. IV.1, the full linear-phase filter $\boldsymbol{b}$ is formed by concatenating $\boldsymbol{b}_{\frac{1}{2}}$ and its last $N - 1$ coefficients and mirror-flipping the former. The minimum-phase filter's magnitude response is then the square root of the magnitude response of $\boldsymbol{b}$, and its phase response is the Hilbert transform of its log-magnitude response [15]. Once this complex-valued response is formed, the final length-N minimum-phase filter is calculated as its inverse DFT.

IV.2.2 Minimization of Peak RF Magnitude by Monte-Carlo Root-Flipping Optimization

The peak amplitude of an RF pulse can be reduced by flipping its passband roots, since flipping the root of a filter changes its phase response but not its magnitude response, and redistributes the filter's energy in time [75]. In the present algorithm, once the minimum-phase multiband β filter is designed, a root-flipping pattern is found that minimizes the resulting multiband RF pulse's peak amplitude. As in the high-TB saturation and inversion pulse design problems to which root-flipping has previously been applied, exhaustive evaluation of the $2^{N_r/2}$ possible root-flipping patterns (where N_r is the total number of passband roots) is computationally infeasible for many multiband refocusing pulse design problems [72]. For this reason, a Monte-Carlo method is used to optimize the pattern because it enables an efficient search across patterns, and has been successfully used in very-high-TB root-flipped saturation pulse design [71]. The first step of the optimization procedure is to compute the filter's complex roots as the eigenvalues of its companion matrix. Then the roots are sorted by their phase angle, and $N_r/2$ roots in the top half of the complex plane and within a fixed distance of the center of each passband become eligible for flipping. That distance is typically set to be a few times greater than half the slice width to ensure that the entire passband is captured. Each eligible index is given a unique probability between 0 and

1, such that the probability of flipping the first root is $2/N_r$ and the probability of flipping the last root is 1. In each Monte Carlo trial, a length-$N_r/2$ vector of uniformly-distributed random numbers is generated, and a root is flipped if its corresponding random number is less than its probability by replacing it with the complex conjugate of its inverse. If a root is flipped, its conjugate root on the negative half of the complex plane is not flipped, and vice versa, to obtain a symmetric pulse. After the roots are flipped, they are multiplied back out to obtain the root-flipped β filter coefficients, and the inverse SLR transform is used to transform these coefficients and the corresponding minimum-phase α filter coefficients into the corresponding RF pulse. The RF pulse with the minimum peak magnitude across all Monte Carlo trials is saved as the output of the minimization.

IV.2.3 Matched Excitation Pulse Design

Root-flipped refocusing pulses will generally not produce linear-phase refocusing (β^2) profiles, so if the sequence is not twice-refocused then matched excitation pulses must be designed to cancel that non-linear phase and obtain full signal [76, 77, 78, 79]. After completing the above refocusing pulse design, a matched excitation pulse is designed to produce a β profile of:

$$\beta_{ex} = \frac{\beta_{ref}^2}{\sqrt{2}}, \tag{IV.4}$$

where the *ex* and *ref* subscripts denote excitation and refocusing. Due to the squared dependence on β_{ref}, the excitation pulse must reach twice the spatial frequency of the refocusing pulse, so β_{ex} must be evaluated on a length-$2N$ grid of frequency locations. This profile and the corresponding minimum-phase α profile are input to the inverse SLR transform to calculate the matched excitation pulse.

IV.2.4 Ripple Relationships

IV.2.4.1 Matched Excitation and Refocusing

To determine the relationship between δ_1, δ_2, and the magnetization ripples $\delta_{1,e}$ and $\delta_{2,e}$ after refocusing, we analyze the combined excitation and refocusing profile (assuming crushing), given by:

$$2\alpha_{ex}\beta_{ex}^*\beta_{ref}^2. \tag{IV.5}$$

To obtain a linear-phase magnetization profile after the refocusing pulse, the excitation pulse's β response is related to the refocusing pulse's β profile as:

$$\beta_{ex} = \beta_{ref}^2/\sqrt{2}. \tag{IV.6}$$

Substituting this and taking the magnitude, we obtain:

$$\sqrt{2}|\beta_{ref}|^4\sqrt{1-|\beta_{ref}|^2} \tag{IV.7}$$

Based on a truncated Taylor series expansion of this expression about $\beta_{ref} = 0$, the β stopband ripple δ_2 is related to the M_{xy} stopband ripple $\delta_{2,e}$ by:

$$\delta_2 = \left(\frac{\delta_{2,e}}{\sqrt{2}}\right)^{\frac{1}{4}}. \tag{IV.8}$$

The relationship between the β passband ripple δ_1 and the M_{xy} passband ripple $\delta_{1,e}$ is similarly derived from a truncated Taylor series expansion to be:

$$\delta_1 = \frac{\delta_{1,e}}{4}. \tag{IV.9}$$

IV.2.4.2 Twice-Refocused

Assuming crushing, the combined twice-refocused profile is $|\beta_{ref}|^4$. Following the same steps as the analysis of crushed spin echo pulses in [15], the β stopband ripple δ_2 can be

related to the M_{xy} stopband ripple $\delta_{2,e}$ as:

$$\delta_2 = \delta_{2,e}^{\frac{1}{4}}.$$

The relationship between the β passband ripple δ_1 and the M_{xy} passband ripple $\delta_{1,e}$ is approximated as:

$$\delta_1 = \frac{\delta_{1,e}}{8}.$$

IV.3 Methods

IV.3.1 Algorithm Implementation

All pulses were computed in MATLAB R2013a (Mathworks, Natick, MA, USA). Effective ripples of $\delta_{1,e} = \delta_{2,e} = 0.01$ were used in all designs. The time-bandwidth products of all root-flipped designs were scaled so that the pulses had the same transition widths as the linear-phase pulses, by determining the minimum-phase time-bandwidth product as

$$TB_{min-phase} = TB\frac{d_\infty(2d_1, d_2^2/2)}{2d_\infty(d_1, d_2)}. \tag{IV.10}$$

Applying this scaling ensured that the slice profiles were as similar as possible between pulses designed by the proposed method and previous methods that are based on conventional linear-phase refocusing pulses. All time-bandwidth products reported in this work refer to TB in the above equation. The minimum-phase multiband filter optimization problem (Eq. IV.1) was solved using CVX, a MATLAB-based software package for specifying and solving convex programs [80]. The A matrices used in those optimizations were built explicitly with an oversampling factor of 10. The function `fmp()` from the `rf_tools` software package (http://rsl.stanford.edu/research/software.html) was then used to compute the multiband minimum-phase β filter from the optimized linear-phase filter. Then MATLAB's `roots()` function was used to calculate the roots of the minimum-phase filter. The roots within 1.5 slice widths of the center of each band were deemed eligible for

flipping in the Monte Carlo optimizations, which used $80N_b\lceil TB \rceil$ trials, where N_b is the number of bands. In this paper, the maximum number of trials was 8,000 for a 10-band, *TB* 10 pulse. After root-flipping, a version of MATLAB's `leja()` function that was optimized for speed was used to order the roots to obtain numerically-accurate results when multiplying them out using the `poly()` function. All RF pulses were computed from their β filters using the `b2rf()` function from `rf_tools` package, which determines the corresponding minimum-phase α filter and invokes an inverse SLR transform. Code to design the pulses is available at http://www.vuiis.vanderbilt.edu/~grissowa/. For scientists without access to MATLAB, the algorithm could be ported to the free alternative Octave (http://octave.org) since the SDPT3 solver on which CVX is based is available on Octave (https://github.com/sqlp), the `roots()` and `poly()` functions have direct equivalents in Octave, the `rf_tools` software package is fully open-source, and our improved `leja()` function is included with our code.

IV.3.2 Simulations

Simulations were performed to compare phase-optimized [66] pulses, time-shifted and phase-optimized [33] pulses, and the proposed multiband refocusing pulses, as a function of the number of bands, time-bandwidth product, and slice separation. Phase-optimized pulses were designed by first designing a single-band SLR refocusing pulse, duplicating and modulating it, and optimizing the phase of each of the bands relative to the first band. The phase optimizations comprised 50 randomly-initialized calls to MATLAB's `fminsearch()` function to minimize the maximum amplitude of the summed pulse. The time-shifted and phase-optimized pulse designs started with the same single-band pulses, looped over a range of integer shifts per band (between 0 and N/N_b), and returned the phase-optimized and summed pulse with minimum normalized duration, measured as the product of the total number of samples in the pulse and its peak amplitude.

Pulses were designed with $N = 1024$ over a range of time-bandwidth products ($TB =$

4 to 10), number of excited bands ($N_b = 2$ to 10), and band separation ($\Delta = 2$ to 40 slice widths). The durations of the pulses were computed subject to a peak $|B_1|$ of 13 μT, based on a peak $|B_1|$ limit of 13.5 μT for the body coil of our Philips 3 T Achieva scanners (Philips Healthcare, Best, Netherlands). A minimum-duration matched excitation pulse with the same peak $|B_1|$ was designed for each root-flipped pulse.

IV.3.3 Experiments

Phantom and in vivo experiments were performed on a 7 T Philips Achieva scanner (Philips Healthcare, Cleveland, OH, USA) with a birdcage coil and a 32-channel receive-only head coil (Nova Medical Inc., Wilmington, MA, USA), and with the approval of the Institutional Review Board at Vanderbilt University. Root-flipped refocusing and phase-matched 90 degree excitation pulses were designed subject to a peak $|B_1|$ of 13 μT. The slice profiles were measured in 3D spin echo scans with the slice-select gradient waveforms played along the frequency-encode direction.

Phantom experiments were performed using a mineral oil bottle phantom to validate the slice profile of the proposed refocusing and excitation pulses. Root-flipped pulses with $TB = 4$ were designed to excite and refocus 3 and 6 slices of thickness 3 mm and slice gaps of 3 and 2 cm, respectively. The 3-slice spin echo images were acquired with TR/TE of 257/17.6 ms and the 6-slice images were acquired with TR/TE of 211/21.4 ms. The field-of-views (FOVs) were $20 \times 20 \times 26$ cm with $1600 \times 1600 \times 26$ matrix size. In another phantom experiment, the signal profile of a 3-band root-flipped pulse was compared to a 3-band aligned-echo time-shifted pulse with the same slice characteristics. The matched excitation pulse for the time-shifted refocusing pulse was designed using the same method as the root-flipped pulse. Both time-shifted and root-flipped pulses were designed with $TB = 4$ to excite 3 slices of thickness 3 mm with 3 cm slice separation. In the spin echo scans, the echo times were set to minimum allowed values, which was 28.3 ms for time-shifted and 17.6 ms for root-flipped pulses. The TR for both scans was 321 ms with FOV

80

of $20 \times 20 \times 26$ cm and $1600 \times 1600 \times 13$ matrix size.

In vivo experiments were performed on a human subject with $TB = 4$ root-flipped pulses that excited and refocused 3 slices with 3 cm slice gap and 3 mm slice thickness. Spin echo images were acquired with TR/TE of 237/17.6 ms and FOV $24 \times 24 \times 16$ cm with $480 \times 480 \times 16$ matrix size.

IV.4 Results

IV.4.1 Simulations
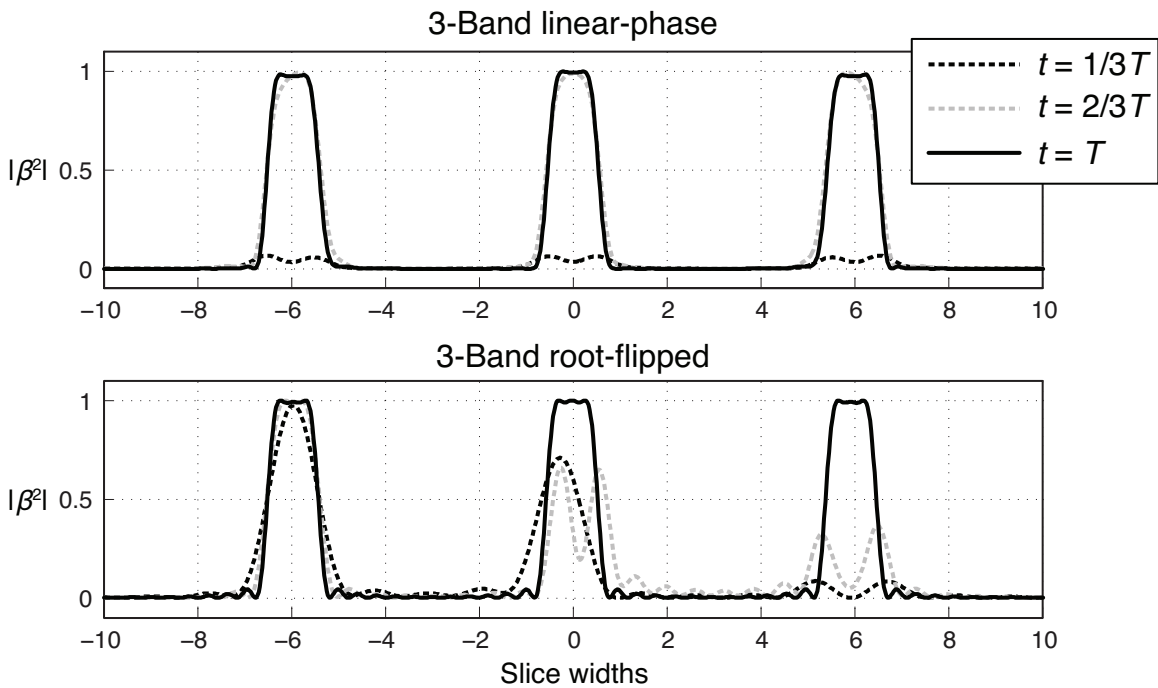
Figure IV.2: Comparison of the temporal evolution of three-band time-bandwidth product 4 root-flipped and linear-phase multiband refocusing. $|\beta^2|$ profiles are plotted one-third, two-thirds, and all the way to the end of the pulse.

Figure IV.2 compares the temporal evolution of three-band time-bandwidth product 4 linear-phase and root-flipped multiband refocusing. Whereas the linear-phase multiband pulse refocuses all slices simultaneously, the root-flipped pulse starts refocusing the leftmost slice first, and then the remaining slices in succession. This is similar to a quadratic phase pulse that sweeps through exciting its passband.
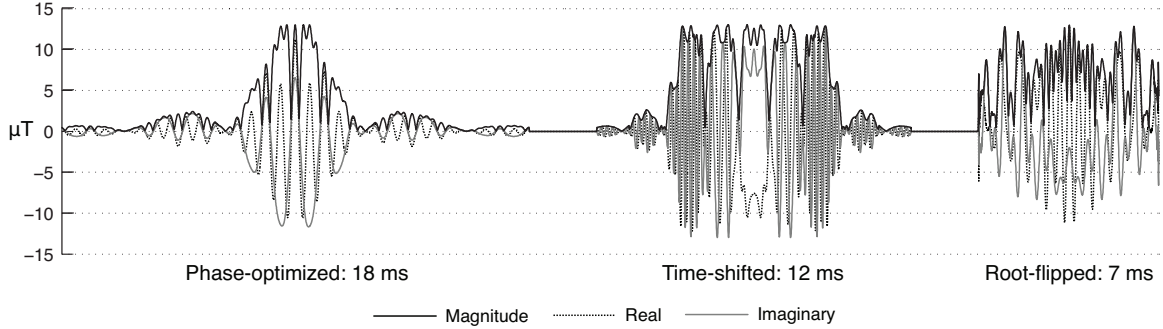
Figure IV.3: Comparison of five-band time-bandwidth product 4 pulse shapes designed by phase optimization, time-shifting, and root-flipping. Each pulse has been scaled to a peak magnitude of 13 μT.

Figure IV.3 compares pulse shapes obtained by the three design methods for $TB = 4$, $N_b = 5$, and a band separation of 4 slice widths. The phase-optimized pulse has the longest duration of 18 ms, with most of its energy concentrated in its center. The time-shifted and phase-optimized design spread out the main lobes, enabling a significantly shorter duration of 12 ms. However, that design has lower-amplitude sidelobes on its ends that are not present in the root-flipped pulse, which has the shortest duration of 7 ms.
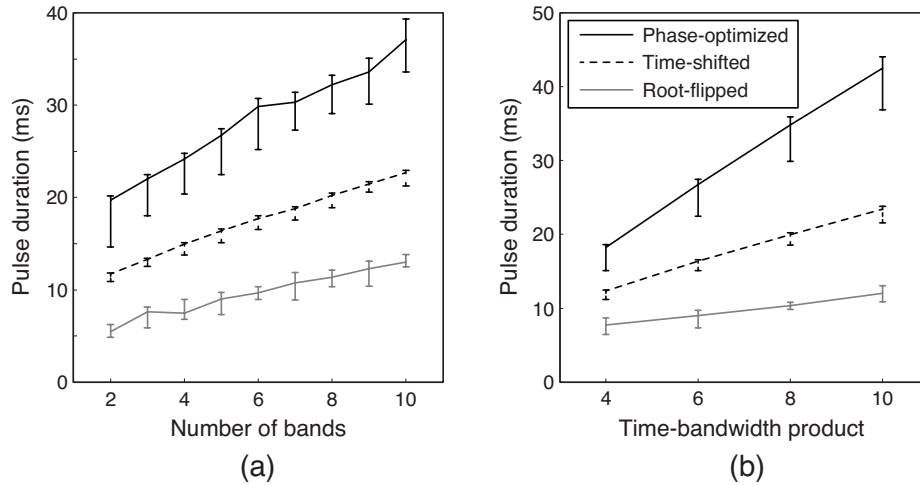
Figure IV.4: Durations of multiband pulses subject to 13 μT maximum $|B_1^+|$. (a) Duration versus number of excited bands, for a time-bandwidth product of 6. Error bars indicate maximum and minimum durations across band separations. (b) Duration versus time-bandwidth product for 5 bands.

Figure IV.4a plots the durations of $TB = 6$ pulses designed by the three methods as

a function of the number of bands, averaged across band separations (Δ). Error bars indicate the maximum and minimum duration across band separations, for each N_b. The phase-optimized and time-shifted and phase-optimized pulses all had durations over 10 ms. Figure IV.4b plots the durations of $N_b = 5$ pulses as a function of TB, again averaged across band separations. The root-flipped pulses had the shortest durations in all designs, and were on average of 46.2% shorter than the time-shifted pulses. The minimum-duration matched excitation pulses had on average 26.1% shorter durations than their corresponding root-flipped refocusing pulses.
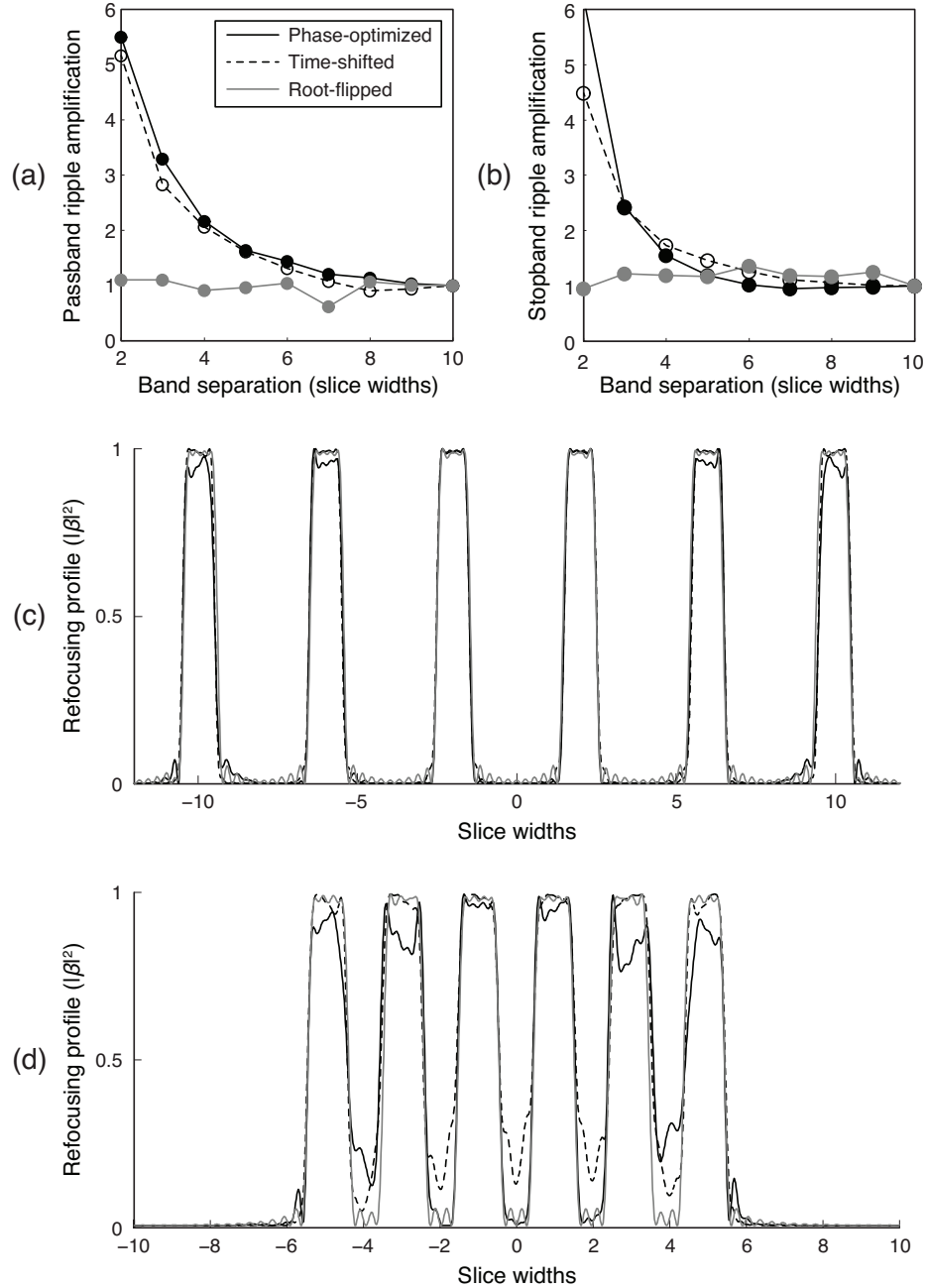
Figure IV.5: Excitation accuracy as a function of band separation for 6-band time-bandwidth product 6 pulses. (a) Amplification of maximum passband ripple as a function of band separation, relative to the maximum passband ripple for a 10-slice width band separation. (b) Amplification of maximum stopband ripple as a function of band separation, relative to the maximum stopband ripple for a 10-slice width band separation. (c) Refocusing $|\beta^2|$ profiles for a 4-slice width band separation. (d) Refocusing $|\beta^2|$ profiles for a 2-slice width band separation.

Figure IV.5 compares excitation accuracy as a function of band separation for the three

methods, for $N_b = 6$ and $TB = 6$. Figures IV.5(a,b) compare maximum passband and stop-band ripple amplification as a function of band separation, normalized to a separation of 10 slice widths. Due to Bloch equation nonlinearity and interference between stopband ripples and passbands, both the phase-optimized and time-shifted pulses' profiles degraded significantly as the bands were brought closer together. In comparison, the root-flipped pulses' maximum errors were stable across band separations. Figures IV.5c and IV.5d compare refocusing profiles for band separations of 4 and 2 slice widths, respectively, illustrating the degree of profile degradation in the phase-optimized and time-shifted designs as the bands are brought closer together. A band separation of 4 is within the range commonly used in SMS imaging.
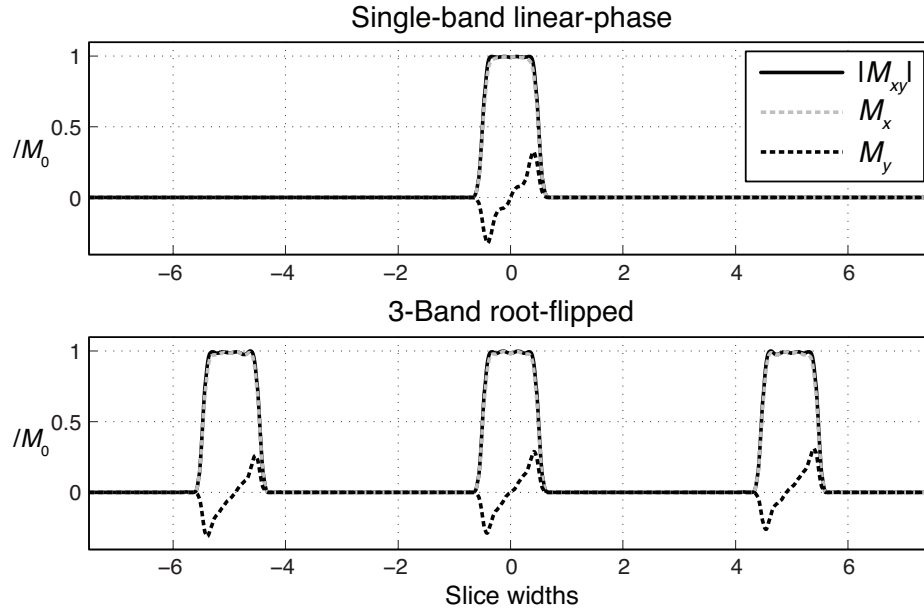
Figure IV.6: Comparison of complex M_{xy} profiles between a single-band linear-phase excitation and refocusing pulse pair, and a 3-band root-flipped excitation and refocusing pulse pair.

Figure IV.6 plots the complex M_{xy} profile of a conventional single-band $TB = 6$ linear-phase excitation and refocusing pulse pair, and a 3-band root-flipped excitation and refocusing pulse pair designed by the proposed method. Most of the magnetization lies along M_x in both profiles, and the M_y components have similar amplitude and shape. The M_x and

M_y profiles are also nearly the same for the 3 bands produced by the root-flipped pair. This validates that the spin echo slice profiles produced by the root-flipped pulse pairs do not contain additional nonlinear phase variations that could lead to through-slice signal loss, compared to conventional slice-selective excitation and refocusing pulses. In both single-band linear-phase and 3-band root-flipped profiles, the imaginary component arises from the nonlinear phase roll of the excitation pulses' α profiles.
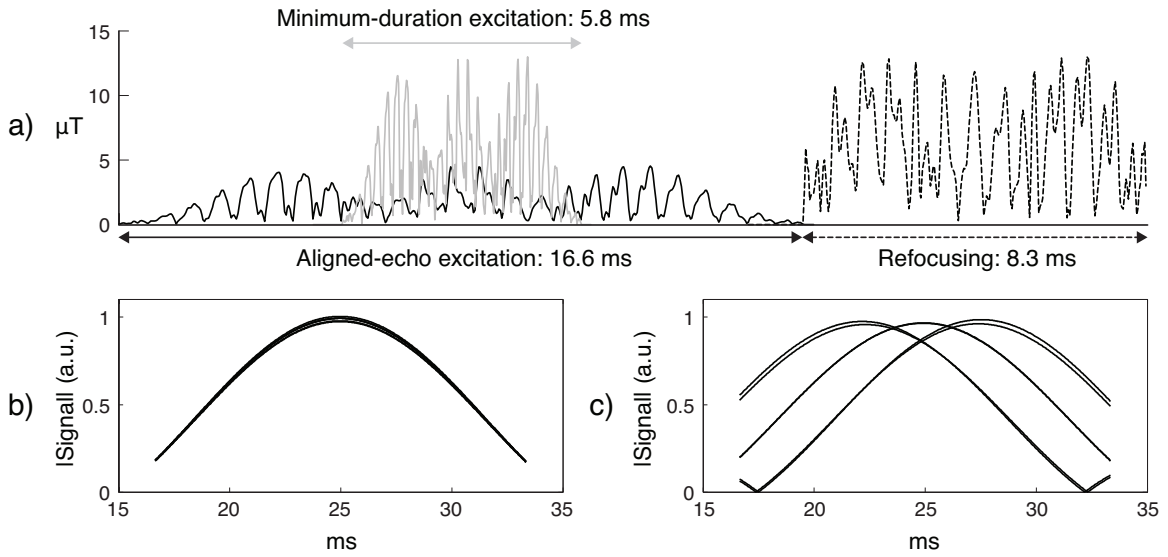
Figure IV.7: Comparison of aligned-echo and minimum-duration excitation pulses. (a) Magnitude plot of matched excitation and root-flipped refocusing RF pulse sequences, illustrating the relative durations of the refocusing pulse and the two excitation pulses (designed for 6-bands, time-bandwidth product 4, 5 slice-width band separation). (b) Spin echo signal profiles for each of the 6 bands when an aligned-echo excitation pulse is used. The spin echoes occur at the same time. (c) Spin echo signal profiles for each of the 6 bands when a minimum-duration excitation pulse is used, which reflect that the spin echoes are dispersed in a symmetric pattern around the aligned-echo point.

Figure IV.7 compares spin echo signals obtained using an excitation and refocusing pulse pair ($N_b = 6$, $TB = 4$, $\Delta = 5$ slice widths) with the excitation pulse duration either set to twice the refocusing pulse duration so that spin echoes form at the same time across bands ('aligned-echo'), or set for minimum duration subject to a 13 μT peak RF magnitude constraint. The two pulse sequences were Bloch-simulated over a ± 50 Hz range of off-resonance frequencies, up to and past the approximately 25 ms minimum TE of the

aligned-echo pulse pair. The aligned-echo signals refocused at the same time, as expected (Fig. IV.7b). The minimum-duration excitation pulse's duration was almost three times shorter than the aligned-echo pulse duration. This led to a dispersion of the spin echo signals in time (Fig. IV.7c) that may need to be accounted for in the design of the signal readout; echoes resulting from minimum-duration time-shifted excitation and refocusing pulses have this same characteristic. The echoes are distributed symmetrically about the aligned-echo point due to forced symmetry of the roots across the real axis of the complex plane.

IV.4.2 Experiments
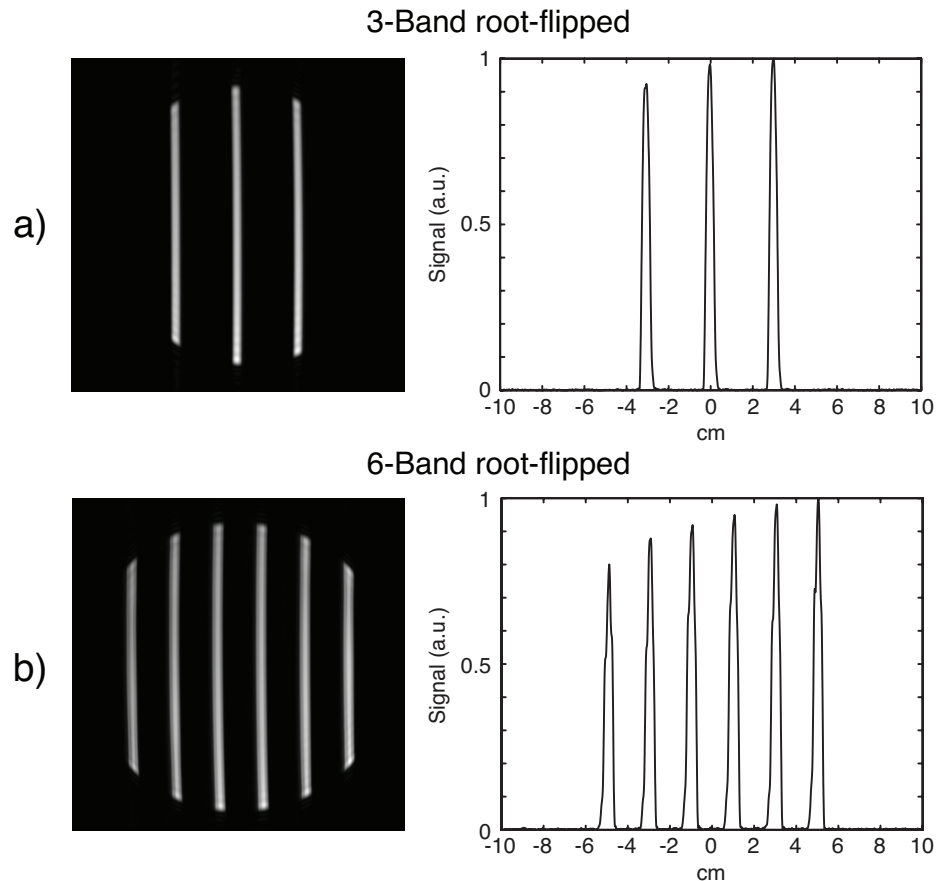
Figure IV.8: Time-bandwidth product 4 root-flipped pulse profiles measured in a mineral oil phantom at 7 T. (a) Slice profile of pulse designed to excite 3 slices of thickness 3 mm and slice gap of 3 cm. (b) Slice profile of pulse designed to excite 6 slices of thickness 3 mm and slice gap of 2 cm. The pulses excited the desired slices at the target locations.

Figure IV.8 shows the slice profiles of the 3-slice and 6-slice root-flipped pulses. Both the pulses excite the desired slices at the target locations and with the target slice widths. The slice profile plots show a left-right increase in signal amplitude across slices, due to TE differences between them. This behavior is consistent with simulations that showed that the left-most slices were excited first, followed by each of the remaining slices.
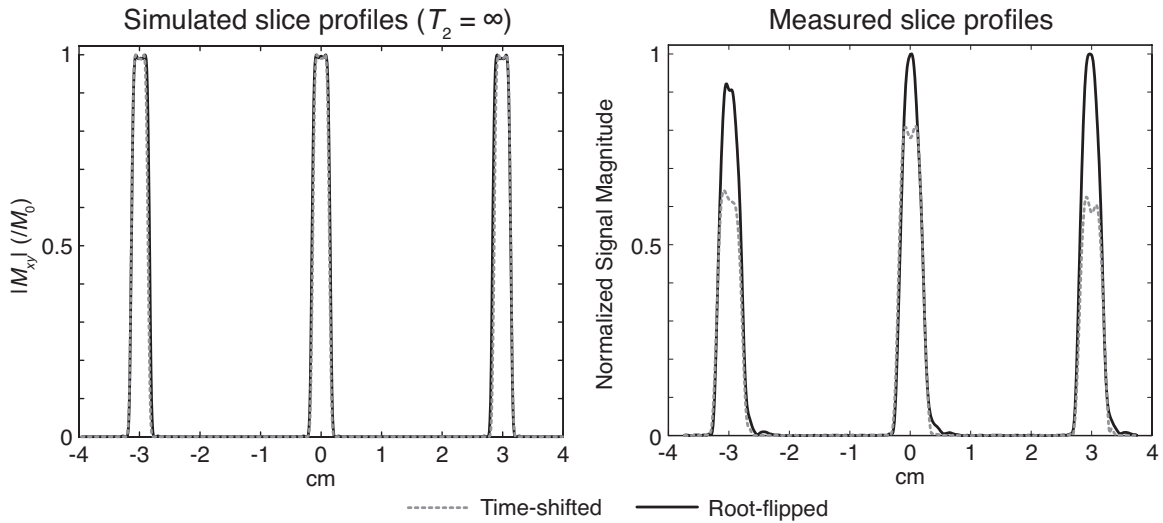
Figure IV.9: Comparison of slice profiles from time-bandwidth product 4 time-shifted and root-flipped pulses. (Left) Bloch simulations showed that without T_2 decay, both time-shifted and root-flipped pulses produce maximum signal at the desired slice locations. (Right) In the experiment, the shorter root-flipped pulse allowed a shorter TE of 17.6 ms compared to 28.3 ms for the time-shifted pulse, resulting in less T_2 weighting and higher signal.

Figure IV.9 compares simulated and measured signal profiles of time-bandwidth product 4 time-shifted and root-flipped refocusing pulses, which had durations of 9.76 and 5.76 ms, respectively. The shorter duration root-flipped pulse allowed a TE of 17.6 ms compared to TE of 28.3 ms for the time-shift pulse. Hence, for the same time-bandwidth product the root-flipped pulses produced higher signal due to lower T_2 weighting. The simulated profiles on the left show that without the T_2 decay, the pulses would produce the same signal levels and profiles.

The experimental root-flipped slice profiles in Figs. IV.8 and IV.9 are somewhat rounded

compared to the simulation, and the experimental time-shift slice profiles in Fig. IV.9 are also somewhat distorted in different ways. This is most likely the result of errors in RF pulse generation due to limited RF amplifier slew, which can be a problem for multiband pulses since their waveforms contain many rapid and large amplitude swings [81]. To address this, Zhu et al have described a multiband RF preemphasis method [82] that could be applied to the proposed root-flipped pulses or any other multiband pulse to improve excitation fidelity.

Target slice locations

Excited slice profiles

Individual slice images
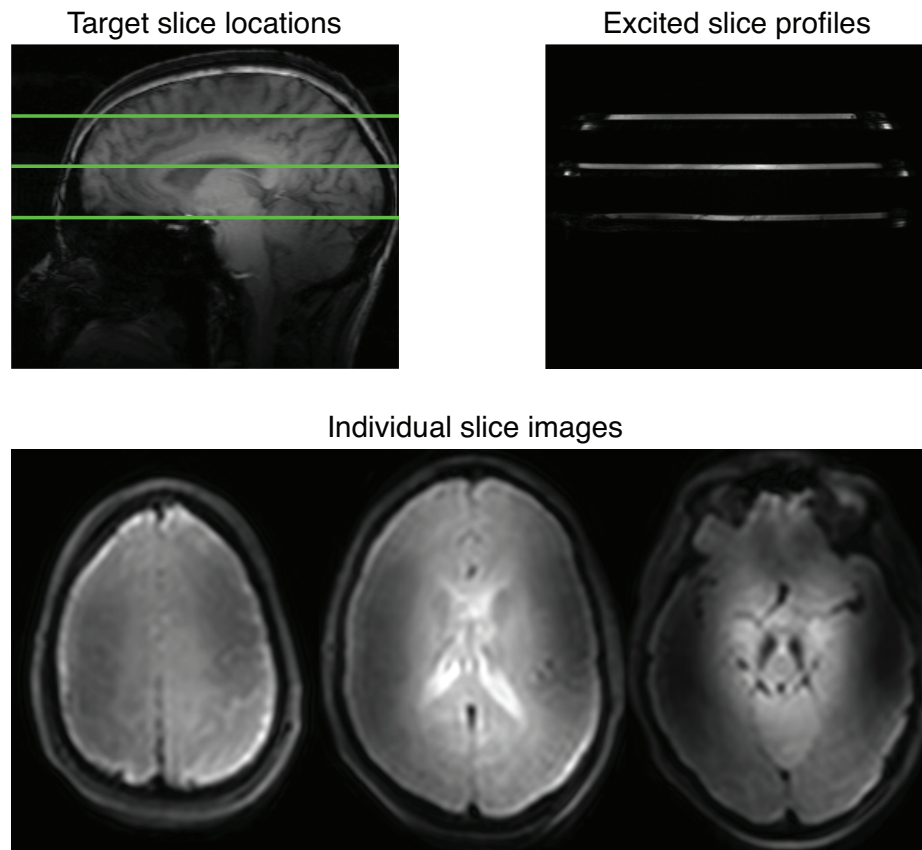
Figure IV.10: Time-bandwidth 4 root-flipped slice profile measured in the human head at 7 T. (Top Left) Green lines show the locations of the desired slices overlaid on a scout image. (Top Right) Imaged slice profiles appear at the intended locations. (Bottom) In-plane images of the three excited slices.

Figure IV.10 shows results from the in vivo experiment. The root-flipped pulse correctly excited the intended three slices with a 3 cm slice separation. Skull fat was uniformly excited outside the water slices. The figure also shows the transverse slice images acquired

using the root-flipped pulse, which contain amplitude modulations due to $|B_1^+|$ inhomo-geneity but otherwise appear as expected.

IV.5 Discussion

The simulation and experimental results showed that root-flipped multiband refocusing pulses have shorter durations than phase-optimized and time-shifted pulses, for the same peak RF amplitude. It was shown in a phantom experiment that the shorter duration of the root-flipped pulses resulted in higher spin echo signal than equivalent time-shifted pulses; by extension the root-flipped pulses should also result in higher signal than phase-optimized pulses since their durations are longer than time-shifted pulses, as shown previously by Auerbach et al [33].

   Like time-shifted pulses, multiband root-flipped refocusing and phase-matched excita-tion pulses can be used in 'aligned-echo' mode [33], where the same gradient magnitude is used for both excitation and refocusing pulses but the excitation pulse is approximately twice the duration of the refocusing pulse. In this mode, the slices' signals refocus at the same time, but they have different TEs. This was the mode used in the presented experiments. If the long duration of the excitation pulse or difference in slices' TEs are problematic, the excitation pulse can be shortened since its peak amplitude at full length is lower than that of the refocusing pulse, as was shown in the simulations. This will bring the slices' TEs closer together but their signals will refocus at different times, which may need to be taken into account in readout design as discussed by Auerbach et al for time-shifted pulses [33]. They suggested to tune the excitation pulse duration so that each spin echo occurs in the middle of an EPI readout lobe. Compared to time-shifted pulses, the shorter durations of root-flipped pulses will provide greater flexibility in echo timing, and neglecting the differences in slice refocusing times will result in less disparity between their signal levels. When shortening the excitation pulse of a root-flipped pulse pair, the refo-cusing time of each slice could be determined by Bloch simulation, as was demonstrated

in Fig. IV.7. More explicit control over the distribution of refocusing and excitation times for each slice could be obtained by flipping roots for bands in pre-specified maximum-, linear-, minimum-phase and other known patterns. This is not an issue for twice-refocused diffusion sequences that use the same root-flipped pulse for both refocusing pulses, since applying the same refocusing pulse twice results in a zero-phase refocusing profile [83]. In that case, a conventional linear-phase multiband pulse can be used for excitation.

Zhu et al [84] have also described a multiband refocusing pulse design algorithm that uses root-flipping. The primary difference between that method and the proposed method is that instead of root-flipping the full multiband profile, in Zhu's method a single-band minimum-phase refocusing pulse is designed and root-flipped. That pulse is then replicated and modulated to the target band locations, and inter-band phase optimization is applied prior to summing the pulses across bands. Like the proposed method, matched excitation pulses are required to obtain linear-phase spin echoes. Compared to the proposed method and time-shifted pulses, Zhu's pulses have the advantage that all echoes will appear at the same time with the same TE. However, because the component single-band pulses are identical, the pulse durations can be expected to lie somewhere between time-shifted and phase-optimized pulses for a given peak amplitude.

In the proposed algorithm the excitation pulse's slice profile was set to a scaled version of the refocusing pulse's profile. If the ability to independently adjust excitation pulse parameters such as slice thickness is desired, it should be possible to gain those degrees of freedom while satisfying the phase-matched condition using a method such as [85] to design the excitation pulse.

The current implementation of the algorithm was not optimized for computation time. The design time for a typical root-flipped pulse was 20-30 minutes which is not compatible with online use. There are several ways the pulse computation time could be reduced. Instead of using the CVX [80] package which is optimized for smaller problem sizes and rapid prototyping, a custom constrained optimization problem solver could be implemented

using approaches such as the log-barrier and primal-dual methods [86]. The initial linear-phase multiband β filter could also be generated using the method of Cunningham et al [87], though the proposed method gives better control over ripple levels. The Monte Carlo root-flip trials could also be run in parallel, and when the number of bands and the time-bandwidth product is small an exhaustive search may require fewer trials than the number used here. Furthermore, it may be possible to achieve nearly the same performance as the proposed algorithm using an approach in which multiple single-slice β polynomials are jointly root-flipped to minimize the peak amplitude of the resulting summed RF pulses. The individual root-flipped pulses could then be stored in a library and modulated and summed online, as the user adjusts parameters such as slice thickness and separation. Finally, as the proposed algorithm aims to produce pulses that imitate the behavior of quadratic phase excitations in which slices are excited sequentially, it should be possible to achieve the same performance by directly designing multiband quadratic phase pulses, using an extension of a quadratic phase pulse design algorithm to the multiband case [88, 89]. If the appropriate quadratic phase profile can be selected quickly without iteration, such an approach should be considerably faster than the proposed algorithm since root flipping would not be required. Computational acceleration using these approaches will be the focus of future investigations.

IV.6   Conclusions

A method was described to design multiband refocusing and matched excitation pulses. Simulations and experiments demonstrated that the pulses produce the desired slice profiles, and have shorter durations than existing multiband refocusing pulses with the same peak RF amplitude. The proposed pulses will be useful in simultaneous multislice acquisitions such as diffusion tensor imaging and spin echo functional MRI, where multiple slices need to be acquired at a high temporal resolution and short refocusing pulse durations are needed.

CHAPTER V

Contributions and future work

In this research work, we have proposed methods to mitigate the engineering challenges faced in high field simultaneous multislice MRI. In Chapter II we presented a method to design low peak power multiband spokes pulses capable of mitigating the transmit field inhomogeneity in simultaneously excited slices. In Chapter III we presented a straightforward pulse sequence to mitigate through plane signal loss in high field fMRI. In Chapter IV we presented a multiband RF pulse design method based on the SLR algorithm, that for a given peak RF power, produces pulses with significantly smaller duration compared to earlier methods. We conclude this dissertation by summarizing our contributions and proposing future work that can extend each of these research projects.

V.1 Transmit Field Inhomogeneity Compensation

We presented a method to design small flip-angle multiband spokes pulses that mitigate the center brightening artifact with low peak power RF pulses compared to pulses designed with no power regularization and with only integrated power regularization. Simulations performed using measured in vivo B_1^+ maps showed that the proposed 'slice-independent' design of multiband spokes pulses yielded more homogeneous excitation patterns and lower integrated and peak RF powers compared to pulses designed using the more straightforward 'slice-joint' approach. In vivo experiments with single transmit channel demonstrated that multiband spokes pulses provide lower center brightening compared to conventional multiband pulses. Similar reduction in center brightening was observed in multiband accelerated slice images that were separated in reconstruction.

There are many avenues for future work on transmit field inhomogeneity mitigation in simultaneous multislice imaging. The presented multiband spokes pulses were designed using the Fourier analysis which is valid for small flip angles. The Fourier relation al-

lows rapid computation of pulses using FFTs. However, at large flip angles, the Fourier transform relationship between RF pulses and magnetization pattern does not hold due to non-linearity of the Bloch equation. Therefore, to mitigate through-plane inhomogeneity in applications that utilize large-tip pulses such as for spin echo refocusing, it is necessary to come up with methods to design large-tip multiband spokes pulses. One way to approach the large-tip design is to cast the pulse design as an optimal control problem [90]. By replacing the Bloch equation with a linear model, the large-tip multiband spokes problem can be cast as an optimization problem. For a target magnetization, the optimization problem can be solved using fast algorithms such as the conjugate gradient method.

Once a method to design large-tip multiband spokes pulses is formulated, a second challenge will be to control their peak RF power. With large-tip multiband spokes pulses of practical durations, the peak RF power requirement will quickly reach the feasible limits at low multiband factors of $2 - 3$. The presented method to reduce the peak power of small-tip multiband spokes pulses is applicable at large flip angles, but it may not be sufficient to produce large-tip pulses with practical RF powers and pulse durations. The peak power can be further reduced by integrating the root-flip strategy, presented in Chapter IV, with the multiband spokes design. It will be straightforward to combine root-flipping with the simpler 'slice-joint' design but root-flipping the more advanced and better performing 'slice-independent' pulses is non-trivial. In the 'slice-joint' design case, the initial conventional multiband pulse can be replaced with a root-flipped version of the same pulse by following the steps laid out in the Theory section of Chapter IV. However, it is not possible to directly apply the proposed root-flip design to the 'slice-independent' pulses. In the 'slice-independent' design, each slice-select pulse is independently optimized to produce a desired magnetization in that slice, but the proposed root-flipped multiband pulse design begins by computing an optimized multiband profile and then finds an optimal root-flip pattern for the final multiband pulse. Therefore, if applied directly, the root-flip method cannot produce the optimal root-flip pattern for each indepedent slice optimized in the

94

'slice-independent' multiband spokes pulse design. On approach would be to design the SLR filter of each slice separately and jointly find optimal root-flip pattern for all the pulses such that the combined pulse has minimum peak power. These pulses can then be fed into the 'slice-independent' multiband spokes pulse design algorithm.

In our experiments we demonstrated that using the spokes pules, slice-accelerated images can be acquired with a reduced center-brightening artifact. The images were acquired using the conventional simultaneous multislice acquisition method where all the excited slices alias directly on top of each other. However, advanced SMS imaging methods such as CAIPIRINHA [91] can boost the SNR of the slice-accelerated images by shifting the slices with respect to each other in the transverse plane. With the slice-shifts, the reconstructed images have a smaller coil g-factor penalty and thus higher SNR. CAIPIRINHA can be integrated into the multiband spokes pulse design by modulating the phase of each slice-selective RF pulse during each TR, to get a desired slice-shift in the phase encode direction. This will require online design of 'slice-independent' mutliband spokes pulses and integration of the pulse design code with the scanner's pulse sequence code. After the shim weights and k-space trajectory are optimized, each slice-select spokes pulse can be modulated during each TR before summing the slice-select pulses to get the final CAIPIRINHA spokes pulses. The CAIPIRINHA spokes pulses will produce slice-accelerated images with higher SNR while allowing transmit field inhomogeneity mitigation.

V.2 Through-Plane Signal Loss Compensation

We presented a pulse sequence that combines spectral-spatial pulses and z-shimming to mitigate through-plane signal loss in regions of signal loss in the brain. Since the spectral-spatial pulses excited spatially disjoint regions, the different off-resonance frequency bands were treated as slices in a multislice sequence. This allowed the correction of signal loss in multiple regions without significant increase in scan duration. In vivo structural imaging experiments showed that in multiple subjects and in multiple brain slices, the proposed

multispectral z-shim method recovered signal in regions of loss while maintaning signal elsewhere. Conventional z-shim lost signal in regions that did not have a susceptibility difference. FMRI results showed that the multispectral z-shim method recovered activation in regions of signal loss while maintaining activation in rest of the slice. The proposed multispectral z-shim method is easy to implement as it is based on existing MRI techniques. We hope that it will be incorporated in routine fMRI experiments of the brain regions near air-tissue interfaces in the frontal and temporal lobes.

My future work on the MS z-shim method will include extending it to simultaneous multislice imaging to allow rapid T_2^*-weighted brain imaging with signal loss compensation. One way to do this is to follow a z-shim compensatory gradient moment driven design. The off-resonance frequency spectrum across all the simultaneously excited slices can be divided into discrete bands and z-shim moments can be calculated for each band. The spectral-spatial pulses that correspond to the off-resonance in each z-shimmed region can be summed to excite and rewind the spins in multiple slices simultaneously. In the proposed pulse design method the most time-consuming step is the manual determination of the brain masks for the different off-resonance frequency bands. This can become a bigger challenge when masks are to be defined for a large number of slices in simultaneous multislice imaging. To reduce the pulse design time, band masks can be formed by computing optimal image thresholds. The overall goal of this work will be to enable rapid whole-brain fMRI with signal loss compensation in regions with susceptibility difference.

V.3 Low Peak Power Multiband Pulses

We have presented a method to design multiband refocusing and matched excitation pulses. Simulations and experiments showed that for a given peak RF amplitude, the proposed pulses are of shorter duration compared to the phase-optimized and time-shifted multiband pulses proposed earlier. In phantom experiments, it was demonstrated that the proposed shorter duration pulses produced higher spin echo signal than the time-shifted pulses. We

foresee that the root-flipped multiband pulses will find applications in rapid imaging using spin-echo based sequences such as those usd in diffusion-weighted imaging.

In future, my investigations into low peak power multiband pulses will involve looking at solutions beyond the root-flip design. One of the ideas that I wish to pursue is the use of polynomial gradients to excite multiple slices simultaneously. An *N*-degree polynomial gradient will have *N* zero-crossings, hence in theory, it is possible to play an iso-center RF pulse along with a non-linear gradient waveform to simultaneously excite multiple slices. This method will have the same benefit as PINS where multiple slices can be excited without a peak RF power penalty. However, compared to PINS it will have the advantage of exciting a finite number of slices which can be separated in reconstruction. We note that the use of non-linear imaging gradients is a new field, some investigation has been done in the use of non-linear gradients in spatial encoding [92] and applications such as reduced field-of-view imaging [93] have been proposed earlier. Most of the scanners have non-linear shim gradients but they are usually unavailable for imaging. Therefore, this project will require the development of new or modifications to existing hardware components. In general, my research in the field of multiband imaging will involve development of methods that combined software and hardware novelties.

REFERENCES

[1] K Setsompop, B A Gagoski, J R Polimeni, T Witzel, V J Wedeen, and L L Wald. Blipped-controlled aliasing in parallel imaging for simultaneous multislice echo planar imaging with reduced g-factor penalty. *Magn Reson Med*, 67(5):1210–1224, 2012.

[2] S A Huettel, A W Song, and G McCarthy. *Functional magnetic resonance imaging*. Sinaeur Associates, Inc, second edition, December, 2008 2009.

[3] D J Larkman, J V Hajnal, A H Herlihy, G A Coutts, I R Young, and G Ehnholm. Use of multicoil arrays for separation of signal from multiple slices simultaneously excited. *J Magn Reson Imag*, 13:313–317, 2001.

[4] D A Feinberg, S Moeller, S M Smith, E J Auerbach, S Ramanna, M F Glasser, K L Miller, K Ugurbil, and E Yacoub. Multiplexed echo planar imaging for sub-second whole brain FMRI and fast diffusion imaging. *PloS One*, 5:e15710, 2010.

[5] Klaas P Pruessmann, Markus Weiger, Markus B Scheidegger, Peter Boesiger, et al. Sense: sensitivity encoding for fast mri. *Magnetic Resonance in Medicine*, 42(5):952–962, 1999.

[6] Griswold MA, Jakob PM, Heidemann RM, Nittka M, Jellus V, Wang J, Kiefer B, and Haase A. Generalized autocalibrating partially parallel acquisitions (GRAPPA). *Magn Reson Med*, 47(6):1202–1210, 2002.

[7] J M Pauly, D G Nishimura, and A Macovski. A k-space analysis of small-tip-angle excitation. *J Magn Reson*, 81:43–56, 1989.

[8] W A Grissom, M M Khalighi, L I Sacolick, B K Rutt, and M W Vogel. Small-tip-angle spokes pulse design using interleaved greedy and local optimization methods. *Magn Reson Med*, 68(5):1553–1562, 2012.

[9] C Y Yip, J A Fessler, and D C Noll. Iterative RF pulse design for multidimensional, small-tip-angle selective excitation. *Magn Reson Med*, 54:908–917, 2005.

[10] U Katscher, P Bornert, C Leussler, and Brink J S vd. Transmit SENSE. *Magn Reson Med*, 49:144–150, 2003.

[11] Y Zhu. Parallel excitation with an array of transmit coils. *Magn Reson Med*, 51:775–784, 2004.

[12] W A Grissom, C Y Yip, Z Zhang, V A Stenger, J A Fessler, and D C Noll. Spatial domain method for the design of RF pulses in multicoil parallel excitation. *Magn Reson Med*, 56:620–629, 2006.

[13] M Shinnar, S Eleff, H Subramanian, and JS Leigh. The synthesis of pulse sequences yielding arbitrary magnetization vectors. *Magn Reson Med*, 12:74–80, 1989.

[14] P Le Roux. Exact synthesis of radio frequency pulses. *In Proceedings of the 7th SMRM*, page 1049, 1988.

[15] J M Pauly, P Le Roux, D G Nishimura, and A Macovski. Parameter relations for the Shinnar-Le Roux selective excitation pulse design algorithm. *IEEE Trans Med Imag*, 10:53–65, 1991.

[16] F Schick. Whole-body MRI at high field: technical limits and clinical potential. *Eur Radiol*, 15:946–959, 2005.

[17] D I Hoult. Sensitivity and power deposition in a high-field imaging experiment. *J Magn Reson Imaging*, 12:46–67, 2000.

[18] Q X Yang, W Mao, J Wang, M B Smith, H Lei, X Zhang, K Ugurbil, and W Chen. Manipulation of image intensity distribution at 7.0T: passive RF shimming and focusing with dielectric pads. *J Magn Reson Imaging*, 24:197–202, 2006.

[19] S Saekho, C Y Yip, D C Noll, F E Boada, and V A Stenger. Fast-k_z three-dimensional tailored radiofrequency pulse for reduced B_1 inhomogeneity. *Magn Reson Med*, 55:719–724, 2006.

[20] X Wu, S Schmitter, E J Auerbach, S Moeller, K Uğurbil, and P F Van de Moortele. Simultaneous multislice multiband parallel radiofrequency excitation with independent slice-specific transmit B_1 homogenization. *Magn Reson Med*, 70(3):630–638, 2013.

[21] I R Young, I J Cox, D J Bryant, and G M Bydder. The benefits of increasing spatial resolution as a means of reducing artifacts due to field inhomogeneities. *Magnetic Resonance Imaging*, 6:585–590, 1988.

[22] J L Wilson and P Jezzard. Utilization of an intra-oral diamagnetic passive shim in functional MRI of the inferior frontal cortex. *Magn Reson Med*, 50:1089–1094, 2003.

[23] R T Constable. Functional MR imaging using gradient-echo echo-planar imaging in the presence of large static field inhomogeneities. *J Magn Reson Imaging*, 5:746–752, 1995.

[24] A W Song. Single-shot EPI with signal recovery from the susceptibility-induced losses. *Magn Reson Med*, 46:407–411, 2001.

[25] H G Guo and A W Song. Single-shot spiral image acquisition with embedded z-shimming for susceptibility signal recovery. *J Magn Reson Imaging*, 18:389–395, 2003.

[26] K A Heberlein and X Hu. Simultaneous acquisition of gradient-echo and asymmetric spin-echo for single-shot z-shim: Z-SAGA. *Magn Reson Med*, 51:212–216, 2004.

[27] C Y Yip, J A Fessler, and D C Noll. Advanced three-dimensional tailored RF pulse

for signal recovery in T2*-weighted functional magnetic resonance imaging. *Magn Reson Med*, 56(5):1050–1059, 2006.

[28] C Y Yip, D Yoon, V T Olafsson, S Lee, W A Grissom, J A Fessler, and D C Noll. Spectral-spatial pulse design for through-plane phase precompensatory slice selection in T_2^*-weighted functional MRI. *Magn Reson Med*, 61:1137–1147, 2009.

[29] C Yang, W Deng, V Alagappan, L L Wald, and V A Stenger. Four-dimensional spectral-spatial RF pulses for simultaneous correction of B1+ inhomogeneity and susceptibility artifacts in T2*-weighted MRI. *Magn Reson Med*, 64:1–8, 2010.

[30] D G Norris, P J Koopmans, R Boyacioglu, and M Barth. Power independent of number of slices radio frequency pulses for low-power simultaneous multislice excitation. *Magn Reson Med*, 66:1234–1240, 2011.

[31] G Goelman. Two methods for peak RF power minimization of multiple inversion-band pulses. *Magn Reson Med*, 37:658–665, 1997.

[32] E Wong. Optimized phase schedules for minimizing peak RF power in simultaneous multi-slice RF excitation pulses. *In Proceedings of the 20th Annual Meeting of ISMRM, Melbourne, Victoria, Australia*, page 2209, 2012.

[33] E J Auerbach, J Xu, E Yacoub, S Moeller, and K Uğurbil. Multiband accelerated spin-echo echo planar imaging with reduced peak RF power using time-shift RF pulses. *Magn Reson Med*, 69:1261–67, 2013.

[34] X Wu, K Ugurbil, and P F Van de Moortele. Peak RF power constrained pulse design for multi-band parallel excitation. *In Proceedings of the 21st Annual Meeting of ISMRM, Salt Lake City, Utah, USA*, 21:4253, 2013.

[35] Z Zhang, C Y Yip, W A Grissom, D C Noll, F E Boada, and V A Stenger. Reduc-

tion of transmitter B_1 inhomogeneity with transmit SENSE slice-select pulses. *Magn Reson Med*, 57(5):842–847, 2007.

[36] D M Olsson and L S Nelson. The Nelder-Mead simplex procedure for function minimization. *Technometrics*, 17(1):45–51, 1975.

[37] K Nehrke and P Bornert. Dream - a novel approach for robust, ultrafast, multislice B1 mapping. *Magn Reson Med*, 68:1517–1526, 2012.

[38] L I Sacolick, F Wiesinger, I Hancu, and M W Vogel. B_1 mapping by Bloch-Siegert shift. *Magn Reson Med*, 63(5):1315–1322, 2010.

[39] M Jankiewicz, J C Gore, and W A Grissom. Improved encoding pulses for Bloch-Siegert B_1^+ mapping. *J Magn Reson*, 226:79–87, 2013.

[40] E Schneider and G Glover. Rapid in vivo proton shimming. *Magn Reson Med*, 18(2):335–347, Apr 1991.

[41] N Otsu. A threshold selection method from gray-level histograms. *Automatica*, 11(285-296):23–27, 1975.

[42] V L Yarnykh. Actual flip-angle imaging in the pulsed steady state: A method for rapid three-dimensional mapping of the transmitted radiofrequency field. *Magn Reson Med*, 57(1):192–200, 2007.

[43] X Wu, D K Deelchand, V L Yarnykh, K Uğurbil, and P-F Van de Moortele. Actual flip angle imaging: From 3D to 2D. In *Proceedings 17th Scientific Meeting, International Society for Magnetic Resonance in Medicine, Honolulu*, page 372, 2009.

[44] J T Schneider, M Haas, W Ruhm, J Hennig, and P Ullmann. Robust spatially selective excitation using radiofrequency pulses adapted to the effective spatially encoding magnetic fields. *Magn Reson Med*, 65:409–421, 2011.

[45] K Harkins, M D Does, and W A Grissom. Iterative method for predistortion of MRI gradient waveforms. *IEEE Trans Med Imag*, 33(8):1641–7, 2014.

[46] X Wu, G Adriany, K Ugurbil, and P F Van de Moortele. Correcting for strong eddy current induced B0 modulation enables two-spoke RF pulse design with parallel transmission: demonstration at 9.4T in the human brain. *PloS One*, 8(10):e78078, 2013.

[47] E J Auerbach, J Xu, E Yacoub, S Moeller, and K Ugurbil. Multiband accelerated spin-echo echo planar imaging with reduced peak RF power using time-shifted RF pulses. *Magn Reson Med*, 69:1261–1267, 2013.

[48] B Guérin, K Setsompop, Ye Huihui, B A Poser, V A Stenger, and L L Wald. Design of parallel transmission pulses for simultaneous multislice with explicit control for peak power and local specific absorption rate. *Magn Reson Med*, doi: 10.1002/mrm.25325, 2014.

[49] A Jesmanowicz, B B Biswal, and J S Hyde. Reductio in FRE-EPI intravoxel dephasing using thin slices and short te. *In Proceedings of the 7th Annual Meeting of ISMRM, Philadelphia, Pennsylvania, USA.*, page 1619, 2012.

[50] T Q Duong, E Yacoub, G Adriany, X Hu, K Ugurbil, and S G Kim. Microvascular BOLD contribution at 4 and 7 T in the human brain: gradient-echo and spin-echo fMRI with suppression of blood effects. *Magn Reson Med*, 49(6):1019–1027, 2003.

[51] M J Donahue, H Hoogduin, P C van Zijl, P Jezzard, P R Luijten, and J Hendrikse. Blood oxygenation level-dependent (BOLD) total and extravascular signal changes and $\triangle$R2* in human visual cortex at 1.5, 3.0 and 7.0 T. *NMR in Biomedicine*, 24(1):25–34, 2011.

[52] Z H cho and Y M Ro. Reduction of susceptibility artifact in gradient-echo imaging. *Magn Reson Med*, 23:193–200, 1992.

[53] R Schneider, F Boada, J Haueisen, and J Pfeuffer. Automated slice-specific simultaneous z-shim method for reducing B1 inhomogeneity and susceptibility-induced signal loss with parallel transmission at 3T. *Magn Reson Med*, 65, 2014.

[54] C H Meyer, J M Pauly, A Macovski, and D G Nishimura. Simultaneous spatial and spectral selective excitation. *Magn Reson Med*, 15:287–304, 1990.

[55] E Schneider and G Glover. Rapid in vivo proton shimming. *Magn Reson Med*, 18(2):335–347, Apr 1991.

[56] W A Grissom, A B Kerr, A B Holbrook, J M Pauly, and K B Pauly. Maximum linear-phase spectral-spatial radiofrequency pulses for fat-suppressed proton resonance frequency-shift MR thermometry. *Magn Reson Med*, 62:1242–1250, 2009.

[57] G M Bydder and I R Young. MRI: Clinical use of the inversion recovery sequence. *J. Comp. Asst. Tomogr.*, 9:659–675, 1985.

[58] M Jenkinson, C F Beckmann, T E Behrens, M W Woolrich, and Smith S M. FSL. *NeuroImg*, 62:782–790, 2012.

[59] M W Woolrich, S Jbabdi, B Patenaude, M Chapple, S Makhni, T E Behrens, C F Beckmann, M Jenkinson, and Smith S M. Bayesian analysis of neuroimaging data is FSL. *NeuroImg*, 45:173–186, 2009.

[60] S M Smith, M Jenkinson, M W Woolrich, C F Beckmann, T E Behrens, H Johansen-Berg, P R Bannister, M De Luca, I Drobnjak, D E Flitney, R Niazy, J Saunders, J Vickers, Y Zhang, N De Stefano, J M Brady, and P M Matthew. Advances in functional and structural MR image analysis and implementation as FSL. *NeuroImg*, 23:208–219, 2004.

[61] M W Woolrich, B Ripley, J M Brady, and S M Smith. Temporal autocorrelation in univariate linear modelling of FMRI data. *NeuroImg*, 14(6):1370–1386, 2001.

[62] S Lai and G Glover. Three-dimensional spiral fMRI technique: a comparison with 2D spiral acquisition. *Magn Reson Med*, 39:68–78, 1998.

[63] G Glover. Spiral imaging in fMRI. *NeuroImg*, 62:706–712, 2012.

[64] R J Anderson, B A Poser, and V A Stenger. Simultaneous multislice spectral-spatial excitations for reduced signal loss susceptibility artifact in BOLD functional MRI. *Magn Reson Med*, 2013.

[65] A Sharma, M Donahue, V A Stenger, and W A Grissom. SALSAS: Spectral spatial excitation with z-shimming to mitigate through-plane signal loss in single-slice and multiband gradient echo imaging. *Joint Annual Meeting ISMRM and ESMRMB, Milan, Italy*, page 1479, 2014.

[66] E C Wong. Optimized phase schedules for minimizing peak RF power in simultaneous multi-slice RF excitation pulses. In *Proceedings 20th Scientific Meeting, International Society for Magnetic Resonance in Medicine, Melbourne*, page 2209, 2012.

[67] C Eichner, Wald L L, and K Setsompop. A low power radiofrequency pulse for simultaneous multislice excitation and refocusing. *Magn Reson Med*, 72:949–952, 2014.

[68] M Shinnar. Reduced power selective excitation radio frequency pulses. *Magn Reson Med*, 32(5):658–660, Nov 1994.

[69] S Pickup and X Ding. Pulses with fixed magnitude and variable phase response profiles. *Magn Reson Med*, 33:648–655, 1995.

[70] S Pickup and M Popescu. Efficient design of pulses with trapezoidal magnitude and linear phase response profiles. *Magn Reson Med*, 38:137–145, 1997.

[71] M Lustig, C H Cunningham, and J M Pauly. *A Monte-Carlo algorithm for designing ultra-high time-bandwidth, minimum peak $|B_1|$, selective saturation and inversion RF pulses*. In Proceedings of the ENC, 2006, 2006.

[72] R F Schulte, P Le Roux, M W Vogel, and H Koenig. Design of phase-modulated broadband refocusing pulses. *J Magn Reson*, 190:271–79, 2008.

[73] T G Reese, O Heid, R M Weisskoff, and V J Wedeen. Reduction of eddy-current-induced distortion in diffusion MRI using a twice-refocused spin echo. *Magn Reson Med*, 49:177–182, 2003.

[74] W A Grissom, G C McKinnon, and M W Vogel. Nonuniform and multidimensional Shinnar-Le Roux RF pulse design method. *Magn Reson Med*, 68:690–702, 2012.

[75] J G Proakis and D G Manolakis. *Digital signal processing: Principles, algorithms and applications*. Prentice-Hall; 1996. 1016 p, 1996.

[76] Z Zun, B A Hargreaves, J M Pauly, and G Zaharchuk. Near-contiguous spin echo imaging using matched-phase RF and its application in velocity-selective arterial spin labeling. *Magn Reson Med*, 71:2043–50, 2014.

[77] P Balchandani, M Yamada, J M Pauly, P Yang, and D M Spielman. Self-refocusing spatial-spectral pulse for positive contrast imaging of cells labeled with SPIO nanoparticles. *Magn Reson Med*, 62:183–192, 2009.

[78] P Balchandani, M M Khalighi, G Glover, J M Pauly, and D M Spielman. Self-refocused adiabatic pulse for spin echo imaging at 7T. *Magn Reson Med*, 67:1077–85, 2012.

[79] J-Y Park and M Garwood. Spin-echo MRI using $\pi/2$ and π hyperbolic secant pulses. *Magn Reson Med*, 61:175–87, 2009.

[80] M Grant and S Boyd. CVX: Matlab software for disciplined convex programming, version 2.1, March 2014. http://cvxr.com/cvx.

[81] P P Stang, A B Kerr, W A Grissom, J Pauly, and G Scott. *Vector Iterative Pre-Distortion: An Auto-calibration Method for Transmit Arrays*. In Proceedings of the 17th Annual Meeting of ISMRM, Honolulu, Hawaii, USA, 2009. p. 395, 2009.

[82] K Zhu, R F Dougherty, A M Takahashi, J M Pauly, and A B Kerr. *Nyquist ghosting correction for simultaneous multislice echo planar imaging*. In Proceedings of the 22nd Annual Meeting of ISMRM, Milan, Italy, 2014. p. 647, 2014.

[83] S Conolly, G Glover, D Nishimura, and A Macovski. A reduced power selective adiabatic spin-echo pulse sequence. *Magn Reson Med*, 18:28–38, 1991.

[84] K Zhu, A B Kerr, and J M Pauly. *Nonlinear-phase multiband $90°$-$180°$ RF pair with reduced peak power*. In Proceedings of the 22nd Annual Meeting of ISMRM, Milan, Italy, 2014. p. 1440, 2014.

[85] K J Lee, M N J Paley, and Wild J M. Combined simulated annealing and Shinnar-Le Roux pulse design of slice-multiplexed RF pulses for multi-slice imaging. *J Magn Reson*, 182:133–142, 2006.

[86] S P Boyd and L Vandenberghe. *Convex optimization*. Cambridge university press, 2004.

[87] C H Cunningham and M L Wood. Method for improved multiband excitation profiles using the Shinnar-Le Roux transform. *Magn Reson Med*, 42:577–584, 1999.

[88] P Le Roux, R J Gilles, G C McKinnon, and P G Carlier. Optimized outer volume suppression for single-shot fast spin-echo cardiac imaging. *J Magn Reson Imag*, 8:1022–1032, 1998.

[89] R F Schulte, J Tsao, P Boesiger, and K P Pruessmann. Equi-ripple design of quadratic-phase RF pulses. *J Magn Reson*, 166(1):111–122, 2004.

[90] W A Grissom, , D Xu, A B Kerr, and J A Fessler. Fast large-tip-angle multidimensional and parallel RF pulse design in MRI. *IEEE Trans Med Imaging*, 28(10):1548–1559, 2009.

[91] F A Breuer, M Blaimer, R M Heidemann, M F Mueller, W A Grissom, and P M Jakob. Controlled aliasing in parallel imaging results in higher acceleration (CAIPIRINHA) for multi-slice imaging. *Magn Reson Med*, 53:684–691, 2005.

[92] J Hennig, A M Welz, G Schultz, J Korvink, Z Liu, O Speck, and M Zaitsev. Parallel imaging in non-bijective, curvilinear magnetix field gradients: a concept study. *Magn Reson Matter Phy*, 21:5–14, 2008.

[93] E Kopanoglu, E Atalar, and R T Constable. Reduced-FOV imaging with excitation using nonlinear gradient magnetic fields (ENiGMa). *Annual Meeting ISMRM, Salt Lake City, Utah, USA*, page 12, 2013.